APPLICATIONS OF DIGITAL HOLOGRAMS FOR THE SELECTION AND DETECTON OF TRANSVERSE LASER MODES

By

Sandile Ngcobo

A thesis submitted in fulfilment of the academic requirements for the PhD degree of Science in the School of Chemistry and Physics, University of KwaZulu-Natal, Durban.

Supervisor:
Prof. Andrew Forbes

May 2014

Abstract

The transverse mode of generally available commercial lasers in most instances is not suitable for desired applications. Shaping the laser beam either extra-cavity, that is outside the laser resonator, or intra-cavity, which is inside the laser resonator, is required to force the laser beam or cavity to oscillate on a selected desirable single laser mode. The shaped laser beam's spatial intensity profile and propagation properties would then be suitable for the desired application. The crux of the work presented in this thesis involves intra-cavity beam shaping where we generate desirable transverse modes from inside the laser resonator and detecting such mode using digital holograms.

In Chapter 1 we discuss a novel technique of modal decomposition of an arbitrary optical light field into underlying superposition of modes. We show that it can be used to extract physical properties associated with the initial light field such as the intensity, the phase and M^2, etc. We show that this novel modal decomposition approach that requires no *a priori* knowledge of the spatial scale of the modes which lead to an optimised modal expansion. We tested the new technique by decomposing arbitrary modes of a diode-pumped solid-state laser to demonstrate its versatility.

In Chapter 2 we experimentally demonstrate selective generation of Laguerre-Gaussian (LG) modes of variable radial order from 0 to 5, with zero azimuthal order. To generate these customised LG modes from within the laser resonator we show that a specialised optical element in a form of an amplitude mask is required to be inserted inside the laser resonator. The amplitude mask is designed and fabricated to contain absorbing rings which are immutably connected to the desired LG mode. The geometry of the absorbing ring radii are selected to match and coincide with the location of the selected LG mode zero intensity parts inside the cavity. We show for the first time that the generated LG modes using this method are of high mode purity and a gain mode volume similar to the desired LG mode. The results provide a possible alternative route to high brightness diode pumped solid state laser sources.

In Chapter 3 we show that we can overcome the disadvantage of the specialised optical element being immutably connected to the selection of a particular mode by experimentally demonstrating a novel digital laser capable of generating arbitrary laser modes inside the laser resonator. The digital laser is realised by intra-cavity replacing an end-mirror of the resonator with a rewritable holographic mirror which is an electrically addressed reflective phase-only

spatial light modulator (SLM). We show that by calculating a new computer-generated holographic gray-scale image on the SLM representing the desired customized laser mode digitally, the digital laser resonator is capable of generating the desired laser modes on demand. The results provide a new laser that can generate customized laser modes.

In Chapter 4 we show that the digital laser can be used as a test bed for conceptualizing, testing, and proving ideas. We experimentally demonstrate this by using a simple laser cavity that contains an opaque ring which is digitally programmed on the SLM and an adjustable circular aperture on the output coupler mirror. We show that by manually varying the diameter of the aperture without realignment of the laser, the generated laser modes can be tuned from a Gaussian mode to a Flat-top mode. This opens up new digital methods that can be used to test laser beam shaping techniques.

In Chapter 5 we outline a simple laser cavity comprising an opaque ring and a circular aperture that is capable of producing spatially tuneable laser modes, from a Gaussian beam to a Flat-top beam. The tuneability is achieved by varying the diameter of the aperture and thus requires no realignment of the cavity. We demonstrate this principle using a digital laser with an intra-cavity spatial light modulator, and confirm the predicted properties of the resonator experimentally.

In Chapter 6 we discuss the techniques used to intra-cavity generate and detect LG beams with a non-zero azimuthal index since they are known to carry orbital angular momentum (OAM), and have been routinely created external to laser cavities. We show that the few reports of obtaining such beams from laser cavities suffer from inconclusive evidence of the real electromagnetic field. In this Chapter we revisit this question and show that an observed doughnut beam from a laser cavity may not be a pure Laguerre–Gaussian azimuthal mode but can be an incoherent sum of petal modes, which do not carry OAM. We point out the requirements for future analysis of such fields from laser resonators.

In Chapter 7 we conclude and discuss future work.

Declaration 1

The experimental work described in this thesis was carried out at the Council for Scientific and Industrial Research, National Laser Centre, while the candidate was registered with the School of Physics, University of KwaZulu-Natal, Durban, Westville, from August 2012 to January 2014, under the supervision of Professor Andrew Forbes.

These studies represent original work by the author and have not otherwise been submitted in any form for any degree or diploma to any tertiary institution. Where use has been made of the work of others it is duly acknowledged in the text.

Signed: _____

On this_____day of_____2014

As the candidate's supervisor I have approved this dissertation for submission.

_____

Prof Andrew Forbes

On this_____day of_____2014

Declaration 2 - Plagiarism

I, ……. declare that

1. The research reported in this thesis, except where otherwise indicated, is my original research.

2. This thesis has not been submitted for any degree or examination at any other university.

3. This thesis does not contain other persons' data, pictures, graphs or other information, unless specifically acknowledged as being sourced from other persons.

4. This thesis does not contain other persons' writing, unless specifically acknowledged as being sourced from other researchers. Where other written sources have been quoted, then:
   a. Their words have been re-written but the general information attributed to them has been referenced
   b. Where their exact words have been used, then their writing has been placed in italics and inside quotation marks, and referenced.

5. This thesis does not contain text, graphics or tables copied and pasted from the Internet, unless specifically acknowledged, and the source being detailed in the thesis and in the References sections.

Signed: ……

Declaration 3 – Publications

Peer-Reviewed Journal Papers:

[1]. C. Schulze, **S Ngcobo**, M. Duparré, A Forbes, "Modal decomposition without a priori scale information," Opt. Express **20** (25), 27866 (2012).

[2]. **S. Ngcobo**, K. Aït-Ameur, N. Passilly, A. Hasnaoui, A. Forbes, "Exciting higher-order radial Laguerre-Gaussian modes in a diode-pumped solid-state laser resonator," Applied Optics **52** (10), 2093 (2013).

[3]. **S. Ngcobo**, I. Litvin, L. Burger, A. Forbes, "A digital laser for on-demand laser modes," Nature Commun. **4**, 2289 (2013).

[4]. S. **Ngcobo**, K. Ait-Ameur, I. Litvin, A. Hasnaoui, A. Forbes, "Tuneable Gaussian to flat-top resonator by amplitude beam shaping," Opt. Express **21** (18), 21113 (2013).

[5] I.A. Litvin, **S. Ngcobo**, D. Naidoo, K. Ait-Ameur, and A. Forbes, "Doughnut laser beam as an incoherent superposition of two petal beams," Applied Lett. **39** (3), 704 (2014).

International Conference Proceedings Papers:

[1]. T. Godin, **S. Ngcobo**, E. Cagniot, M. Fromager, A. Forbes, K. Aït-Ameur, "Strong reducing of the laser focal volume," Proc. of SPIE **8130**, 81300Q (2011).

[2]. A. Forbes, C. Schulze, **S. Ngcobo**, D. Flamm, D. Naidoo, A. Dudley, M. Duparre, "Unravelling light with digital holograms," Proc. of SPIE **8600**, 86000U (2013).

[3]. A. Forbes, **S. Ngcobo**, T. Godin, K. Ait-Ameur, "Selective excitation of higher-order modes in diode-pumped solid-state laser resonators," Proc. of SPIE **8600**, 86000Y (2013).

[4]. **S. Ngcobo**, I. Litvin, L. Burger and A. Forbes, "Real-time dynamic control of laser modes," The 9th International Workshop on Adaptive Optics for Industry and Medicine, Stellenbosch, Cape Town, South Africa (2013).

[5]. **S. Ngcobo**, A. Forbes, A. Hasnaoui, A. Harfouche, A. Bencheikh, M. Traïche, D. Louhibi, M. Fromager, E. Cagniot, K. Aït-Ameur, "Advantages of forcing the laser oscillation on a high order transverse mode but single," The 3rd International Conference on Photonics an Applications (ICOPA), Algeria (2013).

[6]. L. Burger , I. Litvin, **S. Ngcobo** and A. Forbes, "Producing Kaleidoscope Modes using the Digital Laser," The 9th International Workshop on Adaptive Optics for Industry and Medicine, Stellenbosch, Cape Town, South Africa (2013).

[7]. **S. Ngcobo**, I.A. Litvin, L. Burger and A. Forbes, "Digital control of laser mods with an intra-cavity spatial light modulator," Proc. of SPIE **8960**, 8960-68 (2014).

[8] A. Forbes, **S. Ngcobo**, L. Burger and I.A. Litvin, "The digital laser: on-demand laser modes with the click of a button," Proc. of SPIE **8960**, 8960-55 (2014).

[9] **S. Ngcobo**, I.A. Litvin, K. Ait-Ameur, A. Forbes, "Tuneable Gaussian to flat-top resonator by amplitude beam shaping using a digital laser," Proc. of SPIE **8960**, 8960-56 (2014).

[10]. L. Burger, I. Litvin, **S. Ngcobo** and A. Forbes, "How to make a Digital Laser," SPIE - 3rd SMEOS, Skukuza, Kruger National Park, South Africa (2014).

National Conference Proceedings:

[1]. **S. Ngcobo**, A. Forbes, K Ait-Ameur, "Superresollution Beams," 56th South African Institute of Physics conference, University of South Africa (2011).

[2]. **S. Ngcobo**, K Ait-Ameur, A. Forbes, "Superresollution Beams," African Laser Center, Stellenbosch, Cape Town (2011).

[3]. **S. Ngcobo**, K Ait-Ameur, A. Forbes, "Intra-cavity Generation of High Order LG_{pl} Modes," 57th South African Institute of Physics conference, University of Pretoria (2012).

[4]. **S. Ngcobo**, A. Forbes, K Ait-Ameur, "High efficient LG_{p0} End Pumped Nd:YAG Lasers," 57th South African Institute of Physics conference, University of Pretoria (2012).

[4]. **S. Ngcobo**, K Ait-Ameur, A. Forbes, "Intra-cavity Generation of High Order LG_{pl} Modes," IONS1 African conference, Drakensburg Cathedral Peak (2012).

[5]. **S. Ngcobo**, I. Litvin, K. Ait-Ameur and A. Forbes, "Tuneable Gaussian to Flat-Top resonator by amplitude beam shaping," 58th South African Institute of Physics conference, University of Zululand (2013).

[6]. D. Naidoo, **S. Ngcobo**, T. Godin, M. Fromager, K. Ait-Ameur, A. Forbes, "Azimuthal beam superpositions with intra-cavity rings," 58th South African Institute of Physics conference, University of Zululand (2013).

[7]. **S. Ngcobo**, I. Litvin, L. Burger and A. Forbes, "The digital laser," 58th South African Institute of Physics conference, University of Zululand (2013).

[8]. **S. Ngcobo**, I. Litvin, L. Burger and A. Forbes, "Real-Time dynamic control of laser beams," Emerging Researchers Symposium, CSIR (2013).

[9]. **S. Ngcobo**, I. Litvin, L. Burger and A. Forbes, "Digital laser," Emerging Researchers Symposium, CSIR (2013).

International Patents Filed:

[1]. *Title*: Modal decomposition of a laser beam
Description: The invention relates to a method of performing a modal decomposition of a laser beam and apparatus for performing the method.
Inventors: **Sandile Ngcobo**, Christian Schulze, Michael Duparre and Andrew Forbes.

[2]. *Title*: Method of operating a laser and laser apparatus using intra-cavity beam shaping.

Description: The invention relates to a method of operating a laser and to laser apparatus making use of intra-cavity beam shaping.
Inventors: **Sandile Ngcobo**, Igor Litvin, Liesl Bergur and Andrew Forbes.

Signed: ……

Table of Contents

List of Figures

List of Tables

List of Symbols

E	Electrical field
γ	Loss factor
ω	Frequency
t	Time
B	Brightness
P	Power in the mode
λ	Wavelength
M^2	Beam quality factor
∇_t	Transverse Laplace operator
u	Optical electric field
k	Wave vector number
z	Propagation axis
r	Radial coordinate
Φ	Azimuthal angle
$P(z)$	Longitudinal phase of the wave
$q(z)$	Radial amplitude
z_R	Rayleigh range
$R(z)$	Radius of curvature
i	Imaginary
w_0	Minimum beam waist
$w(z)$	Beam waist
E_0	Electrical field amplitude
Φ	Gouy phase shift
I	Intensity
m	Azimuthal mode index
n	Azimuthal mode index
$H_{m,n}$	Hermite polynomial
p	Radial mode index
l	Azimuthal mode index
$w_{p,l}$	Laguerre Gaussian beam waist
ψ_n	Number of modes
ρ_n^2	Modal weights
c_n	Expansion coefficient
$\Delta\phi_n$	Phase difference
$L_p^{\lvert l \rvert}$	Laguerre polynomial
$c_{pl}^{a,b}$	Complex expansion coefficient
$LG_{p,l}$	Laguerre-Gaussian
L_{FM}	Fundamental mode losses
V_p	Radial mode volume
l_0	Length of gain medium
δ	Round trip losses
L	Cavity length
ρ_a	Ring radius
ρ_c	Aperture radius
Y_a	Normalized ring radius
Y_c	Normalized aperture radius
D	Doughnut

Acknowledgements

I would like to express my sincere gratitude and also appreciation to every person who supported me and assisted me throughout the time spent working on my PhD. I would like to make a special mention of:

The CSIR National Laser Centre - for employing me as a full-time researcher early in my research career and for giving me the opportunity and time to conduct this research.

Professor Andrew Forbes - for being my supervisor and also for giving me an opportunity to work on these experiments. There has been lot of good mentoring over the years that you have instilled in me and also a lot of exposure to other fields of research and research groups and that I would really like to say thank you, again it is very much appreciated.

Professor Kamel Ait-Ameur of the University of Caen, France – I would like to thank you for all your hard work with assisting me and the progress of the work in making the DOE masks. Thank you also for hosting me at your university and for the theoretical guidance of work you provided while you were hosting me.

To my fellow colleagues - Dr. Igor Litvin and Liesl Burger, I would thank you for all your hard work, assistance and input, in this work. To Darryl Naidoo and Dr. Angela Dudley, thank you for assisting me with computer programs and also in the laboratory and just for making the journey through my PhD less difficult.

To my family – I’m very grateful for the endurance, support and encouragement that you provided me with to further my studies especially my wife, Thabile. To my kids Osiphayo and Lubanzi, this work is dedicated to you two.

CHAPTER ONE

Mode Selection in Diode-Pumped Solid-State Laser Resonators

1.1. Overview

The discovery of Maxwell's equations in 1861 by the Scottish physicist James Clerk Maxwell, predicted the existence of electromagnetic waves with infinite range of wavelengths. Maxwell's equations which are a set of partial differential equations have been shown to form the foundation of classical physics that describe how electromagnetic fields are generated and propagated.

Maxwell's equations which describe the electromagnetic field in space and time can be used to derive the time-independent Helmholtz equation by the method of separation of variables to reduce the complexity of the analysis [1.1]. The solution of the Helmholtz equation within the paraxial approximation has been shown to produce periodic solutions when appropriate boundary conditions are used. The periodic solutions have found to be modes or self-reproducing electromagnetic field patterns of a resonator.

The selection of a particular set of modes inside the resonator has been shown to depend on the boundary condition being cylindrical or Cartesian coordinate. In the early 1960's, many experiments were performed involving solid-state, gas and semiconductor lasers to force a resonator to select different types of higher-order modes by using rectangular and circular mirrors to generate modes such as Hermite-Gaussian (HG) and Laguerre-Gaussian (LG) modes [1.2-1.6]. The other more general method of selecting a particular high-order mode has been the use of introducing optical elements inside the laser resonator, such as apertures, gradient lenses, phase masks and amplitude masks. There is also a method of replacing the resonator mirrors with gradient mirrors, deformable mirrors [1.7] and more recently with spatial light modulators (SLM) that will be discussed in Chapter 4. All these optical elements have the common effect of causing high losses on undesired laser modes making them not to oscillate in the resonator, while at the same time causing low losses on the desired mode.

Over the year's many experiments involving the generation of high-order Laguerre-Gaussian modes have been reported [1.8-1.20] but have not been used to produce high brightness beams, B:

$$B = \frac{\pi^2 P}{\lambda^2 M^4}; \tag{1.1.1}$$

where P is the power in the mode and M^2 the beam propagation factor of the mode. Most of the interest over the years has been dedicated on generating single fundamental Gaussian low-order modes using many schemes such as matching the pump size to the Gaussian beam size in order to maximize modal overlap, to either aperturing the cavity to allow only the Gaussian beam to oscillate as the fundamental mode, all in order to force the laser to produce high brightness beams which have been a driving force in many applications [1.21-1.22]. The brightness parameter has been shown to be directly proportional to the power in the mode and also at the same time inversely proportional to the beam propagation factor (M^2) squared. Therefore the brightness of the laser will generally be low if selecting a very high-order mode to oscillate in the resonator. This explains why most of the attention over the years has been placed on developing high brightness lasers that produced the lowest-order fundamental Gaussian mode. This is because the lowest-order Gaussian mode has the lowest propagation factor which in turn produces the highest brightness parameter. This trend has been influenced by many applications which required laser beams that have a high brightness parameter. The method of generating a singular high-order mode to extract maximum power from the laser and how the brightness of the laser is increased from such a high-order mode is discussed in details in Chapter 3.

More recently, there has been an increase in the number of publications and applications that require customised higher-order modes to be selected and produced by diode pumped solid-state lasers [1.23]. The interest in using diode-pumped solid state lasers which first were realized as flash lamp pumped solid state lasers, comes from the advantage that diode pumped systems have become very efficient when compared to lamp pumped systems[1.24-1.26]. Other advantages such as better frequency stability, high repetition rate, reliability and compactness have made diode pumped solid state lasers to be laser system of choice for many applications. These applications involve high power solid state lasers for industrial manufacturing application such as welding, cutting and drillings of metal sheets, to applications such as remote sensing and laser weapons [1.27]. There are also applications which prefer low power solid state laser systems such as micromachining, optical communication and laser surgery [1.28].

The revived increase on developing laser resonators that produce higher-order modes such as Laguerre-Gaussian beams is due to the recent discovery that they possess well defined orbital angular momentum along the optical axis for non-zero values of azimuthal order *l*, that have a helical wave front [1.29]. Application such as optical tweezers have been realized with high-order Laguerre-Gaussian beams that transfer orbital angular momentum to trapping particles and induce them to rotate around the optical axis. There are many applications [1.30-1.38] that require high-order LG beams such as material's processing, quantum communication, particle traps and high resolution microscopes. All these applications require the laser to oscillate on a high-order LG beam using holograms, spatial light modulator, diffractive optics and many other schemes.

There is an increasing interest of generating other high-order families of modes in geometries with different symmetries such as rectangular, cylindrical, circular and elliptical that could be used in many other potential applications [1.39-1.47]. These modes can be generated inside the laser resonator and also outside using different types of optical elements. One of the benefits of generating these high-order modes inside the laser cavity [1.16, 1.48-1.52] is that the beam's power and energy could be scaled up. Some of the techniques of generating different families of high-order modes inside the laser resonator are discussed in detail in Chapter 4.

1.2. Laser resonator modes and their selection

A laser resonator which is sometimes called a laser cavity is a device that has mirrors arranged in a manner that forms a light field standing wave. In between the mirrors, a gain medium is usually inserted to provide feedback of the laser light field. In the case of a solid state laser the gain medium is in a form of a solid, like an Nd:YAG crystal. The pump source which provides energy to the gain medium for the amplification to occur can be an optical pump source such as flash lamps or diode lasers as shown in Fig. 1.2.1.

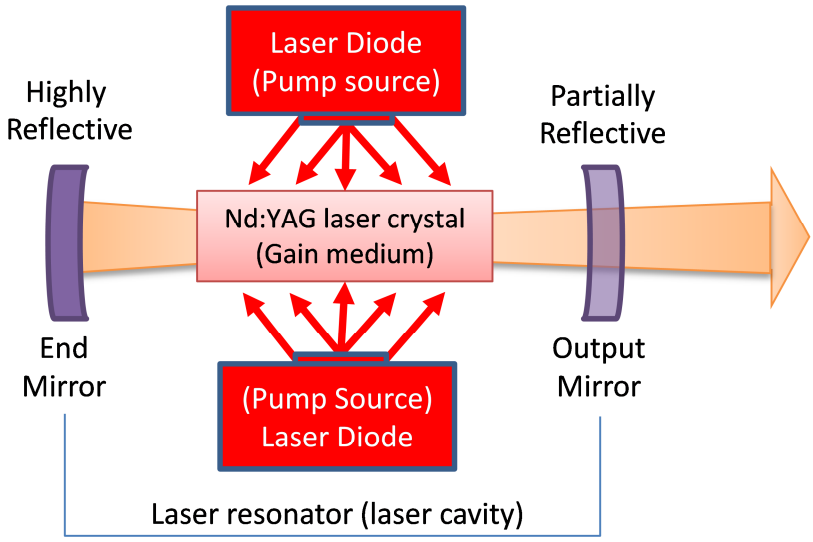

Fig. 1.2.1: Laser resonator schematic diagram showing the laser cavity mirrors, pump source and the gain medium.

The end-mirror of the laser resonator is usually designed to be highly reflective for the laser light, while the output mirror is partially reflective in order to allow some of the laser light to exit the laser resonator for usage. For the laser light to exit the resonator, firstly, the crystal (or active medium) which generates the laser light should be pumped so hard that its gain factor is greater than the loss factor which is introduced by the output coupler mirror. This creates a scenario where most of the laser light is confined within the laser cavity which allows multiple reflections of the laser light field to occur between the mirrors. This leads to a steady state regime where the gain exactly compensates the output coupling losses and therefore the laser start to emit the laser light continuously as shown in Fig. 1.2.2.

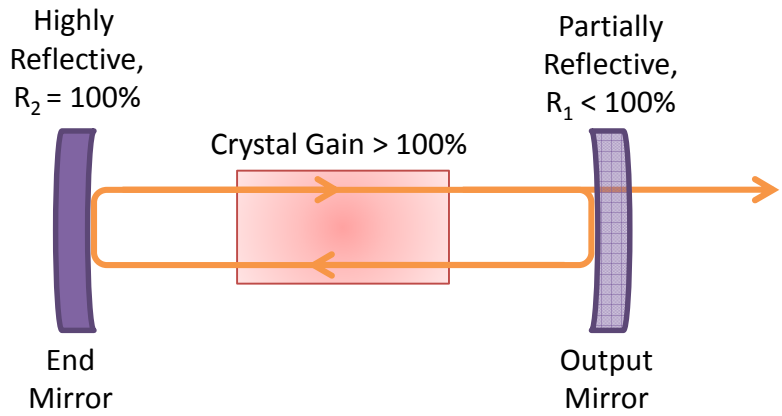

Fig. 1.2.2: Schematic principle of laser resonator where the gain factor should always be greater than the output coupler mirror loss for every round trip.

The definition of an optical laser resonator in most cases includes the gain medium as we have shown above, but an optical laser resonator can also be viewed without the active medium and such a laser resonator is called a passive resonator. The use of a passive resonator is to investigate and determine the steady state solution of the oscillating spatial field structure inside the resonator without the complication and challenges of nonlinear effects on the oscillating field which are introduced by the inclusion of the gain medium.

A stable passive laser cavity as shown in Fig. 1.2.3 in most cases consists of two mirrors with a radius of curvature R_1 and R_2 separated by an optical distance $L = nL_0$, where L_0 is the physical distance between the two mirrors, and n the refractive index between the two mirrors. The resonator will be termed stable, if the rays of light inside the resonator are allowed to bounce between the mirrors repeatedly over an infinite number of times along the optical axis without experiencing any diffraction losses. This means that in the case shown in Fig. 1.2.3, the wave front of an electric field that oscillates in such a cavity matches the radius of curvature of the mirrors, for the field to experience no losses, and for it to be reproduced at every round-trip within the resonator. The self-reproducing of such spherical waves or fields inside the resonator is called an eigenmode or mode of the resonator.

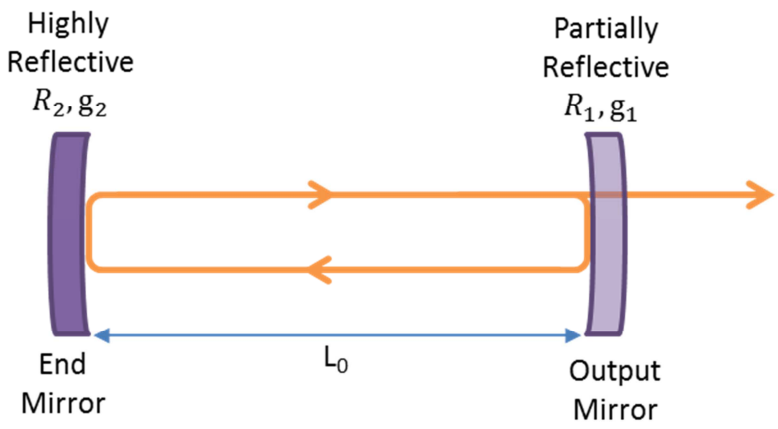

Fig. 1.2.3: The general optical resonator stability is determined by the g-parameter of the mirrors and the resonator length L_0.

The condition for a stable resonator is given by the g-parameter of the resonator mirrors to be:

$$0 < g_1 g_2 < 1;$$

where $g_1 = 1 - \frac{L}{R_1}$ and $g_2 = 1 - \frac{L}{R_2}$.

In the resonator shown above in Fig. 1.2.3, the radii of curvature R_1 and R_2 are positive since the mirrors are concave. The radius of curvature is negative for convex mirrors. For stable resonators the most fundamental eigenmode is the Gaussian beam. The stability of optical resonators when different types of mirrors are used can be determined by a point in the g_1, g_2 coordinate plane on a g-diagram as shown in Fig. 1.2.4. The stability region for optical resonators is limited by the coordinate axes and the hyperbolas, $g_2 = \pm\frac{1}{g_1}$. The resonators corresponding to points on the boundary of the stability region do not generate Gaussian beam eigenmode, they represent a different and unique class of resonators. The confocal resonator is an exception, since in this case the stability parameter $g_2 = g_1 = 0$, and this is considered to be a stable resonator.

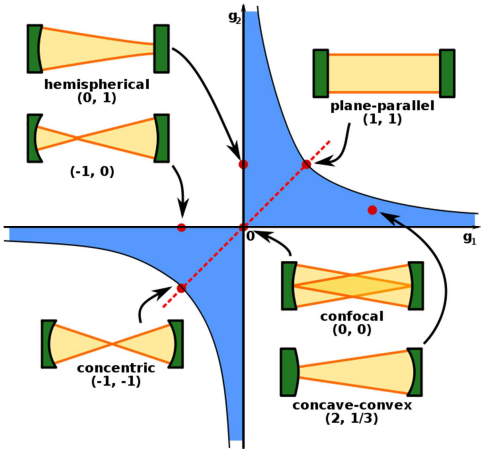

Fig 1.2.4: The stability diagram of optical resonators with spherical mirrors where the shaded region indicates stable resonators [1.53].

The electric field $E_i(x, y)$ eigensolution distribution inside the resonator on each mirror i such that it reproduces itself after each round trip is described by the Kirchhoff integral equation as:

$$\gamma E_i(x_2, y_2) = i\frac{e^{-ikL}}{2Lg_j\lambda_0}\iint E_i(x_1, y_1)e^{\frac{i\pi}{2Lg_j\lambda_0}\left(G\left(x_1^2+y_1^2+x_2^2+y_2^2\right)-2(x_1x_2+y_1y_2)\right)}dx_1dy_1,$$

where the optical stable parameter $G = 2g_1g_2 - 1$, indices $i, j = 1,2$ with $i \neq j$; and $k = \frac{2\pi}{\lambda_0}$, where λ_0 is the vacuum wavelength [1.22].

The solutions to the above integral equation represent the eigenmodes of the resonator and there can be an infinite numbers of such eigenmodes that can exist inside the resonator. The mode profile

shapes of such eigenmodes do not change while oscillating inside the resonator; they could only experience a decrease in amplitude gain due to diffraction losses. The loss factor, $|\gamma|$, which represents the fraction of the initial gain of the mode that is lost after reflecting on the mirror during the round trip travel; could be used to select a certain eigenmode profile to oscillate inside the resonator. This is done by increasing the loss factor on all other eignemodes not supported by the laser resonator. For an eigenmode that has zero loss, $|\gamma| = 1$, and for an eigenmode that experiences large amount of loss, $\gamma = 0$. The favouring of one eigenmode to have zero loss over an infinite number of roundtrips compared to the rest of other eigenmodes that experience maximum loss is termed resonance condition of the optical resonator, since it will lead to a steady state in which a chosen single mode would end up oscillating inside the resonator as shown in the schematic Fig. 1.2.5.

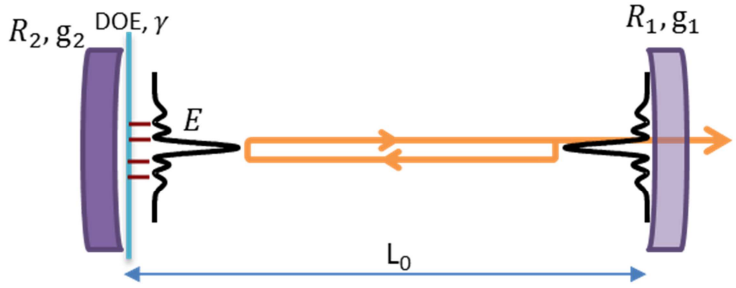

Fig.1.2.5: Schematic of the electrical field $E(x, y)$ at steady-state that reproduces itself at every round trip inside the resonator.

The loss factor mechanism for selecting a particular resonant eigenmode inside the resonator could be performed by either introducing an amplitude mask or a phase mask to select and shape a particular eigenmode profile to be the only mode oscillating inside the resonator. In the schematic diagram above, the eiffractive optical element (DOE) is used to introduce a loss factor mechanism that has maximum diffraction losses at the zero's of a Laguerre polynomial, thereby supporting a Laguerre-Gaussian mode that matches the DOE mask. The amplitude beam shaping technique is discussed in Chapter 3 and the phase beam shaping technique in Chapter 4, where both of these techniques are explored using a spatial light modulator (SLM).

1.3. Lowest-order TEM_{00} mode solution for optical resonators

The Helmholtz paraxial wave equation (Eq. 1.3.1) will be used to derive the lowest-order TEM_{00} mode solution see[1.4], since it describes the optical field of light inside the laser resonator that has

narrow transverse profiles, periodic propagation within the laser resonator and it electrical field is mainly distributed along the axis of propagation. The paraxial wave equation is:

$$\nabla_t^2 u - i2k\frac{\partial u}{\partial z} = 0; \tag{1.3.1}$$

where ∇ is the transverse Laplacian operator; u the optical field of light that has low divergent and does not vary fast along the z direction; and k is the wave vector.

The transverse Laplacian operator can be presented in cylindrical coordinates to be:

$$\nabla_t^2 = \frac{1}{r}\frac{\partial}{\partial r}\left(r\ \frac{\partial}{\partial r}\right) + \frac{1}{r^2}\left(\frac{\partial^2}{\partial \phi^2}\right). \tag{1.3.2}$$

Substituting the transverse Laplacian Eq. (1.3.2) into the paraxial wave equation, Eq. (1.3.1) can be represented in cylindrical symmetry as:

$$\frac{1}{r}\frac{\partial}{\partial r}\left(r\ \frac{\partial u}{\partial r}\right) + \frac{1}{r^2}\left(\frac{\partial^2 u}{\partial \phi^2}\right) - i2k\frac{\partial u}{\partial z} = 0. \tag{1.3.3}$$

The lowest-order mode is generally considered to be a Gaussian beam and the geometry of such a lower-order mode is usually considered to be of circular symmetry; and therefore the variation of ϕ in Eq. (1.3.3) equates to zero. This gives only one solution of Eq. (1.3.1), while there are many other solutions of Eq. (1.3.1) that are possible. Since we are looking for the lowest-order mode the optical field, u, will be represented as u_0 and Eq. (1.3.3) can be simplified as:

$$\frac{1}{r}\frac{\partial}{\partial r}\left(r\ \frac{\partial u_0}{\partial r}\right) - i2k\frac{\partial u_0}{\partial z} = 0. \tag{1.3.4}$$

The trial solution that would represent the lowest-order Gaussian mode should have the smallest divergence and when focused with a convex lens it should converge to a minimum radius and then diverges again. The trial solution which can represent such properties can be shown to be [1.56, 157]:

$$u_0(r,z) = e^{-iP(z)}e^{-\frac{ikr^2}{2q(z)}}, \tag{1.3.5}$$

where $P(z)$ represents the longitudinal phase of the wave; and $q(z)$ the Gaussian radial amplitude distribution of the wave which is real and the radial phase which is imaginary.

Partial differentiation of u_0 with respect to z of the second term of Eq. (1.3.4) leads to:

$$-i2k\frac{\partial u_0}{\partial z} = -i2k\left[-ie^{-iP(z)}e^{-\frac{ikr^2}{2q(z)}}\frac{dP(z)}{dz} + \frac{ikr^2}{2q^2(z)}e^{-iP(z)}e^{-\frac{ikr^2}{2q(z)}}\frac{dq(z)}{dz}\right]$$
$$= -2k\left[\frac{dP(z)}{dz} - \frac{kr^2}{2q^2(z)}\frac{dq(z)}{dz}\right]e^{-iP(z)}e^{-\frac{ikr^2}{2q(z)}}$$
$$= -2k\left[P'(z) - \frac{kr^2}{2q^2(z)}q'(z)\right]u_0. \quad (1.3.6)$$

The second partial differentiation of u_0 with respect to r of Eq. (1.3.4) leads to:

$$\frac{\partial u_0}{\partial r} = -\frac{ikr}{q(z)}e^{-iP(z)}e^{-\frac{ikr^2}{2q(z)}}$$
$$= -\frac{ikr}{q(z)}u_0. \quad (1.3.7)$$

When multiplying Eq. (1.3.7) with r it becomes:

$$r\frac{\partial u_0}{\partial r} = -\frac{ikr^2}{q(z)}u_0. \quad (1.3.8)$$

Taking a partial derivative of Eq. (1.3.8) with respect to r and substituting Eq. (1.3.7) and Eq. (1.3.8) leads to:

$$\frac{d}{dr}\left(r\frac{\partial u_0}{\partial r}\right) = -\frac{ikr^2}{q(z)}\left[-\frac{ikr}{q(z)}\right]u_0 - \frac{i2kr}{q(z)}u_0.$$
$$= -\frac{k^2r^3}{q^2(z)}u_0 - i\frac{2kr}{q(z)}u_0.$$
$$= -\left[\frac{k^2r^3}{q^2(z)} + i\frac{2kr}{q(z)}\right]u_0. \quad (1.3.9)$$

Multiplying Eq. (1.3.9) by $\frac{1}{r}$ leads to the first term of Eq. (1.3.4) which is:

$$\frac{1}{r}\frac{d}{dr}\left(r\frac{\partial u_0}{\partial r}\right) = -\left[\frac{k^2r^2}{q^2(z)} + i\frac{2k}{q(z)}\right]u_0. \quad (1.3.10)$$

Substituting Eq. (1.3.10) and Eq. (1.3.6) into Eq. (1.3.4) produces:

$$-\left[\frac{k^2r^2}{q^2(z)} + i\frac{2k}{q(z)}\right]u_0 - 2k\left[P'(z) - \frac{kr^2}{2q^2(z)}q'(z)\right]u_0 = 0$$

$$-\left[\frac{k^2r^2}{q^2(z)}+i\frac{2k}{q(z)}\right]u_0-\left[2kP'(z)-\frac{k^2r^2}{q^2(z)}q'(z)\right]u_0=0$$

$$r^2\left[\frac{k^2}{q^2(z)}(q'(z)-1)\right]u_0-2k\left[P'(z)+\frac{i}{q(z)}\right]u_0=0. \quad (1.3.11)$$

For Eq. (1.3.11) to be true for any r value, provided that the u_0 does not become zero, then to equate the coefficients in r on either side of the equation to make it zero becomes:

$$q'(z)-1=0 \quad => \quad q'(z)=1 \quad (1.3.12)$$

and

$$P'(z)+\frac{i}{q(z)}=0 \quad => \quad P'(z)=\frac{-i}{q(z)}. \quad (1.3.13)$$

Solving for $q(z)$ in Eq. (1.3.12) results in:

$$q'(z)=1$$
$$\int_{q_0}^{q(z)}dq(z)=\int_{\infty}^{z}dz$$
$$q(z)-q_0=z$$
$$q(z)=q_0+z \quad (1.3.14)$$

where q_0 is the constant of integration which is given by the value q at the focal spot of the beam at $z=0$. At the focal spot of the beam, its wavefront is usually considered to be plane, which means that the radial part of the trial solution should be forced to become real. This is achieved by setting q_0 to become imaginary. This is done by making $q_0=iz_R$, where z_R is a real parameter term with dimensions of length, which makes $q(z)$ in Eq. (1.3.15) to become:

$$q(z)=z+iz_R. \quad (1.3.15)$$

Since the trial solution of Eq. (1.3.5), the term $q(z)$ is given as $\frac{1}{q(z)}$. Then Eq. (1.3.15) can be written as:

$$\frac{1}{q(z)}=\frac{1}{z+iz_R}$$
$$=\frac{z}{z^2+{z_R}^2}-i\frac{z_R}{z^2+{z_R}^2} \quad (1.3.16)$$

Where the first term in Eq. (1.3.16) would represent the real part and the second term the imaginary part of $\frac{1}{q(z)}$. The above equation could be simplified further by making the real part to be equal to $\frac{1}{R(z)}$ and also introducing a new parameter $w(z)$ on the imaginary part, such that Eq. (1.3.16) becomes:

$$\frac{1}{q(z)} = \frac{1}{R(z)} - i\frac{2}{k\,w^2(z)} \tag{1.3.18}$$

where the radius of curvature $R(z)$ is,

$$R(z) = \frac{z^2 + {z_R}^2}{z}$$

$$R(z) = z\left[1 + \frac{{z_R}^2}{z^2}\right] \tag{1.3.19}$$

and

$$w^2(z) = \frac{2}{k\,z_R}[{z_R}^2 + z^2]$$

$$w^2(z) = \frac{2\,z_R}{k}\left[1 + \frac{z^2}{{z_R}^2}\right] \tag{1.3.20}$$

where

$$z_R = \frac{\pi\,w_0^2}{k\lambda} \tag{1.3.21}$$

The trial solution of Eq. (1.3.5) is modified further by substituting Eq. (1.3.18) making it to become:

$$u_0 = e^{-iP(z)}e^{-\frac{ikr^2}{2}\left(\frac{1}{R(z)} - i\frac{2}{k\,w^2(z)}\right)}$$

$$u_0 = e^{-iP(z)}e^{-\frac{r^2}{w^2(z)}}e^{-\frac{ikr^2}{2R(z)}} \tag{1.3.22}$$

where the real term $e^{-\frac{r^2}{w^2(z)}}$ is the Gaussian amplitude field profile along z with width $w(z)$ which is referred to as the beam radius. When r is equal to zero, the value of $w(z)$ is considered to be at its minimum point and is known as the waist size, w_0.

The longitudinal phase factor $P'(z)$ included in the trial solution in Eq. (1.3.5) can be determined by substituting Eq. (1.3.15) into Eq. (1.3.13) giving:

$$P'(z) = \frac{-i}{z + i\,z_R}$$

$$\frac{dP(z)}{dz} = \frac{-i}{z + i\,z_R} \tag{1.3.23}$$

Multiplying both sides of Eq. (1.3.23) with i and integrating results:

$$i\,dP(z) = \frac{-i}{z + i\,z_R}dz$$
$$i\int_0^{P(z)} dP(z) = \int_0^z \frac{1}{z + i\,z_R}dz$$
$$i\,P(z) = \log_e(z + i\,z_R) + C \tag{1.3.24}$$

where C is the integration constant. Since on the trial solution for the lowest-order Gaussian mode the longitudinal phase, $P(z)$ of the beam is assumed always to be zero at the minimum waist size, i.e. at $z = 0$. Therefore when:

$$P(z = 0) = 0,$$

the integration constant C in Eq. (1.3.24) becomes:

$$0 = \log_e(z\ + i\,z_R) + C$$
$$C = -\log_e(i\,z_R). \tag{1.3.25}$$

This means Eq. (1.3.24) can be simplified by substituting Eq. (1.3.25) to become:

$$i\,P(z) = \log_e(z + i\,z_R) + -\log_e(i\,z_R)$$
$$i\,P(z) = \log_e\left(1 + i\,\frac{z}{z_R}\right). \tag{1.3.26}$$

To simplify Eq. (1.3.26) we use an identity of the Argand diagram method which displays complex numbers as follows:

$$a + ib = (a^2 + b^2)^{\frac{1}{2}}\,e^{i\,\tan^{-1}\left(\frac{b}{a}\right)}. \tag{1.3.27}$$

If we make the constant in Eq. (1.3.27) to be:

$$a = 1 \text{ and } b = \frac{z}{z_R},$$

and substitute this into Eq. (1.3.27) we get:

$$1 + i\frac{z}{z_R} = \left(1 + \left(\frac{z}{z_R}\right)^2\right)^{\frac{1}{2}}\ e^{i\,\tan^{-1}\left(\frac{z}{z_R}\right)}. \tag{1.3.27}$$

The longitudinal phase, $P(z)$ of the beam in Eq. (1.3.26) can then be simplified by substituting Eq. (1.3.27) to become:

$$i\,P(z) = \log_e\left(\left(1+\left(\frac{z}{z_R}\right)^2\right)^{\frac{1}{2}}\; e^{\,i\,\tan^{-1}\left(\frac{z}{z_R}\right)}\right)$$

$$i\,P(z) = \log_e\left(1+\left(\frac{z}{z_R}\right)\right)^{\frac{1}{2}} - i\,\tan^{-1}\left(\frac{z}{z_R}\right)$$

$$e^{-i\,P(z)} = \frac{1}{\left(1+\left(\frac{z}{z_R}\right)\right)^{\frac{1}{2}}}\; e^{\,i\,\tan^{-1}\left(\frac{z}{z_R}\right)}. \tag{1.3.28}$$

Eq. (1.3.28) can still be simplified further by substituting Eq. (1.3.20) and Eq. (1.3.21) to make it become:

$$e^{-i\,P(z)} = \frac{w_0}{w(z)}\; e^{\,i\,\tan^{-1}\left(\frac{z}{z_R}\right)}. \tag{1.3.29}$$

Eq. (1.3.29) can now be substituted into Eq. (1.3.22) to cast it into its final form:

$$u_0(r,z) = \frac{w_0}{w(z)}\; e^{\,i\,\tan^{-1}\left(\frac{z}{z_R}\right)} e^{-\frac{r^2}{w^2(z)}} e^{-\frac{ikr^2}{2R(z)}}. \tag{1.3.30}$$

The Helmholtz paraxial approximation wave equation in Eq. (1.3.1) that represents a mode that has a combination of a plane wave and some transverse variations which does not change much as the field of the mode propagates can be represented as:

$$E(r,\phi,z) = E_0\,u(r,\phi,z)\,e^{-ikz}, \tag{1.3.31}$$

where E_0 is the amplitude of the field at $r=\phi=z=0$. Substituting Eq. (1.3.30) into Eq. (1.3.31) leads to the total solution for the paraxial wave equation for the smallest-order Gaussian mode to be:

$$E(r,\phi,z) = E_0\,\frac{w_0}{w(z)} e^{-\frac{r^2}{w^2(z)}}\; e^{-\frac{ikr^2}{2R(z)}} e^{-ikz}\; e^{\,i\,\tan^{-1}\left(\frac{z}{z_R}\right)},$$

which when simplified becomes:

$$E(r,\phi,z) = E_0\,\frac{w_0}{w(z)} e^{-\frac{r^2}{w^2(z)}}\; e^{-\frac{ikr^2}{2R(z)}}\, e^{-i\left[kz-\tan^{-1}\left(\frac{z}{z_R}\right)\right]}, \tag{1.3.32}$$

where $E_0 \frac{w_0}{w(z)} e^{-\frac{r^2}{w^2(z)}}$ is the amplitude; $e^{-\frac{ikr^2}{2R(z)}}$ the radial phase; and $e^{-i\left[kz-\tan^{-1}\left(\frac{z}{z_R}\right)\right]}$ is the longitudinal phase part of the smallest-order Gaussian mode solution. To emphasise, the propagation of a Gaussian beam profile is governed by the beam waist, $w(z)$ the radius of curvature of the wavefront, $R(z)$ and the Gouy phase shift, Φ,

$$\Phi = \tan^{-1}\left(\frac{z}{z_R}\right), \tag{1.3.33}$$

where z_R is the Rayleigh range given in Eq. (1.3.21), which shows how fast the beam diverges from its centre point z_0, where the beam waist is minimum w_0. When the value of z_R is large, it means the Gaussian beam is diverging slowly and when the value is small it means the beam is diverging fast.

The electrical field intensity of a beam is given as:

$$I(r, \phi, z) = |E(r, \phi, z)|^2. \tag{1.3.34}$$

The electrical field intensity of the lowest-order Gaussian beam can be found by substituting Eq. (1.3.32) into Eq. (1.3.34) and be shown to be:

$$I(r, \phi, z) = E_0^2 \left(\frac{w_0}{w(z)}\right)^2 e^{-\frac{2r^2}{w^2(z)}}. \tag{1.3.35}$$

The intensity has a Gaussian distribution, with the peak occurring at r_0 which is at the centre and decreasing monotonically with an increase in *r*, evident in Fig. 1.3.1 (a).

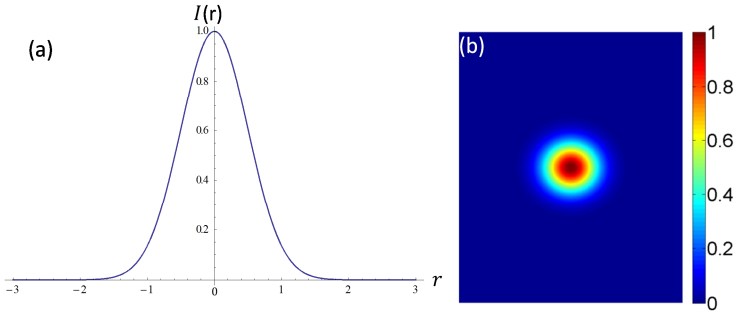

Fig. 1.3.1: (a) Cross-sectional profile and (b) transverse profile of the intensity of the lowest-order Gaussian beam.

Other solutions to the paraxial form of the Helmholtz equation exist such that when the equation is solved using Cartesian coordinates a family of solutions is obtained known as the Hermite–Gaussian

modes and when the equation is solved in circular cylindrical coordinates the solutions are known as Laguerre–Gaussian modes. For both families, the lowest-order solution describes a Gaussian beam, while higher-order solutions describe higher-order transverse modes in an optical resonator.

In the Chapters which follow, we show that Gaussian beams are just one possible solution to the paraxial wave equation and that many other combination sets of orthogonal solutions are possible for modelling laser beams which can be generated by laser resonators. In general, we see that if a complete basis set of solutions is chosen, then any real laser beam can be described as a superposition of solutions from the initial chosen set. The design of the laser cavity in most cases determines which basis set of solutions is intended to be an output of the laser. Hermite-Gaussian modes are generally more common since many laser systems have mirrors that represent Cartesian reflection symmetry in the plane perpendicular to the beam's propagation direction.

1.4. Hermite-Gaussian beams

The Gaussian mode is not the only solution to the paraxial approximation of the Helmholtz wave equation; there are many other solutions that exist, such as the Hermite-Gaussian (HG) mode whose electric field can be represented as [1.4]:

$$E_{m,n}(x,y,z) = E_0 \, \frac{w_0}{w(z)} \, H_m\left(\sqrt{2}\frac{x}{w(z)}\right) H_n\left(\sqrt{2}\frac{x}{w(z)}\right) e^{-\frac{x^2+y^2}{w^2(z)}} \, e^{-\frac{ik(x^2+y^2)}{2R(z)}} \, e^{-i[kz-\Phi(m,n,z)]}, \qquad (1.4.1)$$

where $\Phi(m,n,z)$ is the Gouy phase for the HG mode and is given as:

$$\Phi(m,n,z) = (m+n+1)\tan^{-1}\left(\frac{z}{z_R}\right) \qquad (1.4.2)$$

and the other parameters, such as the radius of curvature $R(z)$ and the beam waist $w(z)$, have been given in Eq. (1.3.19) and Eq. (1.3.21) as propagation parameter of Gaussian beams. This is because HG modes are superposition solutions of Hermite polynomials and the Gaussian parameters which is why they are called Hermite-Gaussian modes. The Hermite-Gaussian modes have polynomial indices of m and n for x and y in Cartesian coordinates. The lowest-order Hermite-Gaussian mode has indices equal to zero, $m = n = 0$ which results in the lowest-order Gaussian mode of TEM_{00} or HG_{00}.

The Hermite-Gaussian intensity profiles of Eq. (1.4.1) with different combination of indices m and n are shown in Fig. 1.4.1. The HG intensity profiles were generated using the digital laser that is discussed in Chapter 4. The number of nodal lines in the intensity profile depends on the values of m and n indices. The index m determines the number of nodal lines along the y axis, whereas n determines the nodal lines along the x axis.

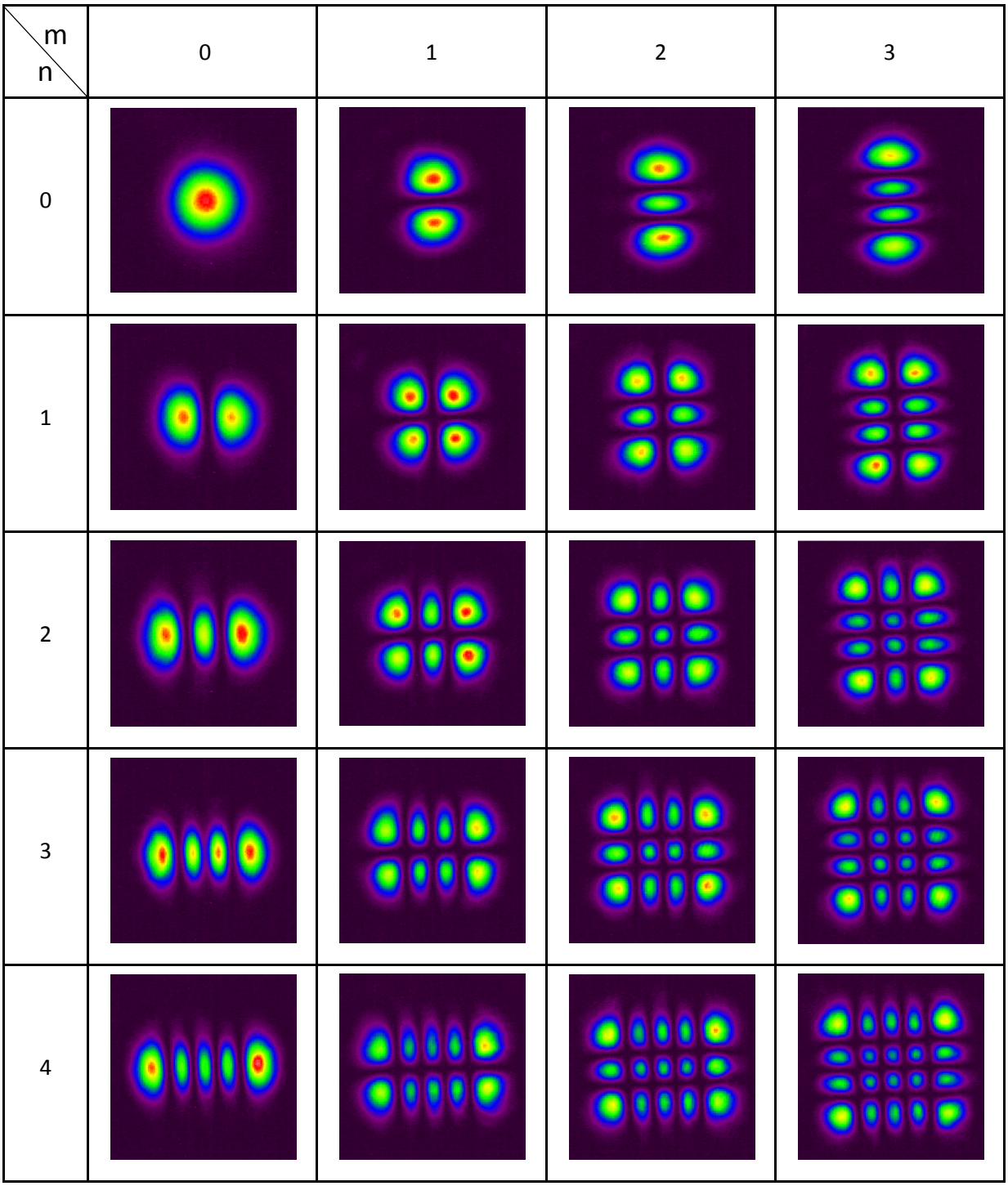

Fig. 1.4.1: The transverse intensity profiles of HG modes with the corresponding indices of m and n.

1.5. Laguerre-Gaussian beams

The previously discussed Gaussian mode is not the only solution to the paraxial approximation of the Helmholtz wave equation; there are many other solutions that exist, such as the Laguerre-Gaussian (LG) mode whose electric field can be represented as:

$$E_{p,l}(r,\phi,z) = E_0 \, \frac{1}{w(z)} \sqrt{\frac{2p!}{\pi(|l|+p)!}} \left(\frac{\sqrt{2}\, r}{w(z)}\right)^{|l|} L_p^{|l|}\left(\frac{2\, r^2}{w^2(z)}\right) e^{-\frac{r^2}{w^2(z)}} \, e^{-\frac{ikr^2}{2R(z)}} \, e^{-i[\Phi(p,l,z)-l\phi]}, \qquad (1.5.1)$$

where $\Phi(p,l,z)$ is the Gouy phase for the Laguerre-Gaussian mode and is given by:

$$\Phi(p,l,z) = (2p+l+1)\tan^{-1}\left(\frac{z}{z_R}\right), \qquad (1.5.2)$$

and the other parameters, such as the radius of curvature $R(z)$ and the beam waist $w(z)$, have been defined in Eq. (1.3.19) and Eq. (1.3.21) as the propagation parameter of Gaussian beams. This is because Laguerre-Gaussian modes are superposition solutions of Laguerre polynomials and Gaussian parameter and that is why they are called Laguerre-Gaussian modes. The Laguerre-Gaussian modes have indices p and l which represents radial coordinate r and azimuthal angle ϕ respectively. The lowest-order Laguerre-Gaussian mode has indices equal to zero, $p = l = 0$ which results in a simple Gaussian mode of TEM_{00} or LG_{00}.

The Laguerre-Gaussian intensity profiles of Eq. (1.5.1) with different combination of indices of p and l are shown in Fig. 1.5.1. The LG intensity profiles were generated using the digital laser that is discussed in Chapter 4. The intensity profile of Laguerre-Gaussian beams has a central null for $l \neq 0$ and the central null diameter size increases as the value of l increases as shown in Fig. 1.5.2. The radial beam width of Laguerre-Gaussian beams is also shown to increase with an increase of p or l indices, where the value of the index p denotes the number of intensity concentric rings of that Laguerre-Gaussian mode as shown by Fig. 1.5.3. The increase in beam width of Laguerre-Gaussian modes from the fundamental lowest-order Gaussian mode is given as:

$$w_{p,l} = w_0\sqrt{2p+l+1} \qquad (1.5.3)$$

where w_0 is the beam width of the fundamental lowest-order Gaussian mode.

P / l	0	1	2	3
0	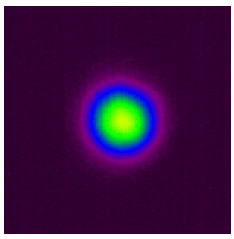	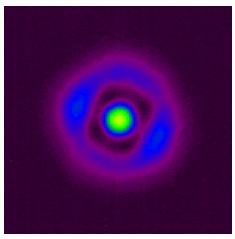	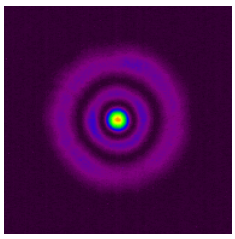	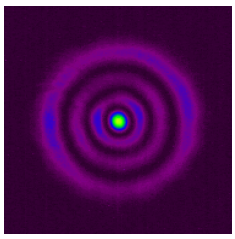
1	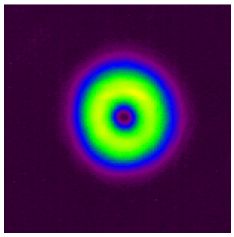	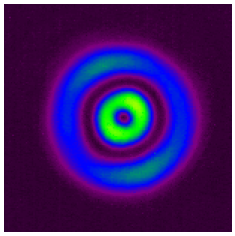	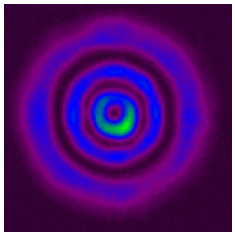	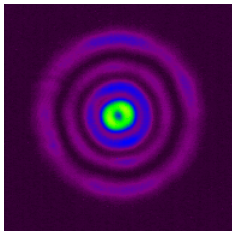
2	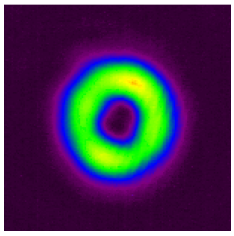	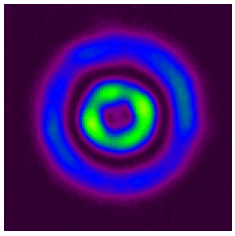	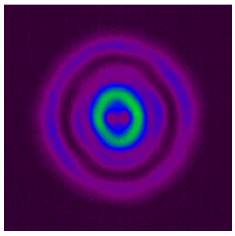	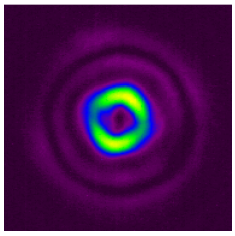
3	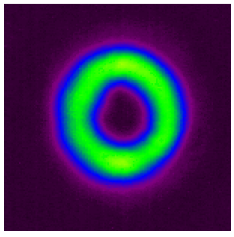	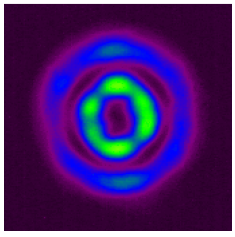	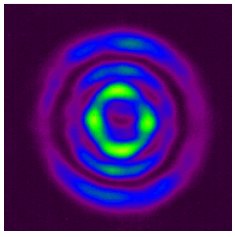	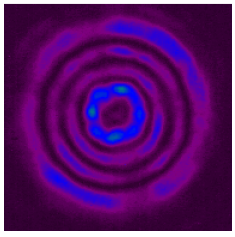
4	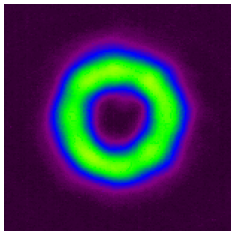	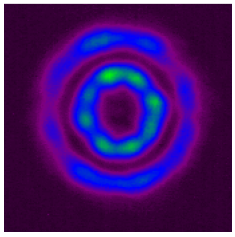	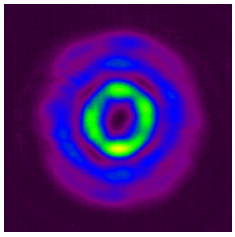	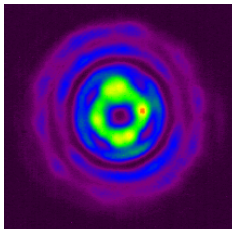

Fig. 1.5.1: The transverse intensity profiles of Laguerre-Gaussian modes with the corresponding indices of p and l.

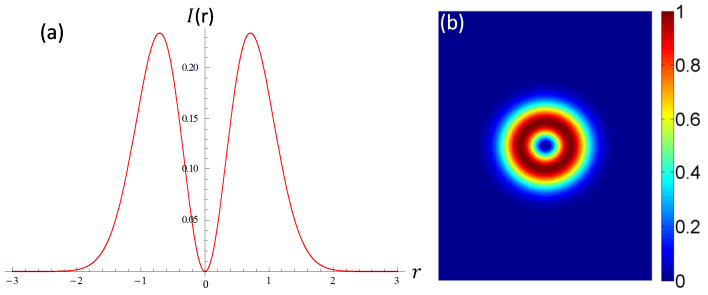

Fig. 1.5.2: (a) Cross-sectional profile and (b) transverse profile of the intensity of a $LG_{0,1}$ beam.

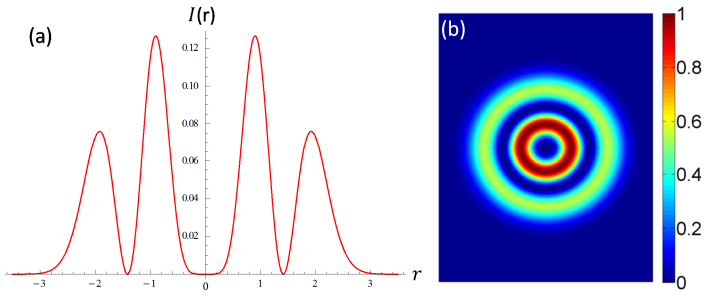

Fig. 1.5.3: (a) Cross-sectional profile and (b) transverse profile of the intensity of a $LG_{1,2}$ beam.

The superposition of two Laguerre-Gaussian modes also corresponds to a different allowed mode of the resonator. The single Laguerre-Gaussian mode that is produced by the laser resonator contains two coherent Laguerre-Gaussian modes that have two opposite azimuthal orders of $+l$ and $-l$ (see Chapter 6).

The electric field expression of the coherent superposition of two Laguerre-Gaussian modes of radial order p with opposite azimuthal order $\pm l$ is given as:

$$E_{p,l}(r,\phi,z) = E_{p,-l}(r,\phi,z) + E_{p,+l}(r,\phi,z)$$

$$= \left[\sqrt{\frac{2}{\pi(|l|)!}}\frac{w_0}{w(z)}\left(\frac{\sqrt{2}r}{w(z)}\right)^{|l|}\right] e^{\left(\frac{-r^2}{w^2(z)}\right)} e^{\left(\frac{-ikr^2}{2R(z)}\right)} e^{\left(-i(2p+|l|+1)\arctan\left(\frac{z}{z_r}\right)\right)} \left(e^{(il\phi)} + e^{(-il\phi)}\right), \qquad (1.5.4)$$

The intensity profiles of such superposition of Laguerre-Gaussian modes are shown Fig. 1.5.4 and they have a central null when the indices $l \neq 0$ and the central null diameter size increases as the value of $\pm l$ indices increases. The radial intensity beam width of the Laguerre-Gaussian beams is also shown to increase with an increase to the values of p or $|l|$ indices. The value of the radial index p denotes the number of intensity concentric rings the mode possesses, and the value of the index l

denotes the number of nodal lines along the radial coordinate. The coherent LG mode intensity profiles in Fig. 1.5.4 were generated using the digital laser that is discussed in Chapter 4.

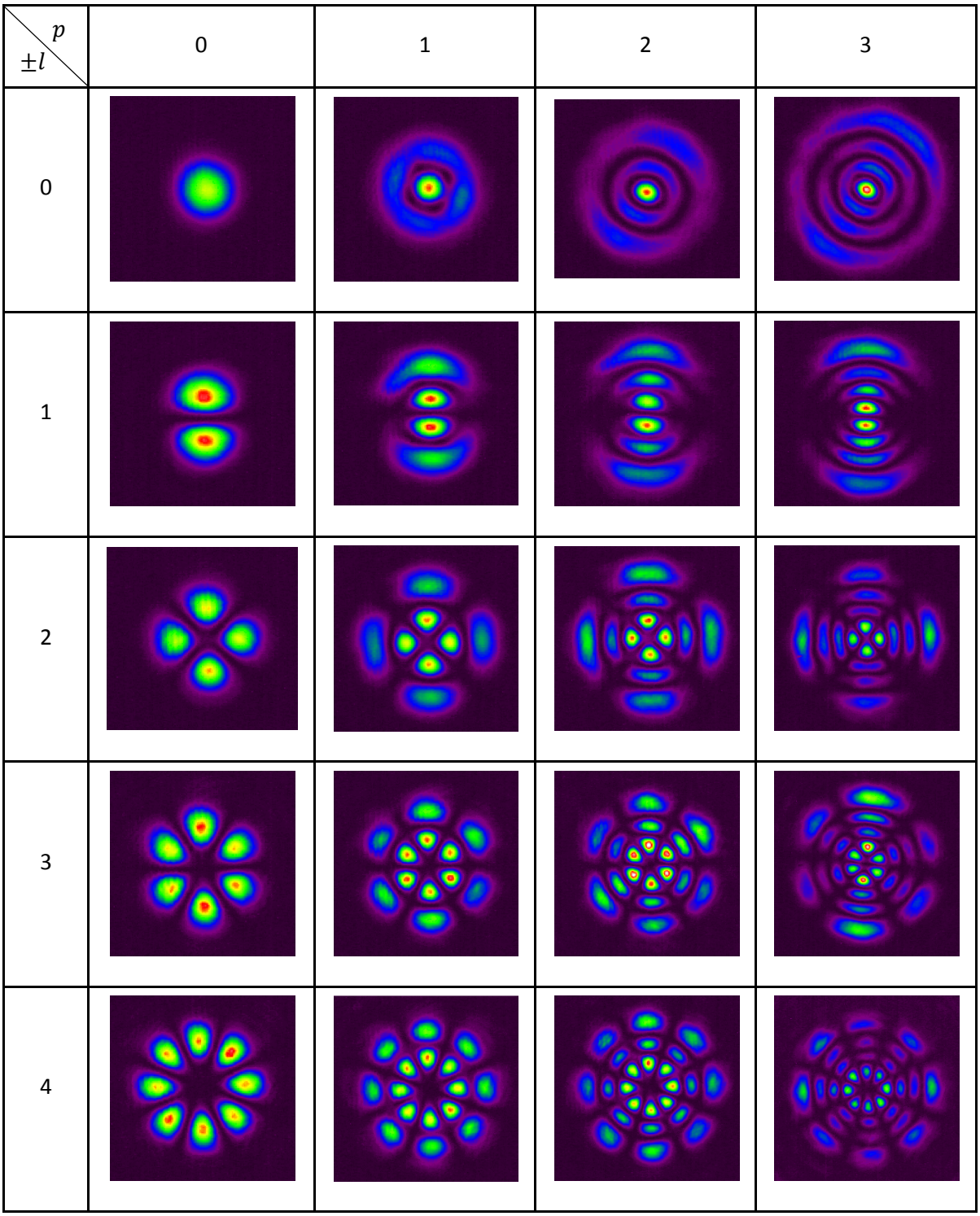

Fig. 1.5.4: The transverse intensity profiles of the superposition of two coherent Laguerre-Gaussian modes with the corresponding indices of p and $|l|$.

1.6. Conclusions

We started the Chapter with an overview of the work covered in this thesis, followed by the background history of mode selection in diode pumped solid state laser resonators (DPSSLR). This was followed by the theoretical implementation of the Helmholtz equation in the paraxial approximation to derive the lowest-order Gaussian mode. Since higher laser modes in a resonator form a basis set of the lowest-order Gaussian mode, it was important in this thesis to show how high-order modes of different families are generated, such as Hermite-Gaussian modes and Laguerre-Gaussian modes.

1.7. References

[1.1]. J. C. Maxwell, "A treatise on electricity and magnetism," (Oxford: Clarendon Press) 793 (1891).

[1.2]. A. Fox and T. Li, "Analysis of Optical Resonators Involving Focusing Elements," Bell Syst. Tech. J. **40**, 453 (1961).

[1.3]. G. Boyd and H. Kogelnik, "Diffraction Loss and Beam Size in Lasers with Spherical Mirrors," Bell Syst. Tech. J. **41**, 1347 (1962).

[1.4]. H. Kogelnik and T. Li, "Laser Beams and Resonators," Appl. Opt. **5**, 1550 (1966).

[1.5]. H. Kogelnik and W. Rigrod, "Visual display of isolated optical-resonator modes," Proc. IRE **50**, 220 (1962).

[1.6]. W. Rigrod, "Isolation of Axi-symmetrical Optical-Resonator Modes," Appl. Phys. Lett. **2**, 51 (1963).

[1.7]. R. Oron, N. Davidson, E. Hasman, and A. Friesem, "Transverse Mode Shaping and Selection in Laser Resonators," Progress in Optics, **42** (6), 325 (2001).

[1.8]. S. F. Pereira, M. B. Willemsen, M. P. van Exter, and J. P. Woerdman, "Pinning of daisy modes in optically pumped vertical-cavity surface-emitting lasers," Appl. Phys. Lett. **73**, 2239 (1998).

[1.9]. Q. Deng, H. Deng, and D. G. Deppe, "Radiation fields from whispering-gallery modes of oxide-confined vertical-cavity surface emitting lasers," Opt. Lett. **22**, 463 (1997).

[1.10]. Y. F. Chen, Y. P. Lan, and S. C.Wang, "Generation of Laguerre-Gaussian modes in fiber-coupled laser diode end-pumped lasers," Appl. Phys. B **72**, 167 (2001).

[1.11]. F. T. Arecchi, "Optical morphogenesis: pattern formation and competition in nonlinear optics," Physica D **86**, 297 (1995).

[1.12]. S. A. Akhmanov, M. A. Vorontsov, V. Yu. Ivanov, A. V. Larichev, and N. I. Zheleznykh, "Controlling transverse wave interactions in nonlinear optics: generation and interaction of spatiotemporal structures," J. Opt. Soc. Am. B **9**, 78 (1992).

[1.13]. G. Grynberg, A. Maître, and A. Petrossian, "Flowerlike patterns generated by a laser beam transmitted through a rubidium cell with single feedback mirror," Phys. Rev. Lett. **72**, 2379 (1994).

[1.14]. A. Ito, Y. Kozawa, and S. Sato, "Generation of hollow scalar and vector beams using a spot-defect mirror," J. Opt. Soc. Am. A **27**, 2072 (2010).

[1.15]. I. A. Litvin, L. Burger, and A. Forbes, "Petal-like modes in Porro prism resonators," Opt. Express **15**, 14065 (2007).

[1.16]. R. Oron, Y. Danziger, N. Davidson, A. A. Friesem, and E. Hasman, "Discontinuous phase elements for transverse mode selection in laser resonators," Appl. Phys. Lett. **74**, 1373 (1999).

[1.17]. A. A. Ishaaya, N. Davidson, G. Machavariani, E. Hasman, and A. A. Friesem, "Efficient selection of high-order Laguerre-Gaussian modes in a Q-switched Nd:YAG laser," IEEE J. Quantum Electron. **39**, 74 (2003).

[1.18]. A. A. Ishaaya, N. Davidson, and A. A. Friesem, "Very high order pure Laguerre-Gaussian mode selection in a passive Q-switched Nd:YAG laser," Opt. Express **13**, 4952 (2005).

[1.19]. L. Burger and A. Forbes, "Kaleidoscope modes in large aperture Porro prism resonators," Opt. Express **16**, 12707 (2008).

[1.20]. Y. Senatsky, J. F. Bisson, J. Li, A. Shirakawa, and M. Thirugnansambandam, "Laguerre-Gaussian modes selection in diode-pumped solid-state lasers," Opt. Rev. **19**, 201 (2012).

[1.21]. W. Koechner, "Solid-State Laser Engineering", 5th ed. (Springer, 1999).

[1.22]. N. Hodgson and H.Weber, "Laser Resonators and Beam Propagation", 2nd ed. (Springer, 2005).

[1.23]. A. Siegman, "Lasers," University Science Books, (1986).

[1.24]. T. Y. Fan and R. L. Byer, "Diode laser-pumped solid-state lasers," IEEE J. Quantum Electron. **24**, 895 (1988).

[1.25]. A. Mak and V. Ustyugov, "Solid-State Lasers with Longitudinal Laser-Diode Pumping: Efficiency, Scaling, Dynamics, and Noise," Laser Phys. **6**, 431 (1996).

[1.26]. D. Hanna and W. Clarkson: A Review of Diode-Pumped Lasers, ed. D. Finlayson and B. Sinclair (Taylor & Francis, New York, 1999) Advances in Lasers and Applications.

[1.27]. R. L. Byer, "Diode pumped solid state lasers," in Conference on Lasers and Electro-Optics/Pacific Rim 2009 (OSA, 2009), paper MD1_1.

[1.28]. J. Dong, K. Ueda, H. Yagi, and A. A. Kaminskii, "Laser-diode pumped self-Q-switched microchip lasers," Opt. Rev. **15**, 57 (2008).

[1.29]. L. Allen, M. W. Beijersbergen, R. J. C. Spreeuw, and J. P. Woerdman, “Orbital angular momentum of light and the transformation of Laguerre-Gaussian laser modes,” Phys. Rev. A **45**, 8185 (1992).

[1.30]. T. Omatsu, K. Chuj, K. Miyamoto, M. Okida, K. Nakamura, N. Aoki, and R. Morita, “Laguerre-Gaussian modes selection in diode-pumped solid-state lasers,” Opt. Express **18**, 17967 (2010).

[1.31]. G. Molina-Terriza, J. Torres, and L. Torner, “Management of the angular momentum of light: preparation of photons in multidimensional vector states of angular momentum,” Phys. Rev. Lett. **88**, 013601 (2001).

[1.32]. T. Kuga, Y. Torii, N. Shiokawa, T. Hirano, Y. Shimizu, and H. Sasada, “Novel optical trap of atoms with a doughnut beam,” Phys. Rev. Lett. **78**, 4713 (1997).

[1.33]. M. Clifford, J. Arlt, J. Courtial, and K. Dholakia, “High-order Laguerre-Gaussian laser modes for studies of cold atoms,” Opt. Commun. **156**, 300 (1998).

[1.34]. K. Gahagan and G. Swartzlander, Jr., “Optical vortex trapping of particles,” Opt. Lett. ... “Simultaneous trapping of low-index and high-index microparticles observed with an optical-vortex trap,” J. Opt. Soc. Am. B **16**, 533 (1999).

[1.35]. J. Arlt and M. Padgett, “Generation of a beam with a dark focus surrounded by regions of higher intensity: "an optical bottle beam",” Opt. Lett. **25**, 191 (2000).

[1.36]. J. Arlt, T. Hitomi, and K. Dholakia, “Atom guiding along Laguerre—Gaussian and Bessel light beams,” Appl. Phys. B **71**, 549 (2000).

[1.37]. T. Watanabe, Y. Iketaki, T. Omatsu, K. Yamamoto, M. Sakai, and M. Fujii, “Two-point-separation in super-resolution fluores-cence microscope based on up-conversion fluorescence depletion technique,” Opt. Express **11**, 3271 (2003).

[1.38]. T. Watanabe, Y. Igasaki, N. Fukuchi, M. Sakai, S. Ishiuchi, M. Fujii, T. Omatsu, K. Yamamoto, and Y. Iketaki, “Formation of a doughnut laser beam for super resolving microscopy using a phase spatial light modulator,” Opt. Eng. **43**, 1136 (2004).

[1.39]. J. Durnin and J. Miceli, Jr., “Diffraction-free beams,” Phys. Rev. Lett. **58**, 1499 (1987).

[1.40]. R. Herman and T. Wiggins, “Production and uses of diffractionless beams,” J. Opt. Soc. Am. A **8**, 932 (1991).

[1.41]. J. Arlt and K. Dholakia, “Generation of high-order Bessel beams by use of an axicon,” Opt. Commun. **177**, 297 (2000).

[1.42]. A. Hakola, S. Buchter, T. Kajava, H. Elfstro¨m, J. Simonen, P.Pa¨a¨kko¨nen, and J. Turunen, “Bessel-Gauss output beam from a diode-pumped Nd:YAG laser,” Opt. Commun. **238**, 335 (2004).

[1.43]. D. McGloin and K. Dholakia, “Bessel beams: Diffraction in a new light,” Contemp. Phys. **46**, 15 (2005).

[1.44]. M. Bandress and J. Gutierrez-Vega: Opt. Lett. **29**, 144 (2004).

[1.45]. U. Schwarz, M. Bandres, and J. Gutierrez-Vega, “Observation of Ince-Gaussian modes in stable resonators,” Opt. Lett. **29**, 1870 (2004).

[1.46]. T. Ohtomo, K. Kamikariya, K. Otsuka, and S.-C. Chu, “Single-frequency Ince-Gaussian mode operations of laser-diode-pumped microchip solid-state lasers,” Opt. Express **15**, 10705 (2007).

[1.47]. K. Tokunaga, S.-C. Chu, H.-Y. Hsiao, T. Ohtomo, and K. Otsuka, “Spontaneous Mathieu-Gauss mode oscillation in micro-grained Nd:YAG ceramic lasers with azimuth laser-diode pumping,” Laser Phys. Lett. **6**, 635 (2009).

[1.48]. Y. Chen, Y. Lan, and S. Wang, “Generation of Laguerre-Gaussian modes in fiber-coupled laser diode end pumped lasers,” Appl. Phys. B **72**, 167 (2001).

[1.49]. Y. Chen and Y. Lan, “Dynamics of the Laguerre Gaussian TEM*0,1 mode in a solid-state laser,” Phys. Rev. A **63**, 063807 (2001).

[1.50]. R. Oron, Y. Danziger, N. Davidson, A. Friesem, and E. Hasman, “Laser mode discrimination with intra-cavity spiral phase elements,” Opt. Commun. **169**, 115 (1999).

[1.51]. A. Ishaaya, N. Davidson, G. Machavariani, E. Hasman, and A. Friesem, “Efficient selection of high-order Laguerre-Gaussian modes in a Q-switched Nd:YAG laser,” IEEE J. Quantum Electron. **39**, 74 (2003).

[1.52]. A. Ishaaya, N. Davidson, and A. Friesem, “Very high-order pure Laguerre-Gaussian mode selection in a passive Q-switched Nd:YAG laser,” Opt. Express **13**, 4952 (2005).

[1.53]. http://en.wikipedia.org/wiki/Optical_cavity

[1.54]. J. W. Goodman, “Introduction to Fourier Optics” (McGraw-Hill Publishing Company, 1968).

[1.55]. M. A. Golub, A. M. Prokhorov, I. N. Sisakian, and V. A. Soifer “Synthesis of spatial filters for investigation of the transverse mode composition of coherent radiation,” Sov. J. Quantum Electron. **9**, 1866 (1982).

[1.56]. H. A. Haus, “Waves and Fields in Optoelectronics,” Prentice Hall, Englewood Cliffs, NJ, 1984.

[1.57]. J. T. Verdeyen, “Laser Electronics,” Prentice Hall, Englewood Cliffs, NJ, 1995.

CHAPTER TWO

Modal decomposition without *a priori* scale information

2.1. Introduction

There are a number of laser systems that produce multiple arbitrary unknown laser modes such as multi-mode optical fibres and multi-mode high-power laser diodes. Specifically, for applications such as fibre communication where multimode-mode optical fibre is used, it is important to perform modal decomposition on the emitted arbitrary multi-mode beam to determine the composition amount of the superposition of modes emitted by the fibre. The technique of modal decomposition has been shown over the years [1.53, 1.54] that it can be used to extract physical properties associated with the emitted multi-mode laser beam such as the intensity of the light field, the phase and M^2, etc. The overwhelming advantages provided by performing modal decomposition technique in systems emitting multimode laser beams has been demonstrated by several experiments [1.55, 2.1–2.4] that have been performed, some with varying degree of success. More recently the technique of modal decomposition has been implemented using computer generated digital holograms to decompose modes emitted by optical fibres [2.5-2.7]. These digital holograms have also been used to determine laser beam properties such as the beam quality factor [2.8], angular momentum density [2.9, 2.10], wavefront and phase [2.11] have all been recently determined using computer generated digital holograms.

It has been shown that the modal decomposition of an arbitrary optical field may be performed without the knowledge of the initial basis function scale. But this approach has been shown not to be efficient and also not to be correctly representative of the underlying field since it produces a large quantity of modes in the expansion, even though the approach is mathematically correct. Therefore, accurate modal decomposition of arbitrary laser modes as a technique has been shown to be unfavourable without prior information of the scale parameter of the basis function. Although, there exists a unique basis function, the angular harmonics, which requires no initial scale parameter, its disadvantage is that it’s a one dimensional (azimuthal angle) basis function, which requires a scan over the second dimension (radial coordinate) to extract the core information [2.12].

In this Chapter [6.12] we demonstrate a novel modal decomposition approach using digital holograms that requires no *a priori* knowledge of the spatial scale of the modes that will lead to an optimised modal expansion. We show that by proposing a simple two-step approach of first determining the second moment size of the beam, w_0, and the beam propagation factor, M^2. We can determine the scale of the adapted set, which enables the second step of determining an optimal decomposition in the adapted mode set to be possible thereby determining the number of modes contained in the arbitrary optical field. We illustrate the power of modal decomposition without a priori scale information by successfully decomposing beams from a diode-pumped solid state laser resonator into optimised Laguerre-Gaussian mode sets. We also demonstrate that our experimental results are in good agreement with theory which illustrates the versatility of our approach.

2.2. Concept

The method of modal decomposition is used to characterise an optical field into superposition of basis functions where each basis function or mode is weighted with a complex expansion coefficient. The main purpose of modal decomposition is to acquire all the necessary information about the field so as to determine these coefficients as a one-dimensional set of coefficients. This reduces the problem to only finding the unknown modal weights (ρ_n^2) and phases ($\Delta\phi_n$) so that an unknown field $U(\boldsymbol{r})$ can be expressed as a phase dependent superposition of a finite number of modes, $\psi_n(\boldsymbol{r})$ [2.6]

$$U(\boldsymbol{r}) = \sum_{n=1}^{n_{max}} c_n \psi_n(\boldsymbol{r}) \tag{2.2.1}$$

and the orthonormal property

$$\langle \psi_n | \psi_m \rangle \; = \; \iint_{R^2} d^2 r \; \psi_n^*(r) \psi_m(r) = \boldsymbol{\delta}_{nm}, \tag{2.2.2}$$

of the basis is then used to determine the unknown coefficients

$$c_n = \rho_n \; exp(i\Delta\phi_n) \; = \langle \psi_n | U \rangle. \tag{2.2.3}$$

To determine the modal weights (ρ_n^2) and phases ($\Delta\phi n$), an experiment would be required where an optical setup for the inner product measurement would need to be performed, as we will discuss later. For optimal decomposition the method requires the knowledge of the scale of the basis for it to yield the minimum number of nonzero coefficients and this will be referred to as the adapted basis set. To date there have been no reports that describe a technique to finding this adapted set.

To illustrate the problem we consider the basis set of Laguerre-Gaussian modes LG_{pl} with radial and azimuthal indices p and l, which at the waist position maybe written as:

$$LG_{pl}(\boldsymbol{r}, w_0) = \sqrt{\frac{2p!}{\pi w_0^2 (p+|l|)!}} \left(\frac{\sqrt{2}\, r}{w_0}\right)^{|l|} L_p^{|l|}\left(\frac{2r^2}{w_0^2}\right) exp\left(\frac{-r2}{w_0^2}\right) exp(il\phi) \tag{2.2.4}$$

where $\boldsymbol{r} = (r, \varphi)$, and $L_p^{|l|}$ is the Laguerre polynomial of order p and l. The basis functions have a generally unknown intrinsic scale, w_0, which corresponds to the Gaussian fundamental mode radius. The arbitrary scalar optical field U can now be decomposed into a Laguerre-Gaussian set of any size:

$$U(\boldsymbol{r}) = \sum_{pl} c_{pl}^{a} \, \mathrm{LG}_{pl}(\boldsymbol{r}, w_a) \; = \sum_{pl} c_{pl}^{b} \, \mathrm{LG}_{pl}(\boldsymbol{r}, w_b) \tag{2.2.5}$$

where $c_{pl}^{a,b}$ denote the complex expansion coeffient for different basis set sizes w_a and w_b, respectively. From Eq. (2.2.5) it is clear that the modal spectrum c_{pl} changes with the scale of the basis set. Therefore to attain a mode set of adapted size, we propose the following simple two-step approach: (i) determine the second moment size of the beam *w* and the beam propagation ratio M^2. The scale of the adapted basis set can then be inferred [15]:

$$w_0 \; = \frac{w}{\sqrt{M^2}}, \tag{2.2.6}$$

enabling the second step, (ii) an optimal decomposition in the adapted mode set. The latter may be used to deduce the "actual" modes constituting the field, and as a check of the previously determined M^2 and w_0. It is possible to implement the first step by any ISO-compliant method [2.14], for example, a modal decomposition [2.6, 2.15], or with a recently introduced digital approach [2.16]. The main idea is to relate the unknown scale of the basis functions directly to the size of the embedded fundamental Gaussian mode, w_0 [2.13]. This comes from Eq. (2.2.4), where it is observed that the size of the Gaussian term is carried through to provide the scale of all the functions in the expansion. With this observation noted, the question becomes how to find this embedded fundamental Gaussian size from a measurement of the arbitrary input field? We exploit the fact that since the beam quality factor of a fundamental Gaussian beam is $M^2 = 1$, and since the second moment beam size for all beams scales as $w \; = \; w_0\sqrt{M^2}$ [2.13], we can infer the unknown scale by measuring the field size and its M^2. Thus while Eq. (2.2.6) is simple to implement, its impact on the ability to optimise modal decomposition is significant, as we shall show in the Chapters to follow.

2.3. Experimental methodology

The laser resonator used to generate the beams which we were studying was a stable plano-concave cavity which had a variable length adjustment of between 300 to 400 mm, and is shown as a schematic in Fig. 2.3.1.

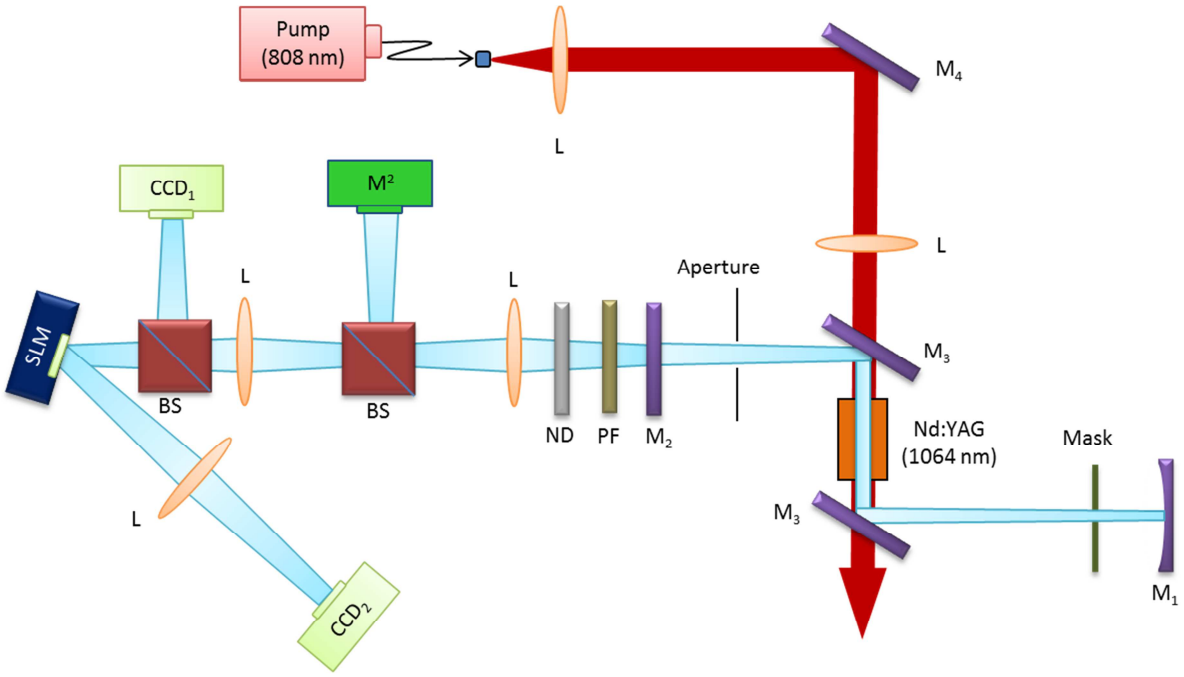

Fig. 2.3.1: Schematic experimental setup of the end-pumped Nd:YAG resonator, where the output beam is 1:1 imaged onto a camera (CCD_1) and a Spatial Light Modulator (SLM), whose diffraction pattern is observed in the far field with CCD_2. $M_{1,2}$: curved (R = 500 mm) and flat mirror ($R = \infty$), BS beam splitter, PF pump light filter, ND neutral density filter, L lens, M^2: M^2 meter.

The back reflector M_1 was chosen to be highly reflective with a curvature of $R = 500$ mm whereas the output coupler M_2 was flat with a reflectivity of 98%. The gain medium, a Nd:YAG crystal rod (30 mm × 4 mm), was end-pumped by a 75 W Jenoptik multimode fibre coupled laser diode (JOLD 75 CPXF 2P W). In order to select specific transverse modes, an intra-cavity amplitude mask was inserted near the curved end-mirror M_1. The amplitude mask used in our experiments was custom-made and consisted of lithographically produced thin aluminium absorbing rings fabricated on a 700 µm thick borosilicate glass with a 93% transmission at 1064 nm wavelength. The mask consisted of a 5 x 4 grid of ring structures, each designed to select a specific LG mode by overlapping the strong absorbing ring structures with the nulls of the desired fields. The adjustment of the resonator length

(L) between mirror M_1 and M_2, which alters the Gaussian mode size, can be viewed as a means to vary the scale parameter of the modes, while the type of ring structure on the mask selects the type of modes to be generated. The fundamental Gaussian waist size on the flat mirror satisfies $w_0^2 = (\lambda/\pi)[L(R-L)]^{1/2}$ and so each LG mode size also scales as $w_{p,l}^2 = w_0^2(2p + l + 1)$ [1.4]; note that the final field may be some superposition of these modes. Thus adjusting the resonator length results in a change in the fundamental Gaussian mode size, and hence the positions of the zeros of the LG modes. By selecting an appropriate ring structure for a given resonator length, the laser can be forced, e.g., to oscillate either on the first radial Laguerre Gaussian mode ($LG_{1,0}$), a coherent superposition of $LG_{0,\pm4}$ beams (petal profile) or a mixture of the $LG_{1,0}$ and $LG_{0,\pm4}$ modes.

The resonator output at the plane of the output coupler was relay imaged onto a CCD camera (Spiricon LBA USB L130) to measure the output beam size in the near field, and could be directed to a laser beam profiler device (Photon ModeScan1780) for measurement of the beam quality factor. The same relay telescope was used to image the beam from the output coupler to the plane of the phase-only spatial light modulator (SLM) (Holoeye HEO 1080 P). The SLM, calibrated for 1064 nm wavelength, was used for complex amplitude modulation of the light to execute an inner product measurement with a Fourier transforming lens ($f = 150$ mm). The modulation achieved by the holograms was implemented with phase-only holograms coded to achieve any desired function using standard coding approaches. In our case, the LG modes were encoded following Eq. (2.2.4) using a modulation technique suitable for a phase-only SLM [1.17]. The method used to implement the inner product measurement has been reported previously [1.7], but is briefly reviewed here with the aid of Fig. 2.3.2.

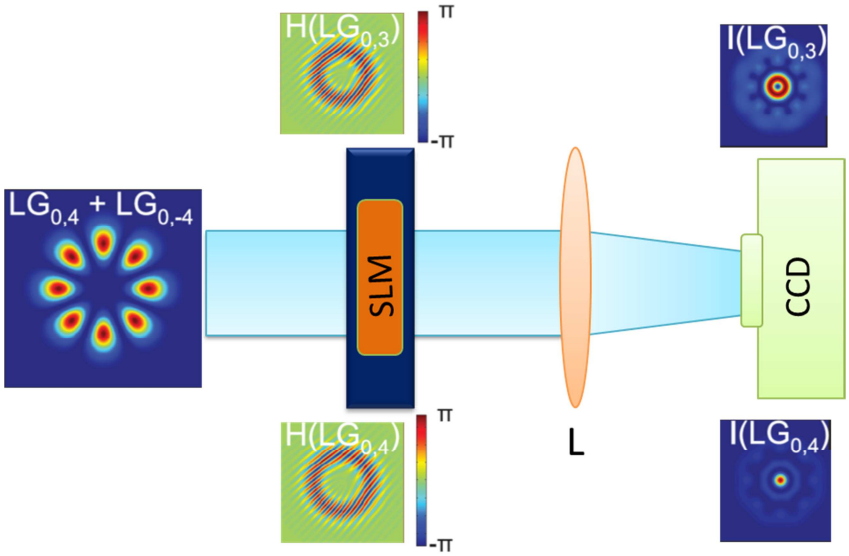

Fig. 2.3.2: Illustration of the inner product measurement scheme using a 2 f -setup. The correlation of an incoming beam with the hologram pattern (H) results in a correlation signal I at the optical axis in the back focal plane of a lens L.

Consider the case where the unknown field incident on the SLM is in fact a superposition of $LG_{0,4}$ and $LG_{0,-4}$ modes (but as yet unknown). The SLM is programmed with a series of match filters, each of which is the complex conjugate of the modal functions in the chosen expansion, e.g. the LG basis functions from Eq. (2.2.4). If the SLM (match filter) is set in the front focal plane of a lens, then in the far-field (back focal plane) the signal on the optical axis (at the origin of the detector plane) is proportional to the modal power [1.54, 1.55]. In our example, if the match filter was set to test for the modes $LG_{0,3}$ and $LG_{0,4}$, then the signal at the origin of the detector would return zero for the former and a strong signal for the latter, indicative of the weighting in the original field. In Fig. 2.3.2 we show examples of just such holograms as well as the light seen at the plane of the CCD detector. Our measurement scheme therefore comprises digital holograms as the match filters, and a monitor (CCD) of the on-axis signal in the Fourier plane of a lens. The measured intensities return the desired coefficients, ρ_n^2, for each mode. The modal phases $\Delta\phi_n$ are accessible analogously by creating a match filter, which depicts the superposition of the desired mode with a (previously chosen) reference mode as detailed in [2.6].

2.4. Results

We tested our approach by using a general case of coherent superposition of Laguerre-Gaussian modes of $LG_{0,4}$ and $LG_{0,-4}$, which had nearly equal weightings, as shown in Fig. 2.4.1(a). The influence of the scale of the beam on the modal decomposition results is demonstrated when the scale of the hologram functions used for the decomposition was changed from an initial optimal w_0 = 208 μm, which then yield non-adapted basis sets as shown by the results in Fig. 2.4.1(b) through to 2.4.1(d). When the relative scales are mismatched from an ideal w_0 to $0.75w_0$, $2w_0$ and $3w_0$, the results yield a concomitant increase in the number of modes in the non-adapted basis sets. We observe that only the radial modes with azimuthal orders $l = \pm 4$ responds, which then makes the non-adapted set to contain modes of $LG_{p,\pm 4}$ where $p \geq 0$. Simultaneously the power content of the $LG_{0,\pm 4}$ modes is shown to drop from an initial 99% to 48%, 13% and 2%. The power is shown to be dispersed among more modes of up to 30 for a basis scale of $3w_0$, compared to 2 for the adapted set. This is demonstrated more clearly by the results in Fig. 2.4.2(a) for a continuous change in the mismatch between the basis scale and the fundamental mode radius. The theoretical prediction for the change in $LG_{0,\pm 4}$ power as a result of the scale mismatch (solid curve) is shown to be in good agreement with the experimental data points. As noted, the modal power is dispersed amongst a large number of radial modes (Fig. 2.4.2(b)) and in general the greater the scale mismatch, the greater is the modal power dispersion.

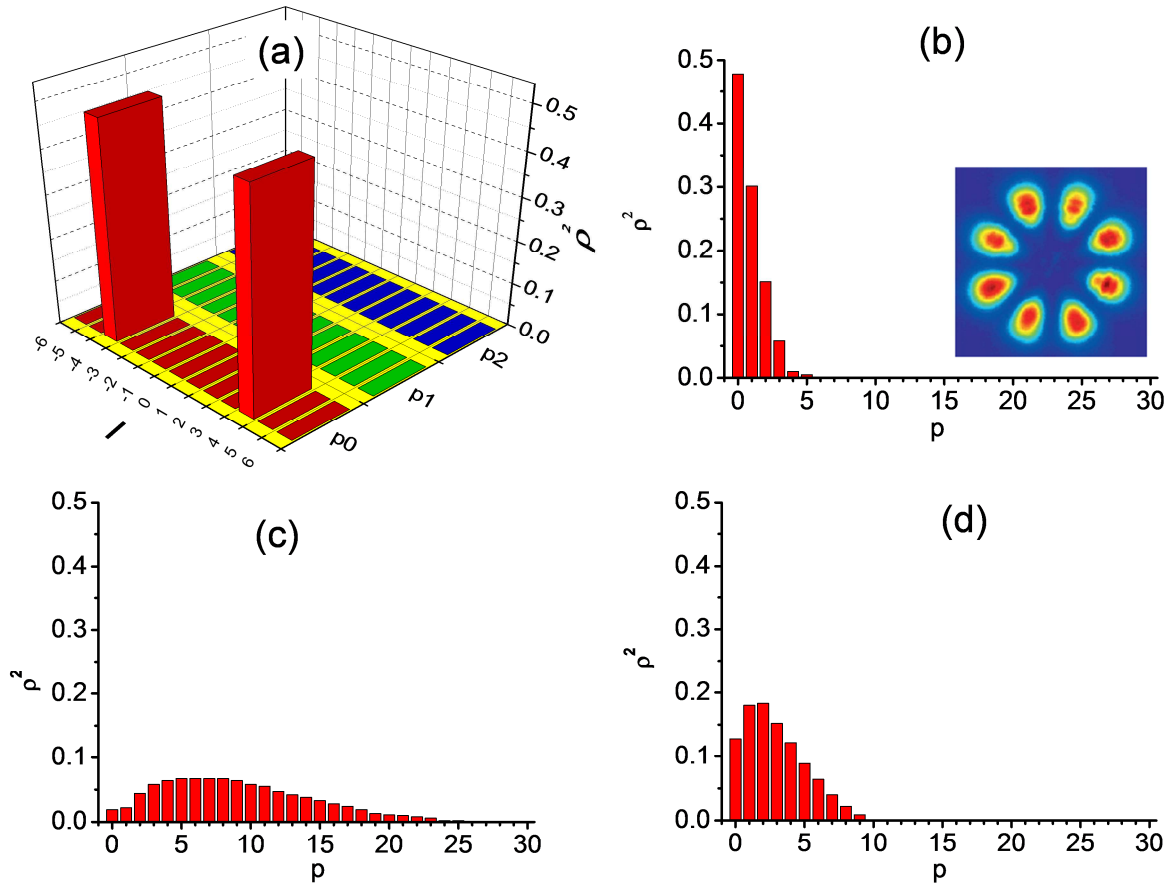

Fig. 2.4.1: Modal decomposition into adapted and non-adapted basis sets regarding scale. (a) Modal decomposition into $LG_{p,\pm4}$ modes of adapted basis scale w_0. (b) Decomposition into $LG_{p,\pm4}$ modes with scale $0.75w_0$, (c) $2w_0$, and (d) $3w_0$. Inset in (b) depicts the measured beam intensity.

The modal decompositions in Fig. 2.4.1 and 2.4.2 are all shown to be mathematically equivalent which emphasises the importance to decompose into an adapted set since this will have an order of magnitude decrease in the number of significant signals. Moreover, one could argue that this is the only set with an intuitively meaningful realization behind the measurement, namely, that the beam really does consist of a coherent superposition of two azimuthal modes and not a superposition of a large number of radial modes. From these results it is also clear that while the first step of our suggested procedure may be performed at any scale, a large deviation from the adapted set scale will result in a laborious measurement and low modal power levels, i.e., low signal to noise, if the modal decomposition method is used for this step too.

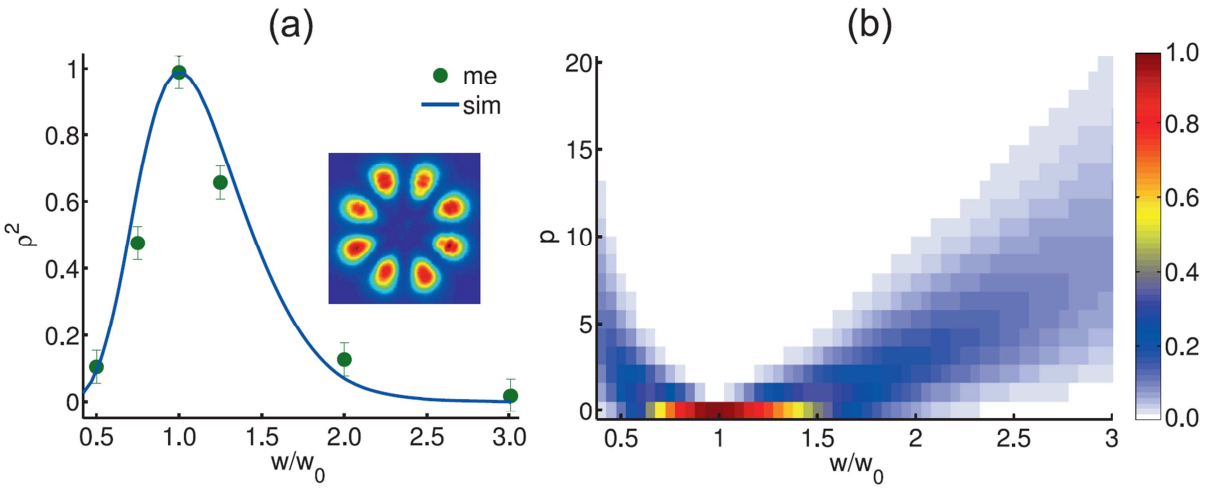

Fig. 2.4.2: Influence of basis set scale on mode spectrum. (a) Relative power ρ^2 of mode $LG_{0,\pm4}$, measured (me) and simulated (sim), as a function of normalised beam radius w/w_0. (b) Simulated power spectrum of $LG_{p,\pm4}$ modes (p = 0. . .20) as a function of normalised beam radius w/w_0. Inset in (a) depicts corresponding beam intensity.

In next part we apply our two-step approach of finding the adapted set by assuming that we do not know the scale parameter of the beam. For the first step we decompose our beam into a non-adapted basis set, and use the result to find the beam diameter and beam propagation factor [2.15]. The modal decomposition results are reconstructed (Reconstruction) and compared to the measured values (Measurement) using the ISO standard approach, and are summarised in Table 2.4.1. The results from both approaches show that they are of very good agreement.

Table 2.4.1: Diameter and M^2 of measured and reconstructed intensity.

	$2w$ (µm)	M^2	$\frac{2w}{\sqrt{M^2}}$ (µm)
Measurement	945.7	5.2	414.7
Reconstruction	913.6	5.0	408.6

This first step returns the "unknown" scale parameter with an average value of w_0 = 414 ± 2 µm which compares well with the theoretical value of 416 µm which is based on the ABCD matrix theory of the known resonator parameters. The second step is to execute the modal decomposition with the correct scale and the results are shown in Fig. 2.4.3. The measurement of amplitudes and phases of the correctly scaled modes shown in Fig. 2.4.3(a) and 2.4.3(b) enables the reconstruction of the optical field in the adapted basis. As expected, the modal decomposition returns the two original azimuthal modes. Using the modal decomposition results, the intensity of the field is reconstructed and

compared with the measured intensity of Fig. 2.4.3(c) and 2.4.3(d). Both are in good agreement, proving the decomposition to be correct.

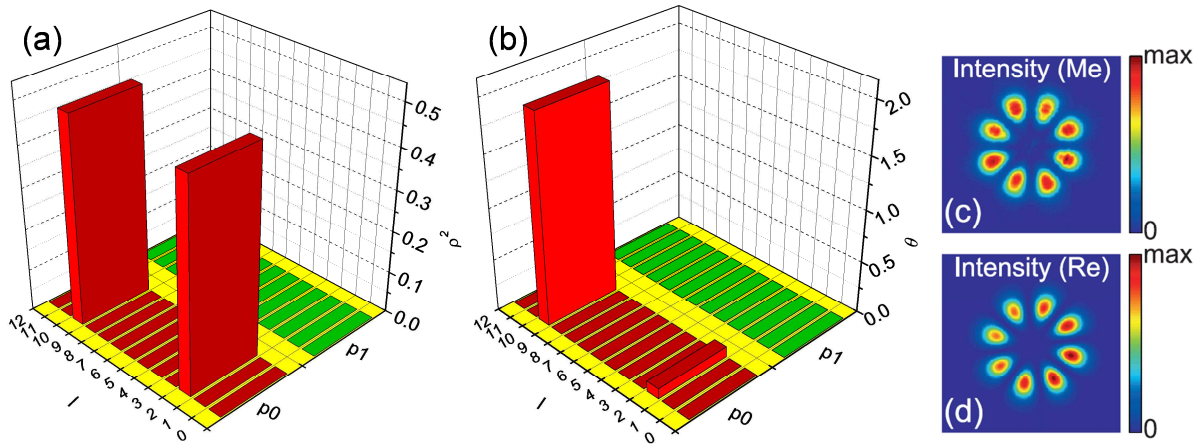

Fig. 2.4.3: Reconstruction of the beam by modal decomposition into $LG_{p,l}$ modes of previously determined scale. (a) Modal power spectrum (total power normalised to one). (b) Modal phases. (c) Measured intensity (Me). (d) Reconstructed intensity (Re).

The same two-step approach was applied to a beam consisting of only the radial order Laguerre Gaussian mode [2.18], $LG_{1,0}$ as shown in Fig. 2.4.4(a), and of a superposition of the $LG_{1,0}$ and $LG_{0,\pm4}$ modes, as depicted in Fig. 2.4.4(b).

It is important to note that if the first step of the procedure is executed with the recently mooted digital approach to M^2 measurements [18], then the entire technique can be implemented with a single spatial light modulator necessitating only a changing digital hologram. As holograms are easy to create and may be refreshed at high rates, the entire procedure can be made all-digital and effectively real-time.

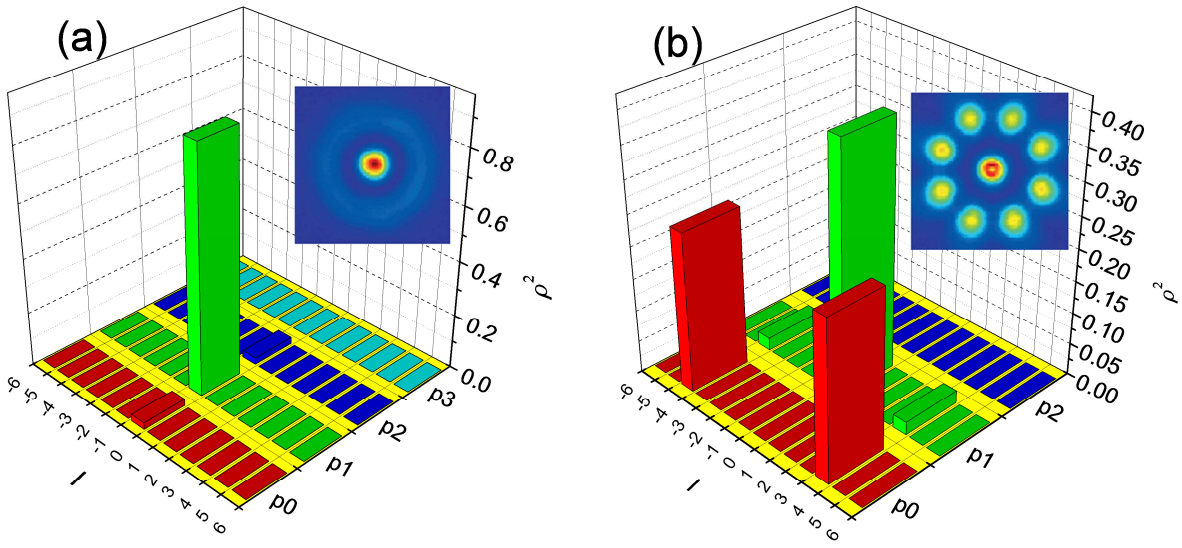

Fig. 2.4.4: Modal decomposition after determination of correct basis set scale of (a) a Laguerre-Gaussian $LG_{1,0}$ beam, and (b) of a superposition of an 8-petal beam and a $LG_{1,0}$ beam. Insets depict corresponding beam intensities.

2.5. Conclusions

In conclusion we have demonstrated a new approach for the modal decomposition of an arbitrary field that requires no a priori scale information on the basis functions. Our approach makes use of digital holograms written to a spatial light modulator, and exploits the relationship between the scale parameters within the basis and the beam propagation factor of the beam. We have demonstrated the approach on LG modes and have successfully reconstructed the modes and their sizes. This new approach may readily be extended to other bases too. The advance of our method will be of relevance to studies of resonator perturbations, e.g. thermal effects and aberrations, and in the study of multimode fibre lasers.

2.6. References

[2.1]. E. Tervonen, J. Turunen, and A. Friberg, “Transverse laser mode structure determination from spatial coherence measurements: Experimental results,” Appl. Phys. B. **49**, 409 (1989).

[2.2]. A. Cutolo, T. Isernia, I. Izzo, R. Pierri, and L. Zeni, “Transverse mode analysis of a laser beam by near-and far-field intensity measurements,” Appl. Opt. **34**, 7974 (1995).

[2.3]. M. Santarsiero, F. Gori, R. Borghi, and G. Guattari, “Evaluation of the modal structure of light beams composed of incoherent mixtures of hermite-gaussian modes,” Appl. Opt. **38**, 5272 (1999).

[2.4]. X. Xue, H. Wei, and A. G. Kirk, “Intensity-based modal decomposition of optical beams in terms of hermite–gaussian functions,” J. Opt. Soc. Am. A **17**, 1086 (2000).

[2.5]. D. Flamm, O. A. Schmidt, C. Schulze, J. Borchardt, T. Kaiser, S. Schr¨oter, and M. Duparr´e, “Measuring the spatial polarization distribution of multimode beams emerging from passive step-index large-mode-area fibers,” Opt. Lett. **35**, 3429 (2010).

[2.6]. T. Kaiser, D. Flamm, S. Schr¨oter, and M. Duparr´e, “Complete modal decomposition for optical fibers using CGH-based correlation filters,” Opt. Express **17**, 9347 (2009).

[2.7]. D. Flamm, D. Naidoo, C. Schulze, A. Forbes, and M. Duparr´e, “Mode analysis with a spatial light modulator as a correlation filter,” Opt. Lett. **37**, 2478 (2012).

[2.8]. O. A. Schmidt, C. Schulze, D. Flamm, R. Br¨uning, T. Kaiser, S. Schr¨oter, and M. Duparr´e, “Real-time determination of laser beam quality by modal decomposition,” Opt. Express **19**, 6741 (2011).

[2.9]. I. A. Litvin, A. Dudley, and A. Forbes, “Poynting vector and orbital angular momentum density of superpositions of bessel beams,” Opt. Express **19**, 16760 (2011).

[2.10]. A. Dudley, I. A. Litvin, and A. Forbes, “Quantitative measurement of the orbital angular momentum density of light,” Appl. Opt. **51**, 823 (2012).

[2.11]. C. Schulze, D. Naidoo, D. Flamm, O. A. Schmidt, A. Forbes, and M. Duparr´e, “Wavefront reconstruction by modal decomposition,” Opt. Express **20**, 19714 (2012).

[2.12]. I. A. Litvin, A. Dudley, F. S. Roux, and A. Forbes, “Azimuthal decomposition with digital holograms,” Opt. Express **20**, 10996 (2012).

[2.13]. A. Siegman, “How to (Maybe) Measure Laser Beam Quality,” in DPSS (Diode Pumped Solid State) Lasers: Applications and Issues (Optical Society of America, 1998), p. MQ1.

[2.14]. ISO, “ISO 11146-1:2005 Test methods for laser beam widths, divergence angles and beam propagation ratios Part 1: Stigmatic and simple astigmatic beams,” (2005).

[2.15]. D. Flamm, C. Schulze, R. Br¨uning, O. A. Schmidt, T. Kaiser, S. Schr¨oter, and M. Duparr´e, “Fast M^2 measurement for fiber beams based on modal analysis,” Appl. Opt. **51**, 987 (2012).

[2.16]. C. Schulze, D. Flamm, M. Duparr´e, and A. Forbes, “Beam-quality measurements using a spatial light modulator,” Opt. Lett. **37**, 4687 (2012).

[2.17]. A. Arrizon, “Complex modulation with a twisted-nematic liquid-crystal spatial light modulator: double-pixel approach,” Opt. Lett. **28**, 1359 (2003).

[2.18]. S. Ngcobo, K. Aït-Ameur, N. Passilly, A. Hasnaoui, A. Forbes, “Exciting higher-order radial Laguerre-Gaussian modes in a diode-pumped solid-state laser resonator,” Applied Optics **52** (10), 2093 (2013).

CHAPTER THREE

Exciting higher-order radial Laguerre–Gaussian modes in a diode-pumped solid-state laser resonator

3.1. Introduction

The operation of solid-state lasers in a multi-mode regime has been shown to be the simplest method of extracting most of the energy in the gain medium, which then allows these lasers to be used in a large number of applications since they can produce high power multi-mode laser beams. Applications such as ultrafast spectroscopy, LIDAR, laser material processing, laser ranging and in military applications [1.27] currently employ high-power solid-state lasers. Solid-state lasers which are mostly used in these applications are currently diode-pumped solid-state lasers while earlier applications used flash lamp-pumped solid-state lasers. The progress towards the use of diode-pumped solid-state lasers is due the advantages they offer compared to flash lamp pumped solid state lasers such as higher efficiency, better frequency stability, higher brightness than diode lasers themselves, and a more compact design due to flexible cooling geometries [1.24]. Most of the recent high-power solid-state lasers often use fiber coupled diode pumping schemes which create multimode oscillation within the laser cavity which in general is not desirable for most of the applications mentioned above. This is shown by the significant effort the scientific community is putting to create geometries to ensure fundamental Gaussian beam oscillations in laser cavities. There are a very large number of schemes which are also too diverse to actually summarize adequately but most of the schemes involve either matching the pump size to the Gaussian beam size in order to maximize modal overlap, or simply aperturing the cavity to allow only the Gaussian beam to oscillate as the fundamental mode [1.21–1.23].

Laser resonators that produce high-order Laguerre-Gaussian modes that have zero radial order and higher azimuthal orders have received a renewed interest in the scientific community since they were discovered to possess well defined orbital angular momentum along the optical axis for non-zero values of azimuthal order, l [1.29]. Laser systems that produce Laguerre-Gaussian modes that have high azimuthal order only have been experimentally demonstrated in a wide variety of laser resonators of many classes [1.8-1.19], while laser systems that purely emit Laguerre-Gaussian modes that have high radial order have received little attention of late [1.20], in fact predominately high

radial order Laguerre-Gaussian modes have only been produced in combination with Laguerre-Gaussian modes that have azimuthal orders [1.17–1.20]. Solid-state laser resonators that emit Laguerre-Gaussian modes with high radial order only have received little interest in the scientific community and this has been attributed to the necessity in many laser applications for high brightness laser beams, a parameter that encapsulates both the power in the mode (P) and the beam propagation factor of the mode, M^2, through:

$$B = \frac{\pi^2 P}{\lambda^2 M^4} \tag{3.1.1}$$

Since, in general, the power in the mode and its beam propagation factor increase in a concomitant manner, much attention has been placed on increasing the power in low-order modes. A different approach of increasing the brightness of the laser would be to consider a method of how to select a particular high-radial-order Laguerre-Gaussian mode for maximum power extraction and then consider outside the cavity approaches of improving the beam quality factor of such a higher-radial-order Laguerre-Gaussian mode. In an effort to attain high laser brightness at the output it is preferable to pump as much of the gain volume as possible to achieve maximum energy extraction. This in turn increases the mode order within the cavity and for the selection of a desired mode, methods such as pump-shaping [3.1], intra-cavity beam shaping [3.2–3.5], and even Talbot imaging of periodic obstacles [3.6] may be employed. The simplest intra-cavity method in selecting higher order modes and in particular, circular symmetric modes, is through the use of an “aperturing” element with circular symmetry. Usually one associates such a mode selecting element with higher losses than high transmission phase-only diffractive optical elements (DOEs), but this has recently been shown not to be true in general [3.7].

In this Chapter [2.18] we demonstrate and outline a simple method of intra-cavity generating pure high-radial-order Laguerre Gaussian modes in a controlled manner. The experimentally generated modes show high mode purity up to radial order 5 and we consider the mode volume, losses, and energy extraction of such modes. We demonstrate that such high radial order modes maybe an option in designing high brightness diode-pumped solid-state laser resonator.

3.2. Laguerre–Gaussian Modes

Laguerre–Gaussian, LG_{pl}, modes, where p is the radial order and l is the azimuthal order, are solutions to the wave equation in circular symmetric geometries, and are analogous to the Hermite–Gaussian modes in rectangular symmetry. We recall that the electric field of an LG_{pl} mode may be written (see Eq. 1.5.1) as:

$$u_{p,l}(r,\phi,z) = \sqrt{\frac{2p!}{\pi(|l|+p)!}}\frac{1}{w(z)}\left(\frac{\sqrt{2}\,r}{w(z)}\right)^{|l|} L_p^{|l|}\left(\frac{2\,r^2}{w^2(z)}\right) e^{\left(\frac{-r^2}{w^2(z)}-\frac{ikr^2}{2R(z)}\right)} e^{\left(-i(2p+l+1)\tan^{-1}\left(\frac{z}{z_R}\right)\right)} e^{(il\phi)} \quad (3.2.1)$$

where r and ϕ are the radial and azimuthal coordinates, respectively, and $L_p^{|l|}$ is the generalized Laguerre polynomial. Here the Gaussian beam parameters have their usual meaning, with z the propagation distance, z_R the Rayleigh range, and R_z and $w(z)$ are the radius of curvature and beam radius of the embedded Gaussian beam, respectively. In this section, we will be particularly interested in symmetrical Laguerre–Gauss modes of zero azimuthal order, which we will denote as LG_{p0}. The Laguerre polynomials $L_p(X)$ follow the expressions given in Table 1.

Table 3.2.1: Laguerre Polynomials.

p	$L_p(X)$
0	1
1	1 – X
2	$X^2/2 - 2X + 1$
3	$-X^3/6 + 3X^2/2 - 3X + 1$
4	$X^4/24 - 2X^3/3 + 3X^2 - 4X + 1$
5	$-X^5/120 + 5X^4/24 - 5X^3/3 + 5X^2 - 5X + 1$

Let us recall that a LG_{p0} beam is made up of a central lobe surrounded by p concentric rings of light and p concentric dark rings. It is important to note that the spot size $w(z)$ has a simple physical interpretation only for the fundamental mode LG_{00} which is Gaussian in shape. The higher-order Laguerre–Gauss LG_{p0} beams are characterized by intensity patterns that spread widely from the axis as the mode order p increases. This lateral spread associated with a LG_{p0} beam can be described by the width, W_p, based on the second moment radius:

$$W_p = w(p)\sqrt{2p+1} \quad (3.2.3)$$

Another quantity which summarizes the propagation properties of a LG_{p0} beam is its beam propagation factor, given by:

$$M_p^2 = 2p + 1 \tag{3.2.4}$$

The spreading of a LG_{p0} beam can be described by the far-field divergence angle θ_p which can be expressed as a function of the Gaussian beam divergence θ_0 :

$$\theta_p = \theta_0\sqrt{2p+1} \tag{3.2.5}$$

Another important property of LG_{p0} beams is that they are characterized by the same on-axis intensity independent of the mode order p. This differs from the usual scale law which states that beam spreading results in an on-axis intensity reduction. In the following, we focus our attention on forcing the fundamental mode TEM_{00} of a laser cavity to be LG_{p0} in shape. For that we impose the position of the p zeros of intensity by setting an absorbing mask having a geometry which follows closely the location of the Laguerre polynomial zeros given in Table 3.2.2.

Table 3.2.2: Roots of Laguerre Polynomials.

p	Values of Ratio $\frac{r_i}{w}$ for the Zeros of Intensity of LG_{p0} Mode				
1	0.707106				
2	0.541195	1.306562			
3	0.455946	1.071046	1.773407		
4	0.401589	0.934280	1.506090	2.167379	
5	0.363015	0.840041	1.340975	1.882260	2.51040

Before proceeding it is worthwhile to note the distinction between the family of symmetrical Laguerre–Gauss modes, denoted LG_{p0}, and the symmetrical eigenmodes, TEM_{p0}, of the cavity. In general when the cavity has apertures and amplitude masks the fundamental mode of the cavity is not the lowest order mode in the Laguerre–Gauss basis. Rather, the fundamental mode of the cavity, denoted TEM_{00}, is the mode having the lowest losses and consequently is the one appearing at the laser oscillation threshold [3.7]. This fundamental mode (TEM_{00}) can be engineered to be a LG_{p0} with $p > 0$ depending on the inserted intra-cavity mask, as will be shown later.

3.3. Concept and Experimental Setup

In our approach to producing LG_{p0} modes we consider a plano-concave solid-state laser resonator that is end-pumped with a multi-mode fibre coupled diode, and with an intra-cavity amplitude mask at one end. The amplitude mask consists of lithographically produced thin aluminium absorbing rings fabricated on a 700 μm thick borosilicate glass with a 93% transmission at 1064 nm wavelength. The mask consisted of a 5 × 4 grid of ring structures: each of the 5 columns corresponding to concentric rings for modes $p = 1 - 5$ (for a Gaussian width of $w_0 \sim 184$ μm), with each row corresponding to a ring width of $h =$ 10, 15, 20, and 25 μm. A schematic of the experimental setup is presented in Fig. 3.3.1. The gain medium, a Nd:YAG rod crystal (4 mm × 25 mm) had a 1.1% neodymium concentration and was antireflection coated for 808 nm to minimize pump reflections. The laser crystal was mounted inside a 19°C water-cooled copper block. The pump diode laser (Jenoptic, JOLD-75-CPXF-2P) had a maximum output power of 75W at an emission wavelength of 808 nm (at an operating temperature of 25°C). The pump diode laser output was coupled into a fibre with a core diameter of 400 μm and was fast-axis collimated and lens coupled to end-pump the Nd:YAG crystal by using a 25.4 and 150 mm focal length spherical lenses, respectively. A gain area with a diameter of 2 mm was then excited within the centre of the Nd:YAG rod crystal.

The plano-concave cavity comprises a plane mirror with a reflectivity of 98% and a curved mirror with a 300 mm radius of curvature and reflectivity of 99%. The resonator was formed in a z-shape (in order to avoid illuminating the mask with the residual pump light) by including two 45° mirrors within the cavity that were highly reflective for 1064 nm and highly transmissive for 808 nm. The resonator length was 260 mm and the Nd:YAG crystal centre was positioned 75 mm from the plane mirror. The aperture was placed as close as possible to the curved mirror while the mask was placed as close as possible to the flat mirror. Both the aperture and the mask were individually mounted on 3-axis translation stages for easy alignment.

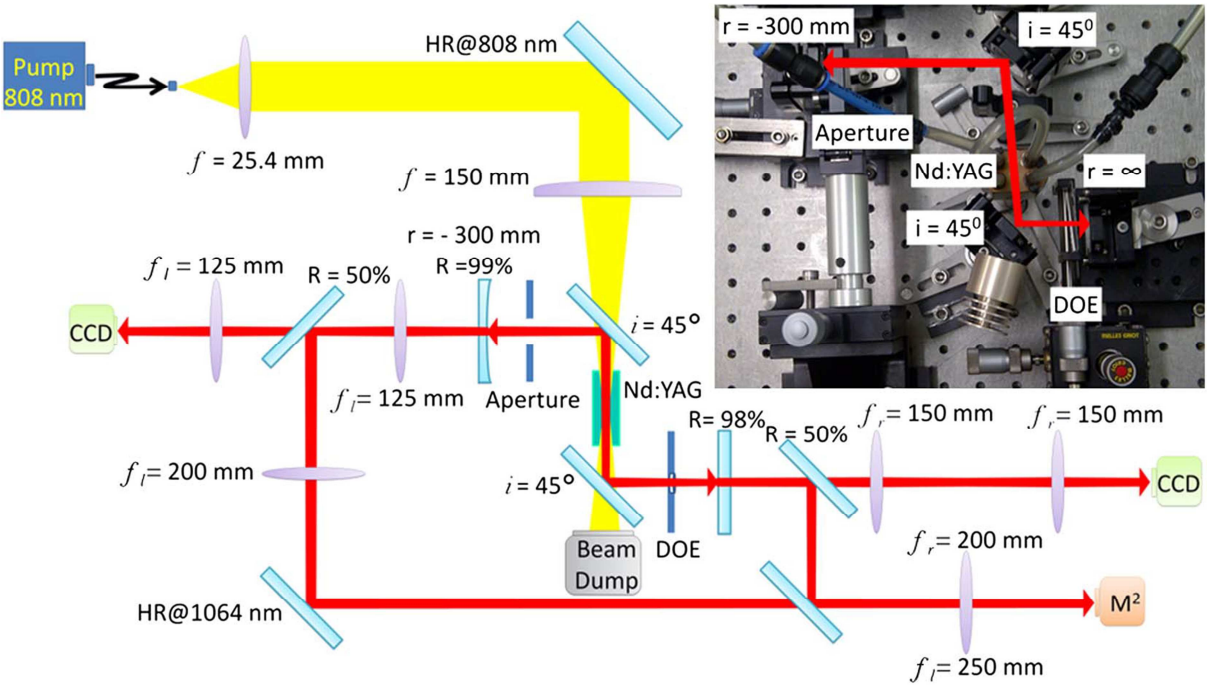

Fig. 3.3.1: Diode-pumped Nd:YAG laser resonator with internal mask (DOE). Resonator mirrors were configured such that the output beam could be observed from both ends with various beam diagnostic tools. Inset shows the actual setup in the laboratory.

The laser beam could be out-coupled from both ends of the resonator for measurement. The output through the mask (plane mirror) was measured with a near field CCD camera (Photon Inc. USBeamPro) by relay imaging the output coupler plane to the camera by a 1:1 telescope system of two 150 mm focal length spherical lenses. The beam quality factor M^2 from the flat mirror output was measured by directing and focusing the beam using two 50% transmissive flat mirrors and a 200 mm focal length spherical lens into the Photon ModeScan Meter. Simultaneously, the laser beam profile from the curved mirror output was 1:1 imaged using a telescope system of two 125 mm focal length spherical lenses and measured using a second CCD camera (Spiricon, LBA-USB). The beam quality factor M^2 from the curved mirror output was measured by directing and focusing the beam using three flat mirrors (one highly reflective and two 50% transmissive) and three focal length spherical lenses (125, 200, and 250 mm) into the Photon ModeScan Meter. The resulting fields could also be directed to a spatial light modulator (SLM) (Holoeye HEO 1080P) for executing a modal decomposition into the Laguerre–Gaussian basis [3.8, 3.9]. Measurement of the signal at the origin of the Fourier plane (at the focal plane of a lens after the SLM) returned the intensity of the coefficients of the modal expansion [3.9].

3.4. Numerical Study

We perform a numerical calculation of the fundamental mode of the resonator with the intra-cavity mask. The simulation is based on the expansion of the resonant field on the basis of the eigen-modes of the bare cavity (without any diffracting object). This method is not given here since it has been already described elsewhere for the case of a plano-concave cavity including an absorbing ring on the plane mirror [3.10]. The modelling given in [3.10] can be easily adapted to the case of a mask made up of concentric absorbing rings just by evaluating the overlapping integral (Eq. A10 of Ref. [3.10]) upon all the regions of transparency of the mask. An example of the mask for the $p = 4$ mode is shown in Fig. 3.4.1: the high-loss regions of the mask (four absorbing rings) coincide with the nulls in intensity of the mode, while the rest of the mask is transparent. The four absorbing rings lead to the $p = 4$ mode having the lowest overall loss (similarly for the other modes).

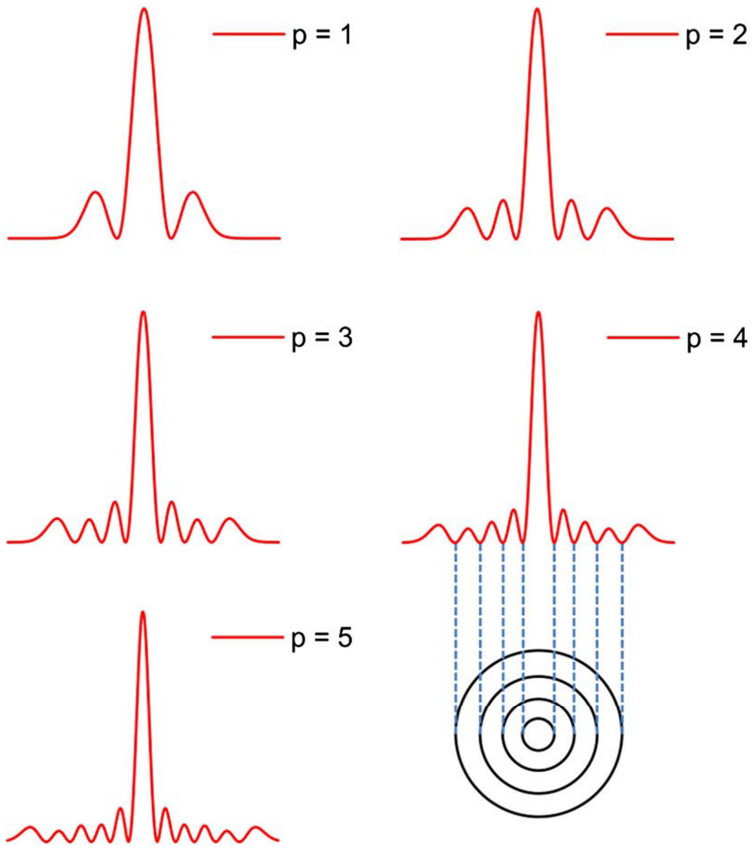

Fig. 3.4.1: Numerically simulated lowest-loss eigenmodes, shown as intensity cross-sections, for $p = 1 - 5$, when the appropriate mask with p rings is placed inside the cavity. Such a mask example is shown for the $p = 4$, with the high-loss rings of the mask coinciding with the intensity nulls of the $p = 4$ Laguerre–Gaussian mode.

The main quantities deduced from the numerical modelling which characterize the fundamental mode are the power losses per round trip LFM due to diffraction upon the absorbing p rings, the intensity profile of the lowest loss mode, and the beam propagation factor M^2 of the output beam. We find that the fundamental mode TEM_{00} of the cavity including an amplitude mask made up of p rings of radii given by Table 3.2.2 is a pure LG_{p0} mode, shown in Fig. 3.4.1: the mode purity was confirmed quantitatively through a numerical calculation of the M^2 of each mode, and found to be 3.02, 5.01, 7.01, 9.01, and 10.99 for $p = 1 - 5$, respectively, in agreement with the theoretical beam propagation factor of $M^2 = 2p + 1$. The variable parameter is the width of the absorbing rings: the simulations shown in Fig. 3.4.1 are for $h = 20$ μm, but similar results are found for the other width values. The variations of the fundamental mode losses LFM as a function of the mode order, with the width h of the rings as a parameter, are shown in Fig. 3.4.2.

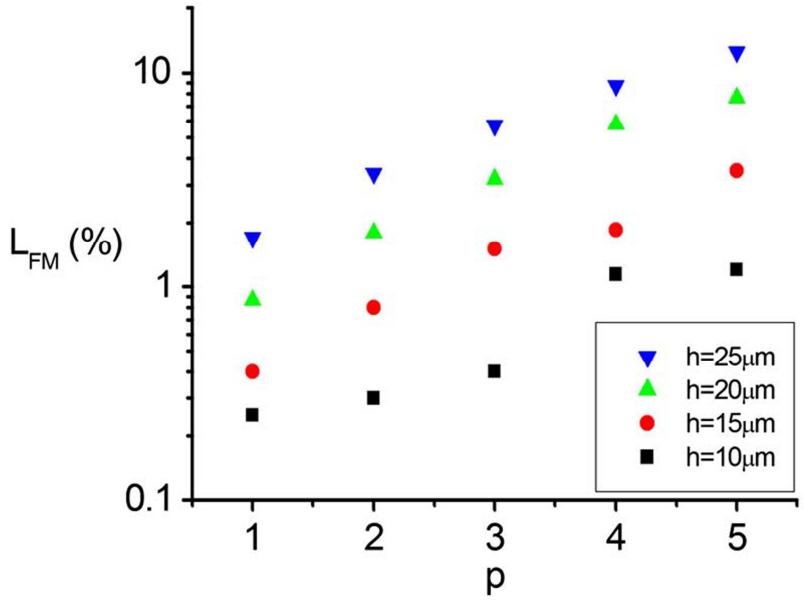

Fig. 3.4.2: Variations of the fundamental mode losses as a function of p the number of absorbing rings which is at the same time the order of the LG mode.

3.5. Experimental Results

3.5.1. Mode Purity

The results of the mode selection by the cavity and mask adjustments are summarized in Fig. 3.5.1. In this section we restrict our summaries to the DOE setting with $h = 20$ μm, and we consider the impact of changing this in Chapter 3.4. Since the LG_p modes are solutions to the Helmholtz equation,

we expect that their near and far field intensity profiles should be identical except for a scale factor. This is clearly evident in Fig. 3.5.1, suggesting (but not yet confirming) that indeed these are the desired single modes of orders 0–5.

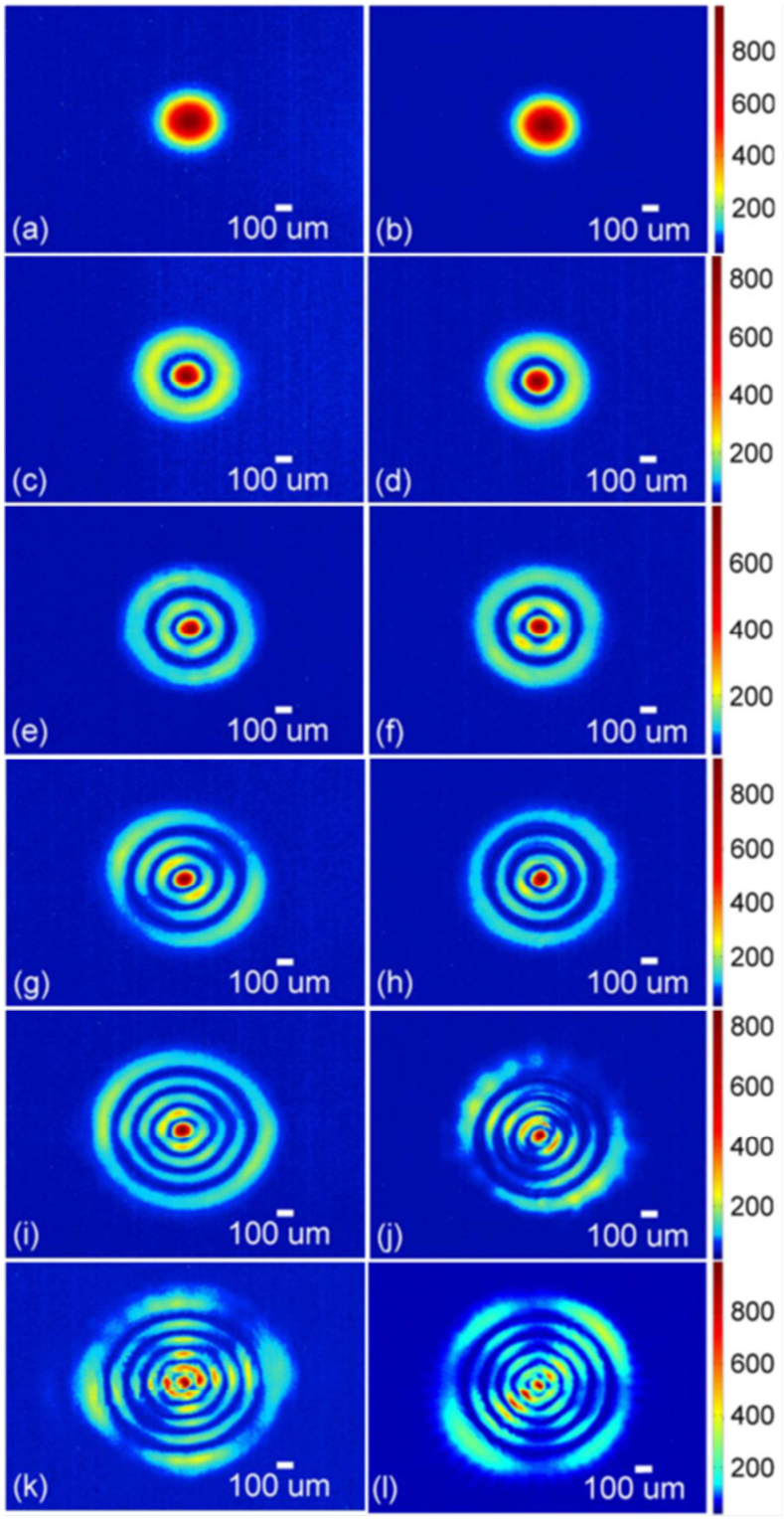

Fig. 3.5.1: Near-field (left column) and far-field (right column) intensity patterns for modes $p = 0 - 5$ (top to bottom rows).

What is evident from Fig. 3.5.1 is that the modes become less radially symmetric as the order increases, most likely due to aberrations inside the laser and the fine misalignment of the DOE. Since the resonator is stable and we are considering single modes, the mode sizes and beam propagation factors are known analytically and can be compared to experiment. The results are summarized in Fig. 3.5.2.

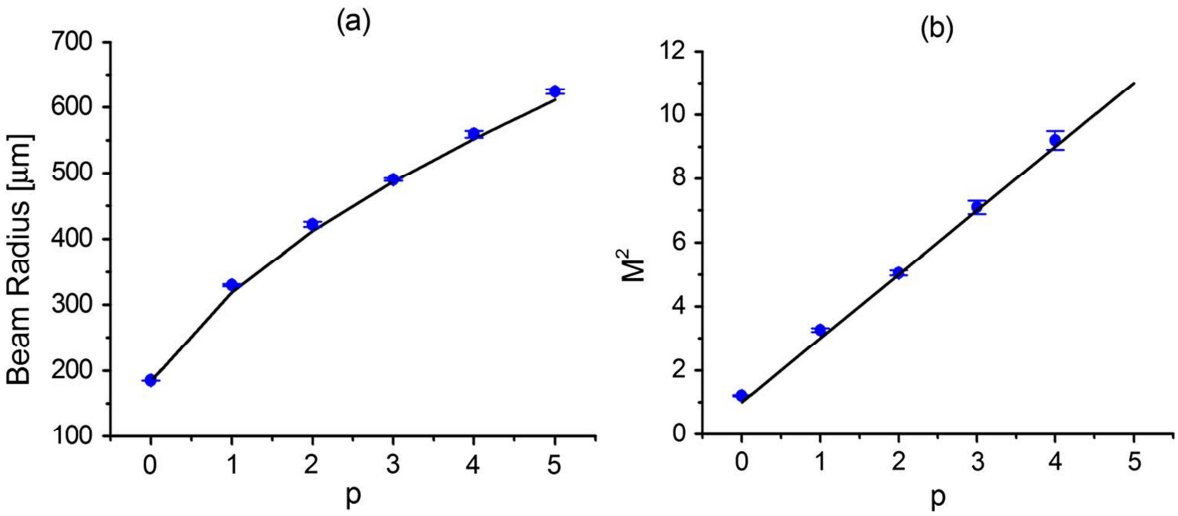

Fig. 3.5.2: (a) Beam width at the output coupler end as a function of mode order. (b) Beam propagation factor as a function of mode order. Solid line in both cases is the theoretical prediction from Eqs. (3) and (4), respectively.

Clearly the cavity is selecting the modes as desired, with the modal properties in good agreement with the theory. This suggests that the slight imperfections noted in the intensity patterns do not significantly affect the properties of the modes. Finally we execute a modal decomposition of the output fields to determine the modal purity of the higher-order modes. As shown in Fig. 3.5.3, the mode purity is >95% for modes $p = 1 - 4$, dropping to 85% for $p = 5$. The remaining modal power is in adjacent lower order modes.

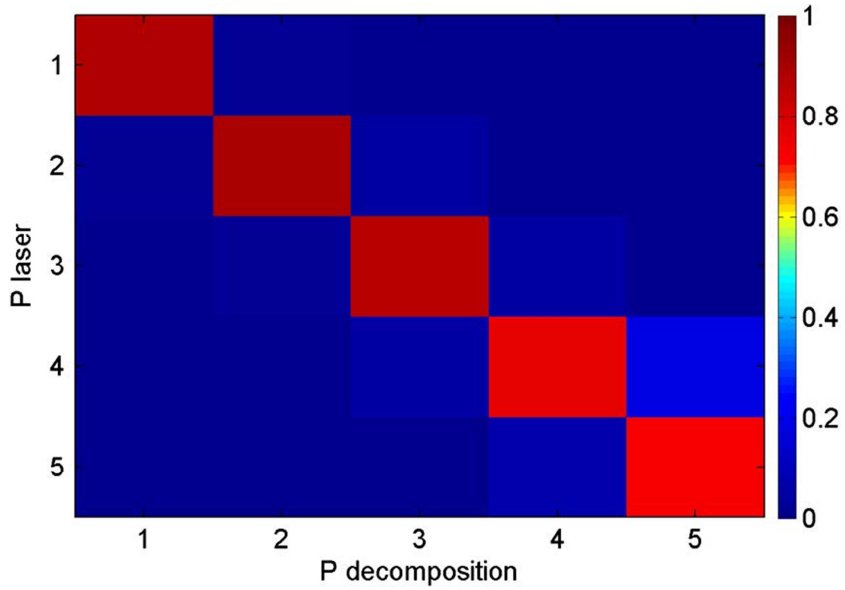

Fig. 3.5.3: Modal decomposition results for modes $p = 1 - 5$. Correlation between the desired mode (p_{laser}) and the measured mode ($p_{\text{decomposition}}$) is very high, degrading slightly at high values of p.

3.5.2. Mode Variance Due to Perturbations

We confirm, first, that thermal lensing and thermal aberrations are not significant in our system. The beam size and beam quality factor were monitored as a function of input pump power for each radial order, with some results for the $p = 0$, and $p = 5$ modes shown in Fig. 3.5.4. It is well known that thermal lensing increases approximately linearly with pump power and inversely with pump size. Within the range shown (corresponding to the range for all tests reported in this manuscript) we find that there is a flat response to our mode properties, as seen in Figs. 3.5.4(a) and 3.5.4(b), suggesting that thermal lensing is not a significant factor in our experiments. The main reason for that is the use of a large pump beam size in order to sustain the laser oscillation up to mode $p = 5$.

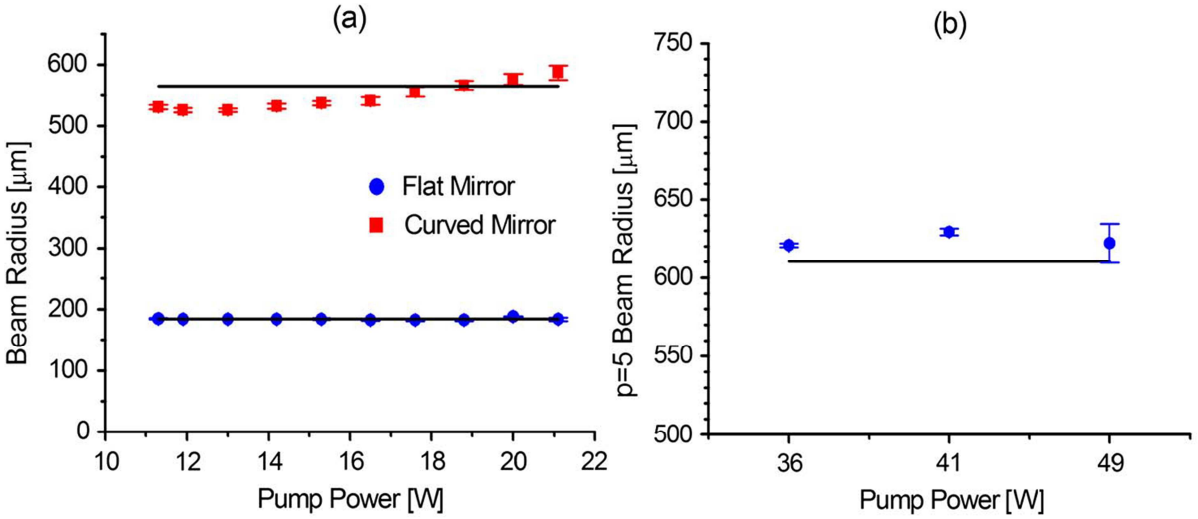

Fig. 3.5.4: (a) Change in beam radius as a function of a changing pump power, for the $p = 0$ mode, measured at both ends of the cavity, and the solid line is the theoretical solution. (b) Change in beam radius as a function of a changing pump power, for the $p = 5$ mode, measured at flat mirror and the solid line is the theoretical solution.

Next we changed the DOE position to select various ring widths, from h =10 to 25 μm, for each p value. The results for $p = 1$ are shown in Figs. 3.5.5(a) and 3.5.5(b). There is very little impact on the mode size and quality factor within this range of ring widths. This is expected from simulations of the transmission for these widths, where little influence is noted. We point out though that as the width increases, so the losses increase and eventually the mode purity would be adversely affected once the ring width exceeds the nominal width of the "zero" regions (see illustration in Fig. 3.4.1).

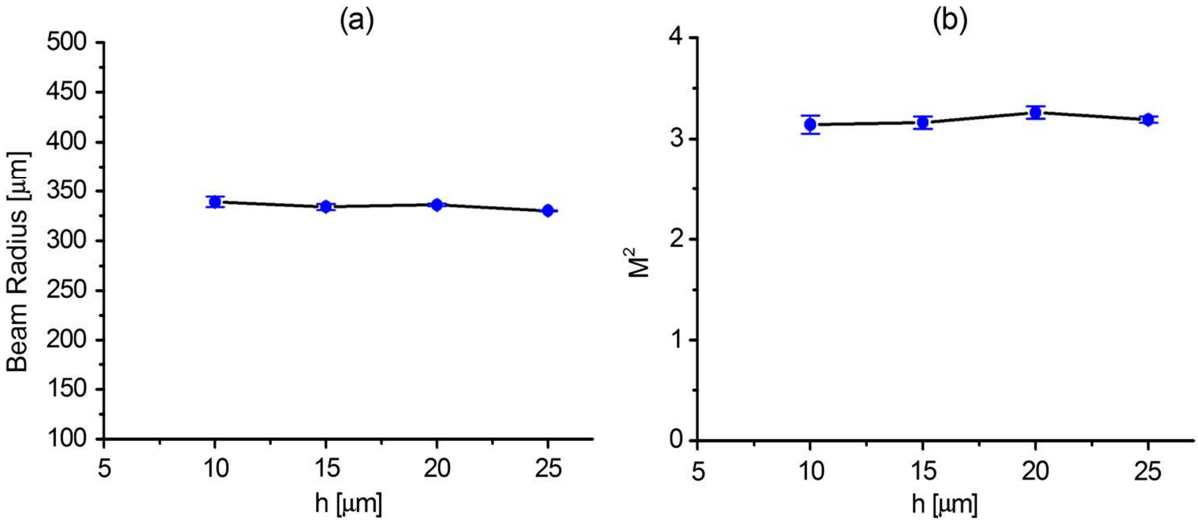

Fig. 3.5.5: (a) Beam radius and (b) beam quality factor changes for mode $p = 1$ when the ring thickness of the DOE is changed.

3.5.3. Mode Volume, Energy Extraction, and Loss

We recall that the output power from a laser is linearly proportional to the mode volume, V_p, where the volume of the pth radial mode is found from:

$$V_p = \int_0^{l_0} \pi W^2(z) dz = (2p+1)\pi w_0 l_0 \left(1 + \frac{l_0^2}{3z_r^2}\right)$$

$$V_p = M^2 V_0 \left(1 + \frac{l_0^2}{3z_R^2}\right) \tag{3.5.1}$$

where l_0 is the length of the gain medium and V_0 is the mode volume of the $p = 0$ (Gaussian) mode. In the limit that the length of the crystal is much smaller than the Rayleigh range of the beam, $l_0 \ll z_R$, then Eq. (3.5.1) simplifies to $V_p \approx M^2 V_0$.

From Eq. (3.5.1) it is clear that the mode volume is proportional to the M^2 factor associated with the mode. The output power is also inversely proportional to the round-trip losses. This suggests that the higher-order radial modes have an output power that may be expressed as:

$$\frac{P_p}{P_0} = (2p+1)\frac{\delta_0}{\delta_p} \tag{3.5.2}$$

where the subscripts p and 0 refer to the radial mode orders and the round trip losses are denoted by δ. Measurements of the threshold and slope efficiency of the generated modes are shown in Fig. 3.5.6.

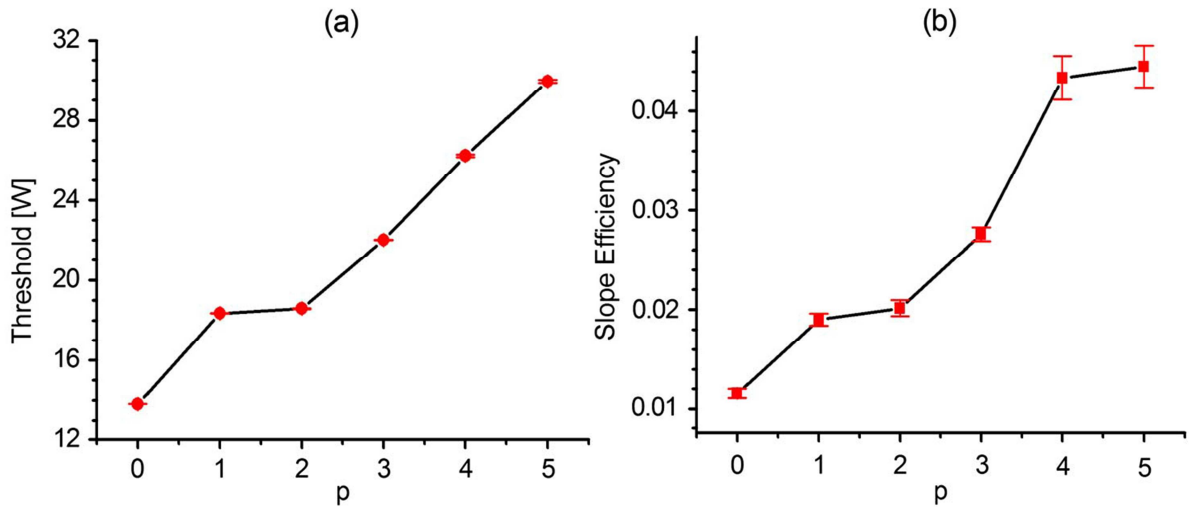

Fig. 3.5.6: (a) Threshold and (b) slope efficiency as a function of the mode order p. Both increase approximately linearly with mode index.

Equation (3.5.2) suggests that it is possible to have a larger power extraction from a higher-order mode if the losses increase at a slower rate than the mode volume. This is the case with our scheme for selecting the higher-order modes. Making the assumption that the ratio of the losses, δ_0/δ_p, can be approximated as the ratio of the threshold values [Fig. 3.5.7 (a)], we calculate the ratio of P_5/P_0 to be ~5, whereas the slope efficiencies have a measured ratio of ~4 [Fig. 3.5.7 (b)]. The extraction of power from the laser therefore has a critical point where the higher-order mode becomes more beneficial as compared to the lower order mode: although the losses increase with mode order, so does the mode volume and hence the gain. In the case of the radial LG_p modes, there is a point where the extra gain compensates for the extra loss. This scenario is illustrated for the $p = 0$, and $p = 5$ modes in Fig. 3.5.7: at a pump power of just greater than 35 W the power extracted from the $p = 5$ mode exceeds that of the $p = 0$ mode, despite its higher losses.

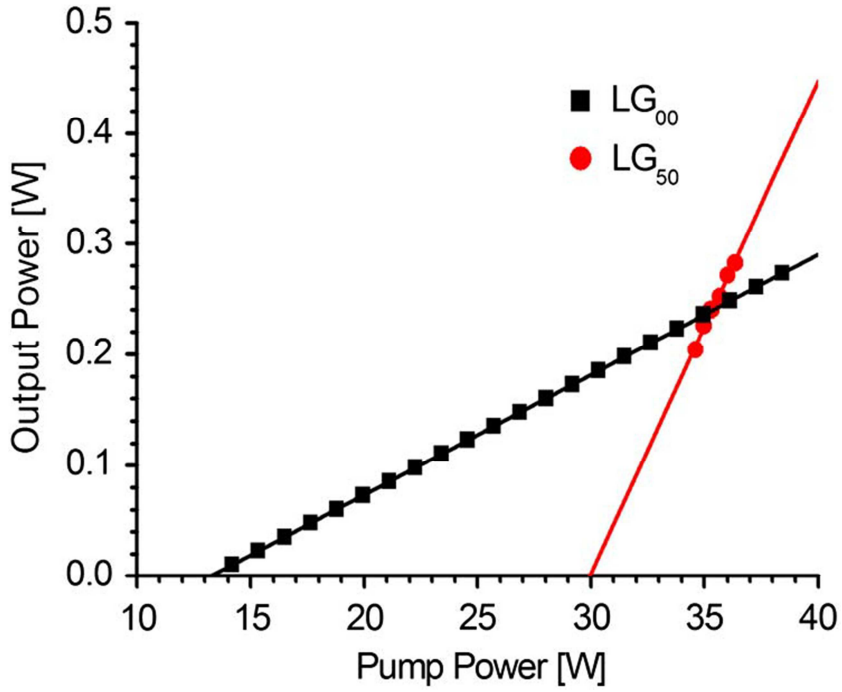

Fig. 3.5.7: Above a certain critical pump power, the higher-order mode extracts more power (compared to the $p = 0$ mode) due to its significantly increased mode volume, as shown here for the $p = 5$ mode.

3.6. Discussion

During the experimental work the laser cavity was optimised for the study of several modes under the same cavity conditions and in most occasions the laser was operated close to a threshold. The experimental laser design configuration was optimized for mode purity and not necessarily for power extraction. This is further shown in Fig. 3.3.1, the cavity was designed to have two output couplers

emitting laser light from both ends, each with a low transmission. For maximum power extraction of a given mode the construction of a laser resonator would require judicious choice of output coupler reflectivity, crystal length, doping concentration, and a very good mode-pump overlap. It is therefore clear that the overall power extraction efficiency of such an end-pumped solid-state laser could be improved to much higher values just by reconfiguring the laser resonator design, which indeed would be required if one were to construct a high-brightness laser. In this Chapter we are interested in the relative modal improvement of the Laguerre-Gaussian high-radial-order modes by comparing the ratios of the losses and the slope efficiencies, which follow Eq. (3.5.2). In this sense the slope efficiency has been improved by 400% for the $p = 5$ mode relative to the Gaussian mode. Finally, we point out that the quoted pump power represents the pump power as measured from the source and not the pump power absorbed by the crystal. The actual absorbed pump power was typically 50% of the quoted value.

The results in Chapter 3 demonstrate that with our simple controlled mode selection approach we can select a single higher-order Laguerre-Gaussian mode of very high purity (Fig. 3.5.3) and also ensure that it has a higher relative energy extraction (Fig. 3.5.7) from the laser cavity compared to a Gaussian mode. In order to increase the brightness of the single higher-order Laguerre-Gaussian mode, it would be necessary to improve the mode quality factor M^2 through a technique such as field mapping process, which would change the single higher-order Laguerre-Gaussian mode to a lowest order Gaussian mode. It is well known that any coherent field may readily be reshaped to any other coherent field, like the Laguerre-Gaussian mode of radial order $p = 5$ can be shaped to a lowest order Gaussian mode of $p = 0$ using known procedures, such as interferometric beam combining [30], geometrical transformations [3.12], complex amplitude modulation [3.13], or refractive or diffractive beam shaping [3.14]. These procedures may induce losses if complex amplitude modulation is used, but lossless procedures have been demonstrated also [3.14, 3.15] and in most cases with two optical elements, the first optical element is usually used to transform the intensity and the second to transform the phase. That the beam quality can be improved by such optical transformations has been demonstrated experimentally [3.11, 3.16], and is in fact evident from the reciprocity nature of light's propagation: for example, the ubiquitous Gaussian to flattop beam shapers in reverse would substantially improve the beam quality factor of the beam.

Our results therefore suggest a route to high brightness lasers through the selective excitation of higher-order laser modes and the subsequent conversion of these modes to lower M^2-valued beams.

3.7. Conclusions

We have demonstrated that it is possible to achieve selective excitation of higher-radial-order Laguerre–Gaussian modes inside a solid-state laser resonator with only an amplitude mask in a controlled manner. The generated high-radial-order Laguerre-Gaussian modes were shown to be of very high mode purity and that the method used to generate them was unaffected by the resonator perturbations. The significant importance of these results is the verification that indeed the power extraction from single high-order Laguerre Gaussian modes may exceed that of the lowest order Gaussian mode at a critical pump value of the resonator; which is determined by the relative cavity round-trip of the modes with reference to the Gaussian mode. For instance with a "lossy" amplitude mask that was utilised we achieved a 400% increase for the Laguerre-Gaussian mode of radial order $p = 5$ relative to the lowest Gaussian mode of order $p = 0$. These results suggest a route to high-brightness lasers through the selective excitation of higher-order laser modes above this critical input power, and the subsequent reshaping of the output field to a lower divergence mode.

3.8. References

[3.1]. D. Naidoo, T. Godin, M. Fromager, E. Cagniot, N. Passilly, A. Forbes, and K. Aït-Ameur, "Transverse mode selection in a monolithic microchip laser," Opt. Commun. 284, 5475 (2011).

[3.2]. P. A. Bélanger and C. Paré, "Optical resonators using graded phase mirrors," Opt. Lett. **16**, 1057 (1991).

[3.3]. C. Paré and P. A. Bélanger, "Custom laser resonators using graded-phase mirrors," IEEE J. Quantum Electron. **28**, 355 (1992).

[3.4]. I. A. Litvin and A. Forbes, "Gaussian mode selection with intracavity diffractive optics," Opt. Lett. **34**, 2991 (2009).

[3.5]. E. Cagniot, M. Fromager, T. Godin, N. Passilly, M. Brunel, and K. Aït-Ameur, "Variant of the method of Fox and Li dedicated to intracavity laser beam shaping," J. Opt. Soc. Am. A 28, 489 (2011).

[3.6]. K. M. Abramski, H. J. Baker, A. D. Colley, and D. R. Hall, "Single-mode selection using coherent imaging within a slab waveguide CO2 laser," Appl. Phys. Lett. **60**, 2469 (1992).

[3.7]. A. Hasnaoui, T. Godin, E. Cagniot, M. Fromager, A. Forbes, and K. Aït-Ameur, "Selection of a LG_{p0} –shaped fundamental mode in a laser cavity: phase versus amplitude masks," Opt. Commun. **285**, 5268 (2012).

[3.8]. D. Flamm, D. Naidoo, C. Schulze, A. Forbes, and M. Duparre, “Mode analysis with a spatial light modulator as a correlation filter,” Opt. Lett. **37**, 2478 (2012).

[3.9]. D. Nadioo, K. Aït-Ameur, M. Brunel, and A. Forbes, “Intracavity generation of superpositions of Laguerre-Gaussian beams,” Appl. Phys. B **106**, 683 (2012).

[3.10]. A. Hasnaoui and K. Aït-Ameur, “Properties of a laser cavity containing an absorbing ring,” Appl. Opt. **49**, 4034 (2010).

[3.11]. A. A. Ishaaya, G. Machavariani, N. Davidson, and A. A. Friesem, “Conversion of a high-order mode beam into a nearly Gaussian beam by use of a single interferometric element,” Opt. Lett. **28**, 504 (2003).

[3.12]O. Bryngdahl, “Geometrical transforms in optics,” J. Opt. Soc. Am. **64**, 1092 (1974).

[3.13]V. Arrizon, U. Ruiz, R. Carrada, and L. A. Gonzalez, “Pixelated phase computer holograms for the accurate encoding of scalar complex fields,” J. Opt. Soc. Am. A **24**, 3500 (2007).

[3.14]. F. M. Dickey and S. C. Holswade, Laser Beam Shaping: Theory and Techniques (Marcel Dekker, 2000).

[3.15]. F. M. Dickey and S. C. Holswade, “Lossless laser beam shaping,” J. Opt. Soc. Am. A **13**, 751 (1996).

[3.16]. R. Oron, N. Davidson, A. A. Friesem, and E. Hasman, “Continuous-phase elements can improve laser beam quality,” Opt. Lett. **25**, 939 (2000).

CHAPTER FOUR

A digital laser for the selection of on-demand laser modes

4.1. Introduction

The operation of a laser generally produces a multi-mode laser beam profile with its shape changing arbitrarily as the power of the laser is increased. A laser that generates such arbitrary dynamic beam shape profiles is generally not useful in many specialized applications that require specific beam shapes such as direct laser paint stripping or thin film ablation, precision laser drilling, fiber and free space communication, and many other applications. Laser beam-shaping techniques [3.14] to control the beam profile emitted by lasers have been developed over the years to allow for extra-cavity reshaping of the laser beam to any desired transverse profile using a variety of methods such as diffractive optical elements, free-form optics and more recently by digital holograms written to a spatial light modulator (SLM). Nonetheless intra-cavity beam shaping possesses some advantages over extra-cavity beam shaping such as laser system efficiency and compactness.

Intra-cavity beam shaping has been the subject of interest for a number of years [1.22, 4.1, 4.2], with various laser cavity design techniques [3.4, 4.3-4.7] being executed successfully such as using a phase only [4.8-4.11], amplitude-only [1.15, 3.9] and phase–amplitude combination [4.12] optical elements for spatial mode selection. All of the above techniques have been demonstrated to require specialised and customised optics; in some cases like the technique used by Bourderionnet. et al. [4.12] required additional external beam-shaping optics, a wavefront sensor and an optimization algorithm routine to iterate towards the desired phase profile. There also have been other efforts at achieving controlled dynamic intra-cavity beam shaping using deformable mirrors [4.13-4.18], but such mirrors have been shown to have a finite stroke, which has caused them to have limited number of phase profiles that they can perform, and that is why deformable mirrors have found a small number of applications in laser mode shaping. Deformable mirrors have rather been extensively applied in high-power applications such as correcting mode distortions due to thermal loads or in maximizing energy extraction and optimization of laser brightness [4.15-4.18]. Until now, there has been no technique that has been demonstrated that shows real-time on-demand selection of arbitrary laser modes.

In this Chapter [4.22] we succeed in overcoming the previously mentioned restriction by using intra-cavity digital holograms, which are applied to a phase-only reflective SLM, to construct a rewritable holographic mirror by replacing a standard laser cavity end-mirror to form a digital laser. This enables on-demand laser mode selection to occur with high resolution and with very broad dynamic range of phase values. This method of using intra-cavity digital holograms makes the task of intra-cavity beam shaping very easy since it reduces the time to test concepts and supposedly only creates the ability to generate appropriate grey-scale images. To put it differently, the creation of customised laser modes has been minimized to that of only creating appropriate digital hologram pictures of the mode of interest; and the techniques to create such pictures is very well established as shown by the wide variety of literature on shaping light using digital holograms. This approach is very simple compared to the others techniques and its advantage is that it only requires a commercially available SLM in an otherwise standard laser cavity. Furthermore, the digital laser allows all the recognised techniques of intra-cavity beam selection to be performed. We demonstrate that the digital laser can mimic a conventional stable cavity and verify on-demand mode selection by dynamically changing the mirror hologram to output a variety of laser modes in real-time. We accomplish this feat by ‘playing a video’ [4.22] inside a laser cavity, requiring a shift in our thinking of mode control in laser resonators.

4.2. Methods

4.2.1. Laser cavity and SLM.

Several SLMs were used in the testing of the digital laser, and finally a Hamamatsu (LCOS-SLM X110468E) series device was selected. Previous tests with other SLMs failed mainly because of the phase–amplitude coupling that becomes pronounced during intra-cavity operation. The gain medium was a 1% doped Nd:YAG crystal rod with dimension of 30 mm (length) by 4 mm (diameter). The crystal was end-pumped with a 75-W Jenoptik (JOLD 75 CPXF 2P W) multimode fibre-coupled laser diode operating at 808 nm. The OC (flat curvature) had a reflectivity of 60%, whereas the SLM had a measured reflectivity of 91% at the desired polarization (vertical) and 93% at the undesired polarization (horizontal). To force the cavity to lase on the vertical polarization, an intra-cavity Brewster plate was used. On this polarization, calibration tests on the SLM reveal typical efficiencies of ~86% into the first order and ~1% into the zeroth order. In the intra-cavity configuration, this large difference results in suppression of the zeroth order because of the significantly higher round trip losses, and thus the SLM could be operated at normal incidence and without a grating. The SLM efficiency had a standard deviation of ~0.4% across all grey levels, that is, minimal amplitude effects

during phase modulation. The nominal length of the cavity was ~390 mm but was determined to have an effective length of 373 mm to compensate for the small thermal lensing due to pump absorption in the crystal as well as the refractive index of the crystal. The effective length was used in all calculations for the mode sizes. The resonator output was 1:1 imaged onto a Spiricon CCD camera using a telescope of two identical mirrors for intensity measurements, and could also be directed to a second SLM for modal decomposition studies. For far-field tests, the first lens of the telescope was removed.

4.3. Results

4.3.1. Realizing a digital laser.

Our laser which is shown in Fig. 4.3.1.1, consists of a normal folded plano-concave resonator design with an Nd:YAG laser crystal as the gain medium for the system. The extra-ordinary part of the resonator is the utilisation of a phase-only reflective SLM as the end-mirror of the laser cavity. The main function of the SLM is to display computer-generated holograms which are programmed as pixelated grey-scale images also known as digital holograms. The SLM is programmed to allow for a full phase cycle of 0 to 2π which is portrayed graphically as grey-scale colours ranging from white to black in 256 levels encoded as 8-bit images. For an instance, a sharp linear increase in colour levels from white to black would represent a linear increase of the phase from 0 to 2π and this would normally represent a diffraction grating. The SLM virtually allows any desired phase values to be programmed as grey-scale digital hologram images. It is clear to observe that the colour change from the SLM can be seen to represent an equivalent depth change in a normal diffractive optical mirror and that it is where the advantage lies with SLM. It is rather simple and easier to make different colours in an image than to spend a lot of time refabricating depth changes in a diffractive optical element. Since the SLM is used as an end-mirror and also to display a digital hologram to intra-cavity change the phase of the reflected light inside the resonator, it will be referred to as a digitally addressed holographic mirror and in short as a holographic mirror. The key properties required of the SLM for this application have been shown to be high resolution, high efficiency, high reflectivity at the appropriately desired polarization, small phase–amplitude crosstalk, reasonable damage threshold and a large phase shift at the chosen laser wavelength.

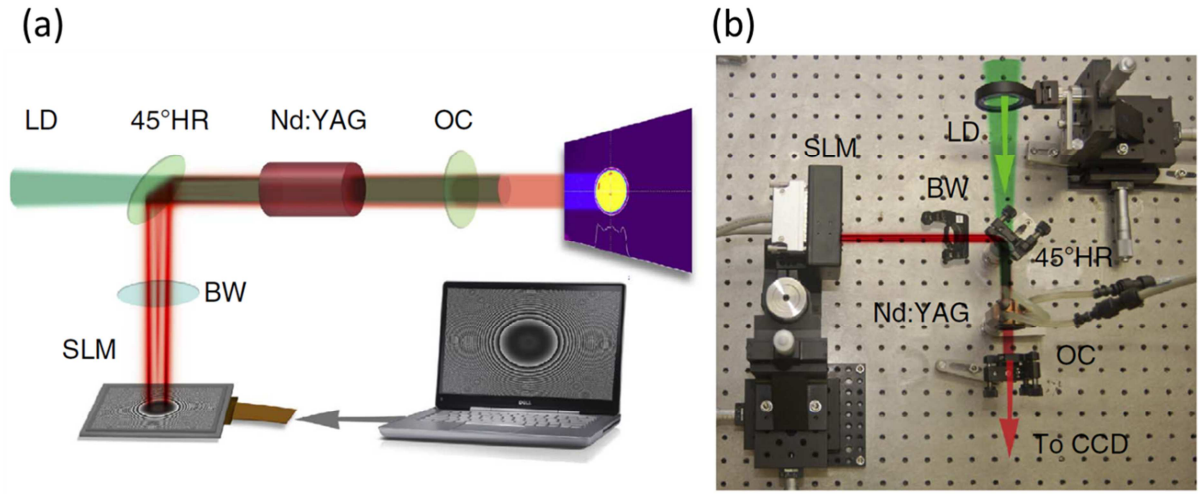

Fig. 4.3.1.1: Concept and experimental realization of the digital laser. (a) Schematic of the digital laser concept showing the SLM, Brewster window (BW), high reflectivity (HR) mirror at an angle of 45^0, Nd:YAG gain medium pumped by an external laser diode (LD) source and the output coupler (OC). (b) Photograph of the experimental set-up.

The digital laser shown in Fig. 4.3.1.1 was optically pumped by a high-power 808 nm laser diode that was fibre coupled into the cavity through a folding mirror that was coated for high transmission at the diode wavelength and high reflectance at the lasing wavelength of 1064 nm. The resonator was designed to form an L-shaped cavity using this folding mirror so that the high-power diode beam will not be absorbed by the SLM and thus avoiding damage. Another important feature of the cavity was the inclusion of an intra-cavity Brewster window that was used to force the laser to oscillate in the desired polarization for the SLM which in our case was vertical. The output coupler (OC) was used to emit the laser light out of the laser resonator.

In an experiment to prove the principle of our approach of dynamic intra-cavity beam shaping using an SLM, we programmed the holographic mirror to imitate a conventional concave end-mirror with a radius of curvature, R, which was chosen to ensure the resonator formed a stable cavity as shown in Fig. 4.3.1.2 (a). The SLM will then be programmed to produce a holographic image that will represent a lens with a focal length $f = R$, so that the hologram mimics the curvature of the end-mirror. The minimum beam radius which is the waist size on the flat output coupler of the Gaussian beam that oscillates in such a resonator can be described theoretical as [1.22]:

$$w_0^2 = \left(\frac{\lambda}{\pi}\right)[L(R-L)]^{\frac{1}{2}} \qquad (4.3.1.1)$$

where L is the effective length of the resonator and λ is the laser wavelength. Before the digital laser was tested, two physical concave mirrors were inserted as an end-mirror at separate occasions in the same experimental set-up in place of the SLM, and the Gaussian beam size was recorded at the output coupler. The experimental results for the two cases of using two physical end-mirror with, R = 400 and 500 mm, are shown in Fig. 4.3.1.2 (b) and plotted in Fig. 4.3.1.2 (c) together with the theoretical solid curve follow Eq. (4.3.1.1). An equivalent test of radius of curvature scenarios was programmed digitally using the SLM and are shown alongside the physical mirror measurements in Fig. 4.3.1.2 (b). From a mode selection perspective, the laser performs identically in the two configurations. Another observed scenario was that as the digital hologram's programmed radius of curvature was changed as shown in Fig. 4.3.1.2 (c), the measured Gaussian beam radius size on the flat output coupler changed in accordance with Eq. (4.3.1.1). This proves that the digital laser behaves as a standard stable laser cavity and it is also clear from the results that the SLM mimics the stable cavity with high fidelity. In addition to confirming the desired behaviour of the digital laser, this experiment also brings to the fore another practical advantage over using physical mirrors. It is a commonplace to possess a limited and discrete selection of physical mirrors, while with the digital approach virtually any mirror curvature can be created, on demand, by simply changing the grey-scale image representing the digital hologram, and it is limited only by the resolution of the SLM that will be used in the resonator.

The high loss properties of the SLM resulted to the laser resonator having a high lasing threshold as demonstrated in Fig. 4.3.1.2 (d). The resonator losses are due to the overall diffraction efficiency and fill factor of the SLM. These two loss effects can contribute to the SLM having a reduced reflectivity of between 15- 20 %.

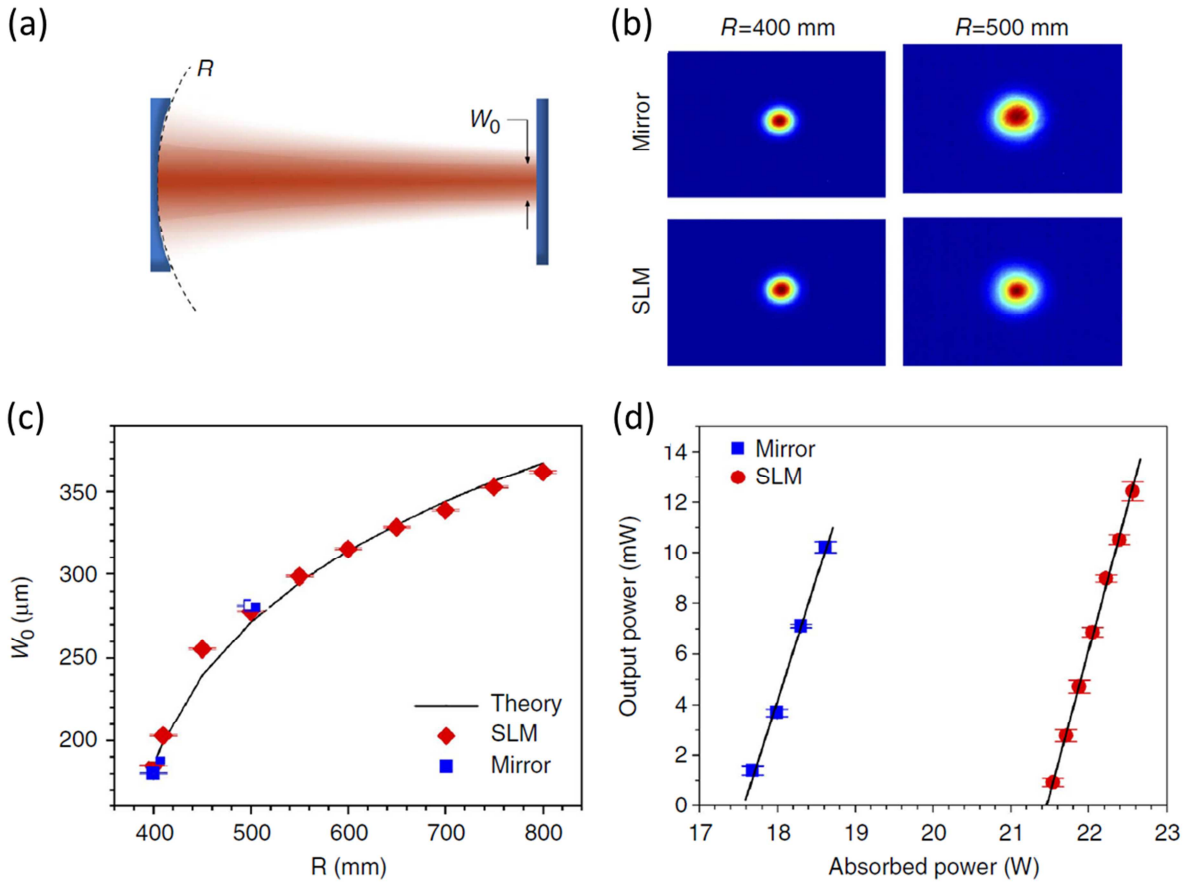

Fig. 4.3.1.2: Comparison of the digital laser to an equivalent plano-concave laser. (a) Schematic of the stable plano-concave resonator with a waist plane at the flat OC. (b) Measured intensity profiles for two curvature cases (R = 400 and 500 mm), comparing the digital laser output (SLM) with that of physical mirrors (Mirror). (c) The change in measured beam size with digitally imposed curvature matches the theoretical curve. (d) The threshold of the digital laser is higher than that of the conventional laser owing to the additional losses from the SLM shown here for the R = 400 mm case. The black lines are fits to the data and error bars are s.d.

4.3.2. On-demand laser modes.

In the following demonstration we used the digital laser to select and produce the well-known Hermit-Gaussian, Laguerre-Gaussian, super-Gaussian which is a flat-top and Airy beams. The digital laser can either be programmed to implement amplitude-only, phase-only or amplitude and phase modulation by simply changing the digital hologram grey-scale image that is displayed on the SLM screen. The SLM that is used in this experiment is able to implement phase-only changes on the field while a large number of the desired holograms require both the amplitude and phase changes on the field. We achieve this by making use of the well-known method of complex amplitude modulation [3.13, 4.19, 4.20], because it is easy and suitable to be implemented on the SLM. There are several

means by which to implement this (see Arrizon et al. [3.13, 4.20] and references therein), and for the benefit of the reader we briefly outline one approach used in the creation of our modes. Consider for example a desired field $u(x,y) = u_0 exp(i\phi)$, with u_0 the real amplitude and ϕ the phase of the desired beam. To encode the amplitude term, we introduce high spatial frequency modulation in the form of a checkerboard pattern with alternating phases between two values. The two phases are chosen so that their average value is equal to the desired complex value. For example, if the two phase values are given by $A = exp(i\phi + i\alpha)$ and $B = exp(i\phi - i\alpha)$, then the desired amplitude u_0 may be expressed as $u_0 = \cos\alpha$. This checkerboard may be varied spatially to create arbitrary amplitude modulation as a function of position. A graphical interpretation of the process is shown in Fig. 4.3.2.1 (a), where the modulation between two phase-only values (A and B) gives an average return of C, which is no longer on the unit circle in the complex plane, that is, amplitude modulation of the input field. The checkerboard corresponding to this is shown in Fig. 4.3.2.1 (b). This can be understood from basic diffraction theory: some of the incoming light is diffracted by the checkerboard grating into higher diffraction orders, so that the resulting light in the desired order is now less than before. In this sense, the desired light has been amplitude modulated, although the pattern on the SLM is phase-only.

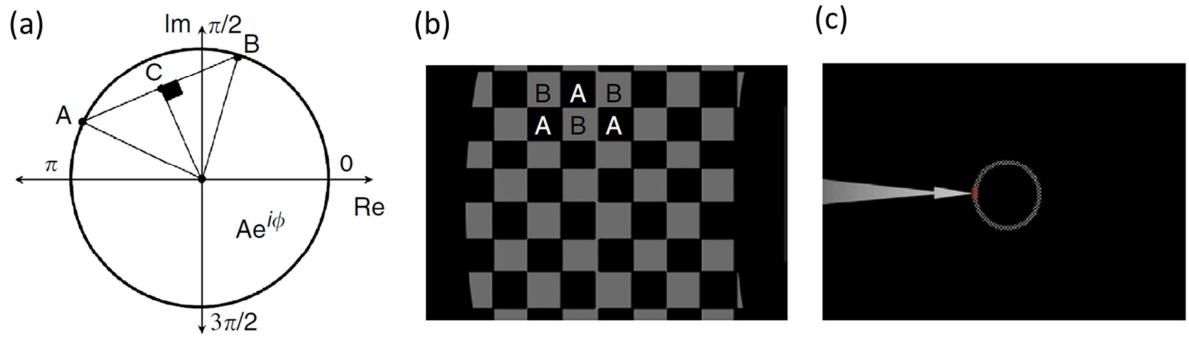

Fig. 4.3.2.1: Complex amplitude modulation concept. (a) Schematic of the complex plane showing two phase-only values, A and B, lies on the unit circle (unit amplitude). The average of these is vector C, representing amplitude modulation as it is not on the unit circle. (b) Example of a checkerboard pattern of the two phase values A and B. (c) Zoomed out image of b showing the complete annular ring created with this checkerboard pattern to result in zero transmission in the annular ring.

Thus, although our SLM is calibrated for a phase-only response from 0 which is represented as a black colour image all the way to 2π which is represented as white colour, appropriate holograms can result in amplitude variations from 0 to 1. An example of a high-loss annular ring is shown in Fig. 4.3.2.1 (c), with the zoomed-in checkerboard shown in Fig. 4.3.2.1 (b).

The selection of the Hermite-Gaussian and Laguerre-Gaussian modes shown in Fig. 4.3.2.2 exploited the use of complex amplitude modulation method to implement an amplitude modulation on the phase-only SLM [3.13, 4.19, 4.20]. This means the SLM can be used to create customized apertures, for example, just like the fine wires or loss-lines used in the past for Hermite-Gaussian mode selection [1.22, 4.1]. The digital hologram for the creation of the radial order, $p = 1$, Laguerre-Gaussian beam with zero azimuthal order, $l = 0$, comprised of a high-loss annular aperture together with a phase-only radius of curvature. In this case, the checkerboard consisted of the two phase values, 0 and π, for a resultant of zero amplitude inside an annular ring. This low-loss ring was positioned at the zero of the first radial Laguerre-Gaussian function to select the pure LG_{10} mode shown in Fig. 4.3.2.2. The radius of curvature was used to select and control the mode size, following Eq. (4.3.1.1). Many techniques exist for the design of intra-cavity diffractive optics [3.4, 4.3–4.7] for particular mode selection, all of which may readily be applied to the digital laser. We illustrate this in Fig. 4.3.2.2 where an Airy beam [4.21] and flat-top beam [4.5] are created by phase-only digital holograms.

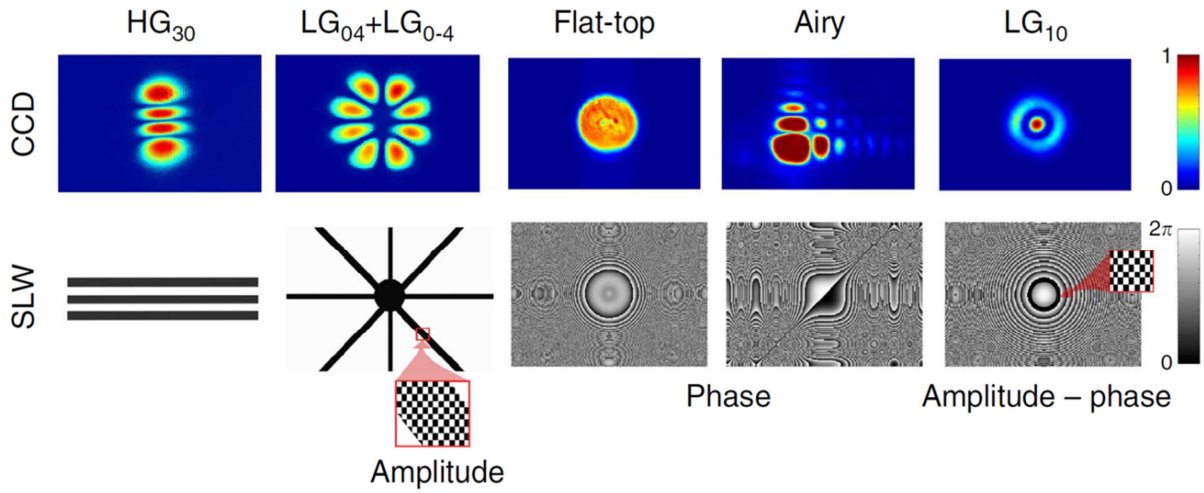

Fig. 4.3.2.2: Customized spatial modes by amplitude and phase modulation. By complex amplitude modulation, a customized set of high-loss regions create a Hermite–Gaussian beam ($n = 3, m = 0$) and a superposition of Laguerre–Gaussian beams ($p = 0, l = \pm 4$) as the laser output. By phase-only modulation, a flat-top beam and Airy beam are created as the stable modes of the cavity. Combining amplitude and phase effects allows for the selection of a Laguerre–Gaussian beam ($p = 1, l = 0$) of a chosen size.

Finally, we observed that switching from one mode to another required nothing more than changing the digital holographic grey-scale image that is displayed on the SLM which resulted in no realignment and also no additional optical elements being required. Traditionally, to generate the list of modes shown in Fig. 4.3.2.2 would have required several laser resonator set-ups with each resonator requiring customised and expensive optical elements. We exploit the versatility of the

digital laser by operating the laser in ‘video’ mode which allowed the fundamental mode that oscillates in the resonator to be changed in real-time by dynamically changing the digital hologram at an equivalent video refresh rate time. The movie laser video is shown in [4.22] and it is the first time this has ever been done in a laser and it represents a shift in the thinking about laser resonators.

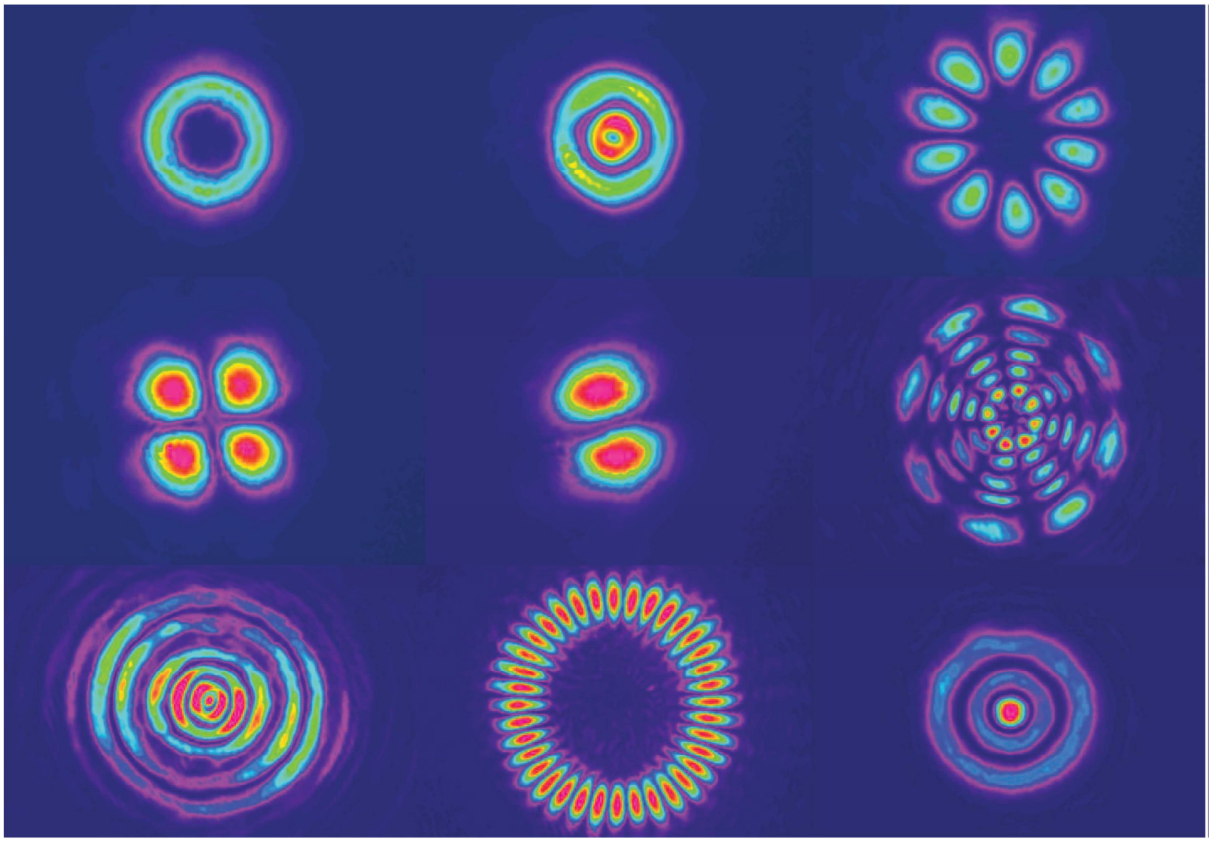

Fig. 4.3.2.3: Higher-order Laguerre–Gaussian modes. An example range of modes created with the digital laser.

To illustrate this technique’s applicability for intra-cavity mode control with the digital laser, we consider the generation of high-order modes and their super-positions in the laser cavity using complex amplitude modulation. In Fig. 4.3.2.3, we illustrate higher-order modes from the Laguerre–Gaussian basis, and in Fig. 3.3.2.4 we show a very high superposition state of the Laguerre–Gaussian modes with azimuthal indices of $l = +25$ and -25, creating a petal-like structure with 50 lobes. This is the highest pure azimuthal combination created in a laser that we are aware of. It is clear from these examples that a myriad of modes may be created within the laser cavity using our approach.

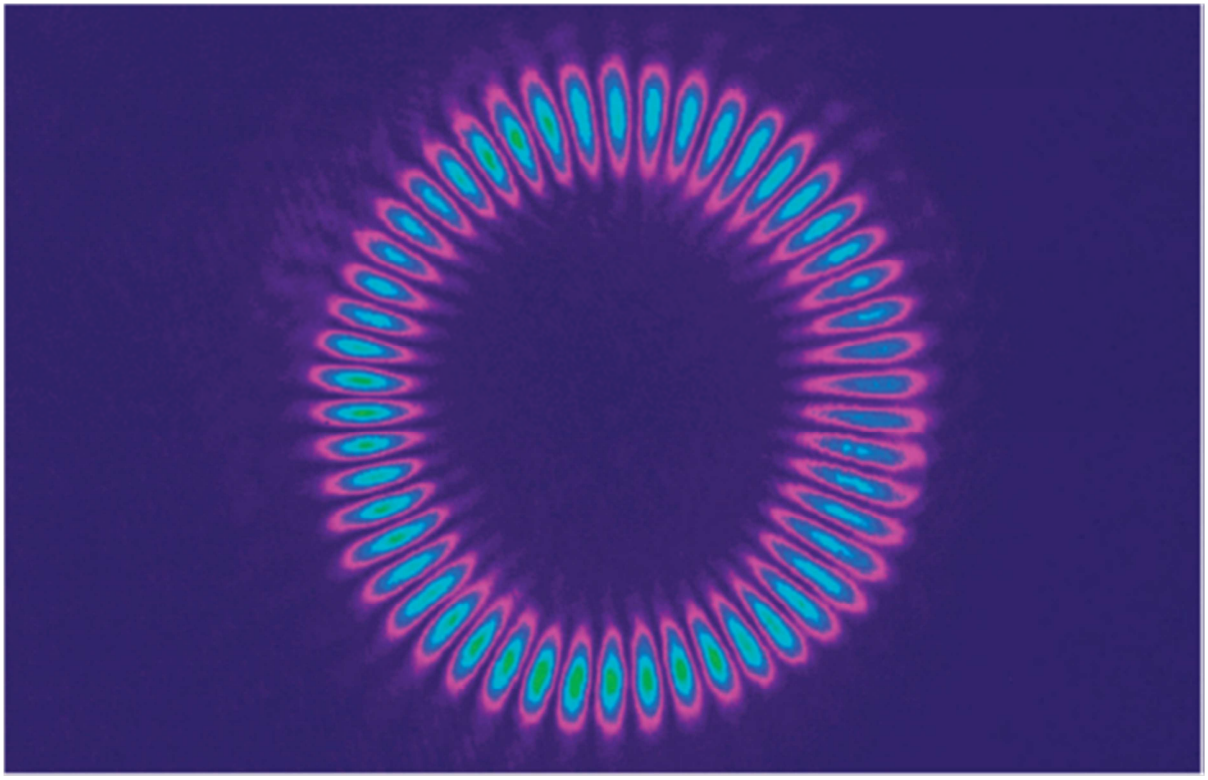

Fig. 4.3.2.4: A super-position of two high-order azimuthal modes. Two Laguerre–Gaussian modes of opposite but equal azimuthal index, and of azimuthal order $|l| = 25$, are combined coherently in the digital laser to produce this high-order superposition.

4.4. Discussion

All the generated laser beam shapes shown here were possible because the holograms fell well within the resolution of the SLM. At 800×600 pixels with a 20 µm pitch, the resolution is significantly higher than that of an adaptive mirror but substantially lower than that of a typical diffractive optical element. As the number of pixels decreases for each phase ramp of $0-2\pi$, so does the diffraction efficiency, as well as the functionality of the hologram, since for an example the resulting beam profile is degraded by the Moire´ patterns. Nevertheless, for a wide range of typical generated beam shapes, the standard SLM is more than sufficient to be used and moreover the current manufactures can produce SLM with much higher resolutions lately.

We have observed from our results that two conditions will have to be simultaneously satisfied for the digital laser to function properly. The gain of the laser must be sufficiently high to overcome the losses and at the same time the intra-cavity circulating intensity must not exceed the damage threshold of the SLM. We managed this by virtue of using a high-power diode pump source and an L-shaped

cavity design, but there are several other valid approaches (for example, increasing the doping concentration of the crystal). When these conditions are balanced, the digital laser will function as designed.

We also outline that all of the beam shaping techniques we used in designing the holograms for mode selection were standard and well known, that is, no new tools will be required to implement the digital laser approach. We have emphasised this point by creating modes traditionally generated by phase-only diffractive optical elements like the Airy beam, amplitude-only filters like the Hermite–Gaussian beams and the combinations of the two methods to produce the high-order Laguerre–Gaussian beams. What is very important about all the modes that we have shown here is that they required only a change to a picture to generate them and no new optics and no additional alignment of the laser cavity was needed. It is the simplicity of our approach that makes this digital laser so powerful. In that it offers a direct and easy means to control modes inside the resonator with suitable standard laser beam shaping tools and without any special optics being needed, just only a commercial SLM, which we can assume many researchers are familiar with and have access to. This makes our approach accessible to all.

4.5. Conclusions

In conclusion, we have demonstrated a novel digital laser that allows arbitrary intra-cavity laser beam shaping to be executed on-demand and also on an SLM refresh rate. This is substantially different from other intra-cavity laser beam shaping approaches since only a grey-scale image is needed to be changed to select a laser mode. We have also demonstrated that the digital laser can produce conventional stable resonator modes as well as ‘custom’ laser resonators that produce more exotic laser modes. The digital laser is at present limited in the power that it can output, but this may be overcome with careful engineering of bespoke liquid crystals for high power applications. Just as SLMs external to the laser cavity have proved an excellent means for testing high-power beam shaping elements before fabrication, and have in the process opened up many avenues for low-average-power applications of structured light such as holographic optical tweezers, the digital laser may well become a robust, easy-to-implement, test bed for intra-cavity beam-shaping ideas. Moreover, as the digital laser is rewritable it allows for dynamic intra-cavity beam shaping, as we have shown [4.22] by ‘playing a video’ inside a laser for the first time. Applications of this would range from controlling thermal lensing and aberrations in real-time to real-time mode control and switching. Customized laser modes are now only a picture away.

4.6. References

[4.1]. A. E. Siegman, “Laser beams and resonators: the 1960s,” IEEE J. Sel. Top. Quantum Electron. **6**, 1380 (2000).

[4.2]. A. E. Siegman, “Laser beams and resonators: Beyond the 1960s,” IEEE J. Sel. Top. Quantum Electron **6**, 1389 (2000).

[4.3]. P. A. Belanger & C. Pare, “Optical resonators using graded-phase mirrors,” Opt. Lett. **16**, 1057 (1991).

[4.4]. C. Pare, L. Gagnon & P. A. Belanger, “Aspherical laser resonators: an analogy with quantum mechanics,” Phys. Rev. A **46**, 4150 (1992).

[4.5]. I. A. Litvin & A. Forbes, “Intra-cavity flat-top beam generation,” Opt. Express **17**, 15891 (2009).

[4.6]. M. Kuznetsov, M. Stern & J. Coppeta, “Single transverse mode optical resonators,” Opt. Express **13**, 171 (2005).

[4.7]. B. Tiffany & J. Leger, “Losses of bound and unbound custom resonator modes,” Opt. Express **15**, 13463 (2007).

[4.8]. P. A. Be´langer, R. L. Lachance & C. Pare, “Super-Gaussian output from a CO2 laser by using a graded-phase mirror resonator,” Opt. Lett. **17**, 739 (1992).

[4.9]. J. R. Leger, D. Chen & Z. Wang, “Diffractive optical element for mode shaping of a Nd:YAG laser,” Opt. Lett. **19**, 108 (1994).

[4.10]. Leger, J. R., Chen, D. & Dai, K. High modal discrimination in a Nd:YAG laser resonator with internal phase gratings. Opt. Lett. **19**, 1976 (1994).

[4.11]. A. J. Caley, M. J. Thomson, J. Liu, A. J. Waddie & M. R. Taghizadeh, “Diffractive optical elements for high gain lasers with arbitrary output beam profiles,” Opt. Express **15**, 10699 (2007).

[4.12]. J. Bourderionnet, A. Brignon, J.-P. Huignard, A. Delboulbe & B. Loiseaux, “Spatial mode control of a diode-pumped Nd:YAG laser by an intracavity liquid crystal light valve,” Opt. Lett. **26**, 1958 (2001).

[4.13]. J. C. Dainty, A. V. Koryabin & A. V. Kudryashov, “Low-order adaptive deformable mirror,” Appl. Opt. **37**, 4663 (1998).

[4.14]. Lubeigt, W., Valentine, G., Girkin, J., Bente, E. & Burns, D. Active transverse mode control and optimization of an all-solid-state laser using an intracavity adaptive-optic mirror. Opt. Express **10**, 550 (2002).

[4.15]. T. Y. Cherezova, L. N. Kaptsov & A. V. Kudryashov, “Cw industrial rod YAG:Nd3+ laser with an intracavity active bimorph mirror,” Appl. Opt. **35**, 2554 (1996).

[4.16]. W. Lubeigt, M. Griffith, L. Laycock & D. Burns, “Reduction of the time-to-fullbrightness in solid-state lasers using intra-cavity adaptive optics,” Opt. Express **17**, 12057 (2009).

[4.17]. W. Lubeigt et al. “Control of solid-state lasers using an intra-cavity MEMS micromirror,” Opt. Express **19**, 2456 (2011).

[4.18]. S. Piehler, B. Weichelt, A. Voss, M. A. Ahmed & T. Graf, “Power scaling of fundamental-mode thin-disk lasers using intracavity deformable mirrors,” Opt. Lett. **37**, 5033 (2011).

[4.19]. A. Dudley, R. Vasilyeu, V. Belyi, N. Khilo, P. Ropot & A. Forbes, “Controlling the evolution of nondiffracting speckle by complex amplitude modulation on a phase-only spatial light modulator,” Opt. Commun. **285**, 5 (2012).

[4.20]. V. Arrizo´n, “Optimum on-axis computer-generated hologram encoded into low resolution phase-modulation devices,” Opt. Lett. **28**, 2521 (2003).

[4.21]. G. Porat, I. Dolev, O. Barlev & A. Arie, “Airy beam laser,” Opt. Lett. **36**, 4119 (2011).

[4.22]. S. Ngcobo, I. A. Litvin, L. Burger, and A. Forbes, “A digital laser for on-demand laser modes,” Nat. Commun. **4**, 2289 (2013).

CHAPTER FIVE

Tuneable Gaussian to flat-top resonator by amplitude beam shaping

5.1. Introduction

Commercially available lasers generally produce a Gaussian beam profile which is a convenient spatial laser beam profile since it has been shown to maintain its spatial distribution when propagating over a long distance and also being very good at focusing to a diffraction limited spot. The major disadvantage of the Gaussian beam is that when focused the spot area is limited by a beam diameter of $1/e^2$ level which contains only 86.5% of the energy of the laser beam and the intensity at the boundary edges is only 13.5% of the peak intensity. Certain applications have attempted to use a Gaussian beam profile such as laser material processing for ablation or drilling holes and it has been shown that the energy on the boundary edges or wings of such a beam is either lost or causes major damage to the surrounding material even the central high-intensity peak would cause damage to the substrate for ablation processes. Laser materials applications such laser ablation have been shown to require specific laser beam threshold power over a certain area and this make the use of Gaussian beam profile to be not favourable. The majority of laser material processing applications have been demonstrated to require uniform beam intensity profile over a certain limited area with sharp edges on the boundary of the beam. The laser beam with uniform intensity distribution over the cross-section of the working plane is called a flat-top beam or sometimes a top-hat beam.

Laser systems that produce flat-top beams are desirables for many applications [5.1] such as laser welding, laser micro-fabrication, laser radar, laser scanning and optical processing applications. There are many extra-cavity techniques that have been demonstrated for the creation of flat-top beams [3.14, 4.5, 5.2, 5.3], and most of them have low loss even though their optical delivery system is associated with some complexity which require careful alignment and fixed input beam parameters to the shaping elements. There are a number of advantages to having a flat-top beam profile as a direct output from a laser resonator such as obtaining optimised energy extraction from the gain medium. However the methods of obtaining the flat-top beam profiles as the laser eigenmodes are mostly complicated and often required expensive custom made diffractive optical elements, aspheric elements, graded phase mirrors and deformable mirrors [3.2, 3.4, 4.5, 4.8–4.11, 4.14, 4.16, 5.4, 5.5].

In addition to that almost all solutions currently have been designed for a single mode and are not tuneable in the mode selection.

In this Chapter [6.10] we offer a different approach to the techniques for obtaining a Flat-Top (FT) beam as the fundamental oscillating mode that is emitted from a laser cavity. The technique that we propose requires only an intra-cavity opaque ring as an amplitude filter in combination with a standard circular aperture in a traditional laser cavity. We demonstrate that by carefully choosing well thought out resonator parameters, such a laser cavity can be made to emit a FT beam or a Gaussian beam by merely adjusting the circular aperture. The cavity becomes mode tuneable in an easy manner to implement, which require no new optic or realignment of the resonator. In addition to that the FT beam is found in the near field and most importantly also in the far field which then significantly simplifies the delivery optics since no relay imaging is required. This approach is different from other previously reported FT resonators where the FT beam is created only in the near field. We verify our concept and theoretical predictions using a "digital laser" [4.23] comprising an intra-cavity spatial light modulator as a rewritable holographic mirror.

5.2. Concept and simulation

Our concept is based on the mode selective properties of a cavity comprising both an aperture and a ring obstruction, as illustrated in Fig. 5.2.1. We show that the desired beams can be obtained by careful selection of the normalized radius $Y_a = \rho_a/w_0$ of the opaque ring of width h, and the normalised radius $Y_c = \rho_c/w_0$ of the circular aperture; here w_0 and w_c are the beam radii of the Gaussian beam in the bare cavity (without the ring of radius ρ_a and aperture of radius ρ_c) at the flat and curved mirror, respectively. Single pass studies [3.7, 3.10] on the transmission of radial Laguerre-Gaussian beams through each component (separately) have indicated that when the aperture is "open" ($Y_c > 2$) all the radial modes have similar losses, while as it is closed so the Gaussian mode dominates with the lowest loss; in the latter scenario there is no radial mode selectivity by this element.

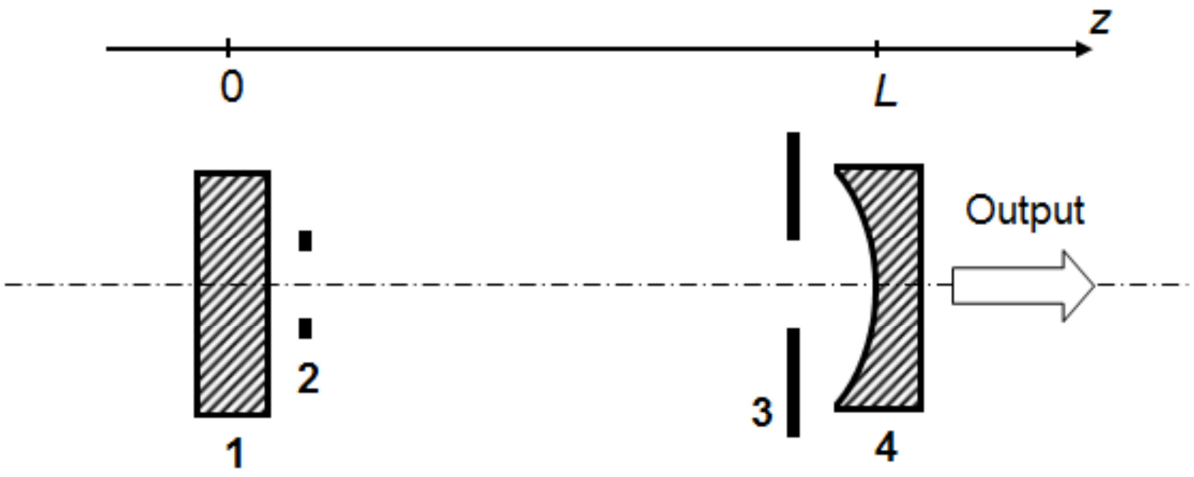

Fig. 5.2.1: A schematic representation of the concept. An absorbing ring (2) is placed at the plano (1) end of a plano-concave cavity. A standard circular aperture (3) is placed at the opposite end, and the mode is transmitted through the output coupler (4).

This is depicted through simulation in Fig. 5.2.2 (a). The opaque ring on the other hand can be highly mode selective, and does not exhibit the monotonic behaviour of the aperture. Rather, there are normalised radii where the losses are inverted for the radial modes (lower radial modes have higher losses), and other radii where the losses for several radial modes would be the same or similar, as seen through simulation in Fig. 5.2.2 (b).

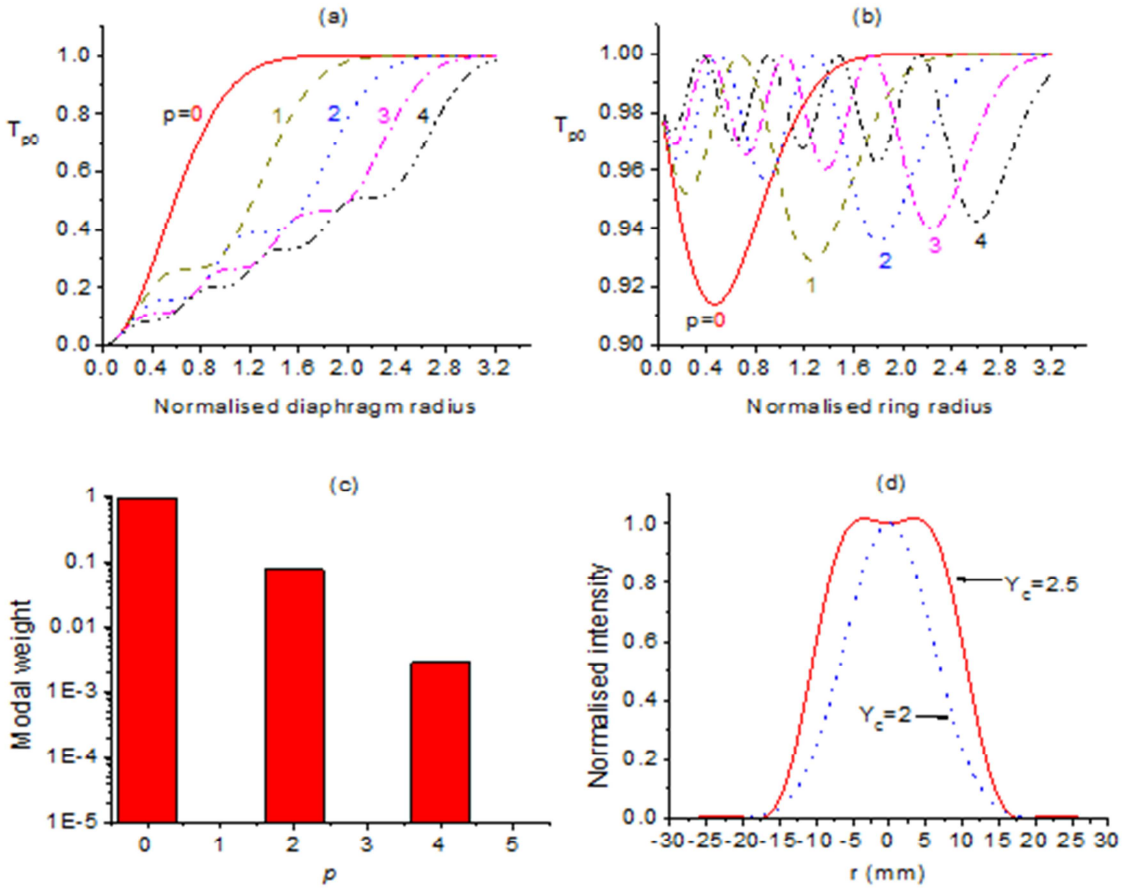

Fig. 5.2.2: (a) Single pass losses for radial Laguerre-Gaussian modes through an aperture, (b) Single pass losses for radial Laguerre-Gaussian modes through an opaque ring, (c) Predicted modal spectrum of radial (p) modes for Y_a = 1.55 and Y_c = 2.5, and (d) Predicted output modes from the cavity in the far field showing a quasi-Gaussian (Y_c = 2) and flat top beam (Y_c = 2.5). The simulations were performed with a normalised ring radius of Y_a = 1.55 and a ring width of h = 20 μm. The parameters of the cavity were selected to match the experiment, namely, R = 500 mm and L = 252 mm for g ~0.5 at a wavelength of λ = 1064 nm.

This suggests a simple approach to tuneability: if the normalized ring radius is chosen to allow particular Laguerre-Gaussian radial modes to lase simultaneously, then they will do so incoherently. If the aperture is open, so that the ring is the mode determining element, then our Fox-Li analysis predicts a flat-top beam as the output. As the aperture is steadily closed, so it becomes the mode determining element and the Gaussian mode is selected, based on substantially lower round trip losses. Hence only the aperture opening needs to change to control the mode.

Our simulation results, shown in Fig. 5.2.2, suggest that for $Y_a \approx 1.5$ the cavity eigenmode is a FT beam, the purity of which can be adjusted by varying Y_c. We find optimal settings of Y_c = 2.5 for a

high quality FT beam, which can be approximated in shape by a super-Gaussian beam of order ~ 5. The incoherent modal spectrum, comprising three radial Laguerre-Gaussian modes, is shown in Fig. 5.2.2 (c). Furthermore we predict that the FT beam can be transformed into a quasi-Gaussian beam by simply adjusting the circular aperture to Y_c = 2.0, while keeping Y_a. Since the FT beam is a incoherent sum of radial modes the shape remains invariant during propagation. The results are shown in the far field in Fig. 5.2.2 (d) for both beams. If the circular aperture is opened further more exotic modes are found, for example, a donut mode at Y_c = 2.6.

5.3. Experimental setup and results

In order to test the simulated results we used the laser set–up shown in Fig. 5.3.1 (a). The cavity was arranged in a Z-shape to allow the high power pump (808 nm) to pass through the gain medium (Nd:YAG) without interference from the aperture and ring mask. The stable plano-concave cavity had an effective length of 252 mm, with the circular aperture placed directly in front of the curved (R = 500 mm) output coupler of reflectivity 80%. The output mode could be measured in both the near field and far field with imaging or Fourier transforming optics. Care was taken to separate the lasing wavelength (1064 nm) from the pump light (808 nm) with suitable filters.

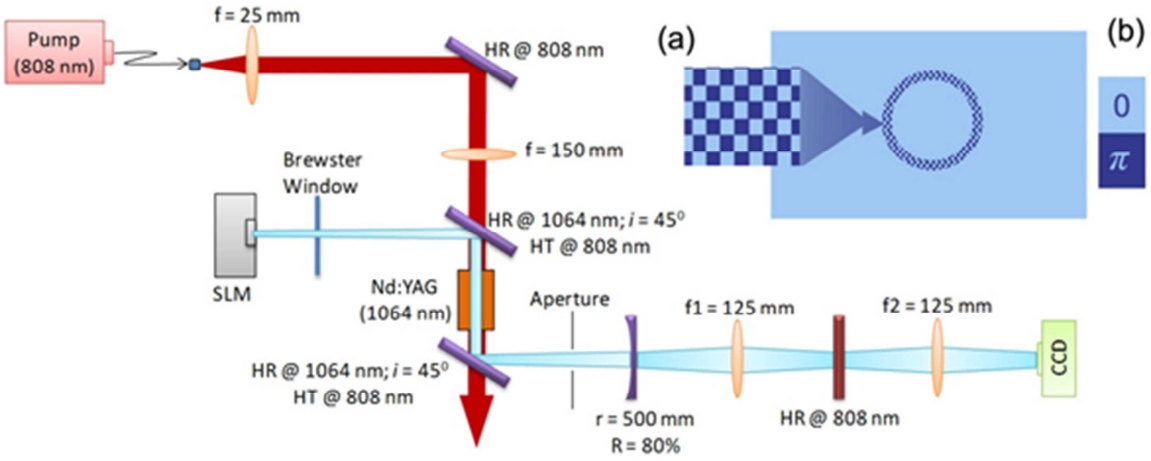

Fig. 5.3.1: (a) Schematic setup of an intra-cavity SLM with diagnostic and control equipment. The High Reflectors (HR) were used to reflect the 808 nm or 1064 nm wavelengths. (b) SLM phase screen acted as a flat-end mirror containing an opaque ring of 100 μm width.

An additional novel aspect of this experiment was the use of a “digital laser” [4.23]. One of the cavity mirrors in the digital laser setup is a rewritable phase-only spatial light modulator (SLM), forming a

holographic end-mirror. The SLM was programmed with a digital hologram representing both the flat mirror and the opaque ring, as shown in Fig. 5.3.1 (b). The digital laser allowed for easy optimisation of the ring radius as well as the ring thickness. To vary these parameters with lithographically produced rings of varying thickness and radii would be time consuming, and would require a realignment of the cavity for each setting. In the digital laser, a new ring could be created by merely changing an image on the control PC representing the desired digital hologram, without any realignment. The amplitude modulation employed to realise the ring was achieved by complex amplitude modulation [3.13, 4.21] using high spatial frequency gratings in the form of so-called "checker boxes".

On the other side of the cavity we had a variable circular aperture which was controlled manually in order to find the optimal value of Y_c. This standard aperture provided the tuneability of the mode. The output from the digital laser is shown in Fig. 5.3.2, where the near field and the far field intensity profiles of the quasi-Gaussian (a) and Flat-top (b) beams are shown. In the first four panels (a-b) we have the results for a 20 μm width ring, while in the last four panels (c-d) we have the results for a 100 μm width ring. We note that the spatial intensity distributions are in good agreement with the simulated Fox-Li results in Fig. 5.2.2 (d). Moreover, as predicted by theory, the desired shapes are found in the far field too. The field patterns are also found at values of Y_a and Y_c close to those predicted by theory, differing by less than 10%. The small deviation can be attributed to minor mode size errors, e.g., due to small thermal lensing or refractive index errors.

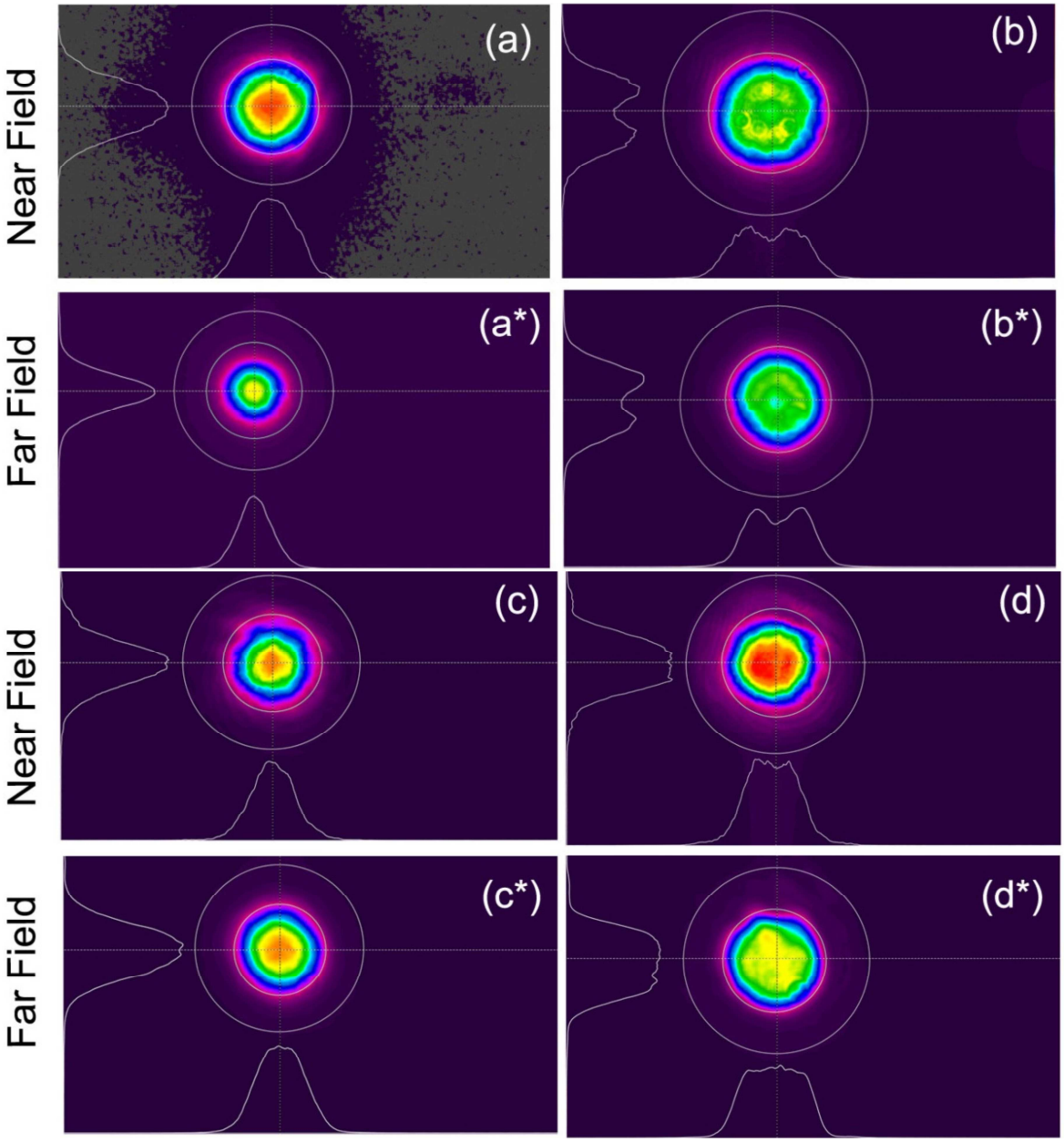

Fig. 5.3.2: Experimentally obtained near field and far field images of the Gaussian beam and Flattop beam for ring width settings of (a-b): 20 μm and (c-d): 100 μm. Gaussian beam (a and a*) and Flat-top beam (b and b*) for Y_a = 1.4, a ring width of 20 μm, and Y_c = 2.0 (Gaussian) and 2.3 (FT). Gaussian beam (c and c*) and Flat-top beam (d and d*) for Y_a = 1.4, a ring width of 100 μm, and Y_c = 2.0 (Gaussian), 2.3 (FT). These values are in good agreement with theory.

Slope efficiency measurements, Fig. 5.3.3, reveal that the FT beam has the highest slop efficiency but also the highest threshold as compared to the quasi-Gaussian beam selected by the ring cavity. The FT beam slope efficiency is approximately 2 times that of the quasi-Gaussian. This can be explained by the fact that the FT beam has a much larger gain volume than the quasi-Gaussian mode and is better matched to the pump beam in size and shape. For comparison the data for a Gaussian beam without

any ring is also shown; this was achieved with no opaque ring programmed on the SLM and a normalized circular aperture set to Y_a = 2.0 on the curve mirror (i.e., the standard approach to Gaussian mode selection). The quasi- Gaussian and Gaussian mode show little difference when the ring width is small (20 μm), indicating that indeed the perturbation from the ring is minimal in the case of selecting the quasi-Gaussian, and thus it may indeed be considered as a Gaussian mode, in agreement with the theoretical prediction. It has been suggested previously [3.7] that in some cases amplitude masks do not lead to higher losses, and this could be the situation here too. When the ring width increases the quasi-Gaussian departs further from the ideal Gaussian mode and the lasing threshold increases.

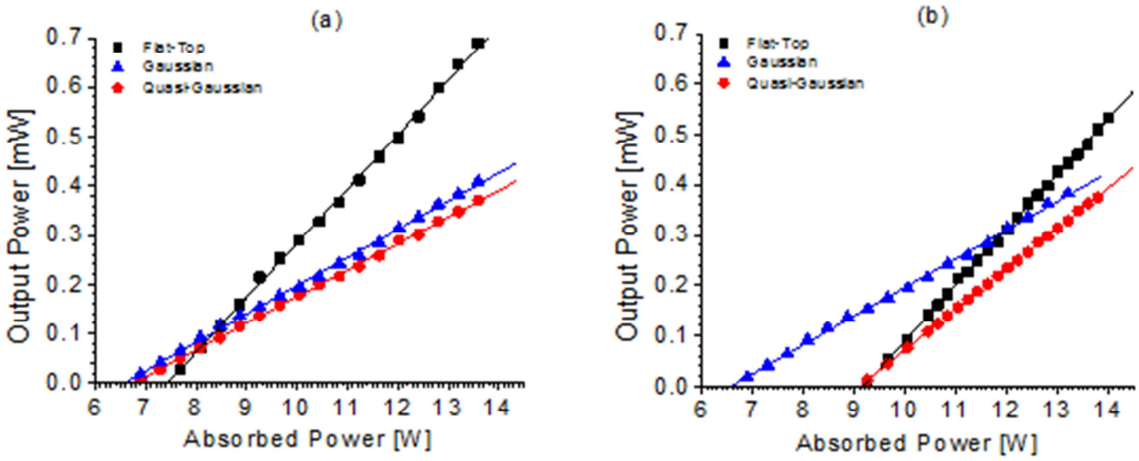

Fig. 5.3.3: The slope efficiencies of the FT beam, quasi Gaussian beam and Gaussian beam for (a) 20 μm and (b) 100 μm ring width.

Finally we point out that while we have used the digital laser to prove the principle, one would not use the intra-cavity SLM approach in a high power system. Rather, one would make use of custom optical elements to implement the ring aperture, thereby increasing the damage threshold and lowering the losses, to produce a more efficient and practical system.

5.4. Conclusion

The conclusion is that we have created and demonstrated for the first time a new laser cavity that is mode tuneable. We have established that by simply adjusting the diameter of a standard circular aperture inside the cavity, the mode that is emitted by the laser can be selected from the ubiquitous

Gaussian to a Flat-top beam. The opaque ring mask was implemented on an SLM as an intra-cavity holographic end-mirror for the advantage that this allows in testing the design parameters. For the construction of a similar high-power resonator which will be optimised for maximum power extraction by using standard optics and lithographic processed optical elements, will eliminate the use of an SLM and its associated losses.

5.5. References

[5.1]. F. M. Dickey, S. C. Holswade, and D. L. Shealy, "Laser Beam Shaping Applications," (Taylor and Francis, 2006).

[5.2]. J. A. Hoffnagle and C. M. Jefferson, "Design and performance of a refractive optical system that converts a Gaussian to a flattop beam," Appl. Opt. **39**(30), 5488 (2000).

[5.3]. A. Laskin and V. Laskin, "Imaging techniques with refractive beam shaping optics," Proc. SPIE **8490**, 84900J-11 (2012).

[5.4]. T. Y. Cherezova, S. S. Chesnokov, L. N. Kaptsov, V. V. Samarkin, and A. V. Kudryashov, "Active laser resonator performance: formation of a specified intensity output," Appl. Opt. **40**(33), 6026 (2001).

[5.5]. M. Gerber and T. Graf, "Generation of super-Gaussian modes in Nd:YAG lasers with a graded-phase mirror," IEEE J. Quantum Electron. **40**(6), 741 (2004).

CHAPTER SIX

Doughnut laser beam as an incoherent superposition of two petal beams

6.1. Introduction

Laguerre-Gaussian beams are a well-known solution to the Helmholtz equation in the paraxial approximation under conditions of cylindrical symmetry, and they have become a standard topic in many laser textbooks. In the scientific community Laguerre-Gaussian modes that have azimuthal order, l , have of lately attracted renewed attention because they carry orbital angular momentum of $l\hbar$ per photon [1.29, 6.1, 6.2]. There are many techniques that have been demonstrated for extra-cavity generation of such beams such as using spatial light modulators [6.3], spiral phase elements [6.4], cylindrical lens mode converters [6.5], etc. There has been a significant effort in the scientific community in creating such beams inside the laser resonator with appropriate intra-cavity optical elements. The techniques that have been used to achieve such modes include the thermally induced focusing [6.6, 6.7], spatially variable retardation plates [6.8], and ring-shaped pumps [6.9, 1.20]. In all the above mentioned scenarios, an intensity pattern with a doughnut shape was observed being emitted from the laser cavity. Paradoxically this may not be indicative of the presence of a pure azimuthal Laguerre-Gaussian mode.

In this Chapter [6.14] we revisit the generation and detection of pure azimuthal Laguerre-Gaussian modes. We demonstrate a laser resonator that generates a doughnut-shaped mode profile and show through a number of experiments that it is not a pure Laguerre-Gaussian mode but rather an incoherent sum of petal-like modes. We illustrate that the conventional tools for mode analysis, such as beam propagation and M^2 measurements, intensity, and second moment measurements, would not have been conclusive in determining the correct mode structure. Our results bring into question previous claims of Laguerre-Gaussian mode generation and outline the required analysis to overcome this ambiguity in future studies. Such structure of the doughnut mode may be in contradiction to the current experimental procedures of implementation, especially in areas such as optical tweezing of nanoparticles and atoms and angular momentum based experiments where it is necessary to know the real field structure and not only the intensity of the field.

6.2. Experimental setup and laser performance

The selection of a doughnut-shaped mode is implemented through the use of an end-pumped solid-state laser resonator with a plano-concave configuration which is shown in Fig. 6.2.1. An additional novelty is the use of a spatial light modulator (SLM) as a concave high reflector end-mirror of the resonator, thus forming the so-called “digital laser” [4.22] as show in Chapter 4.

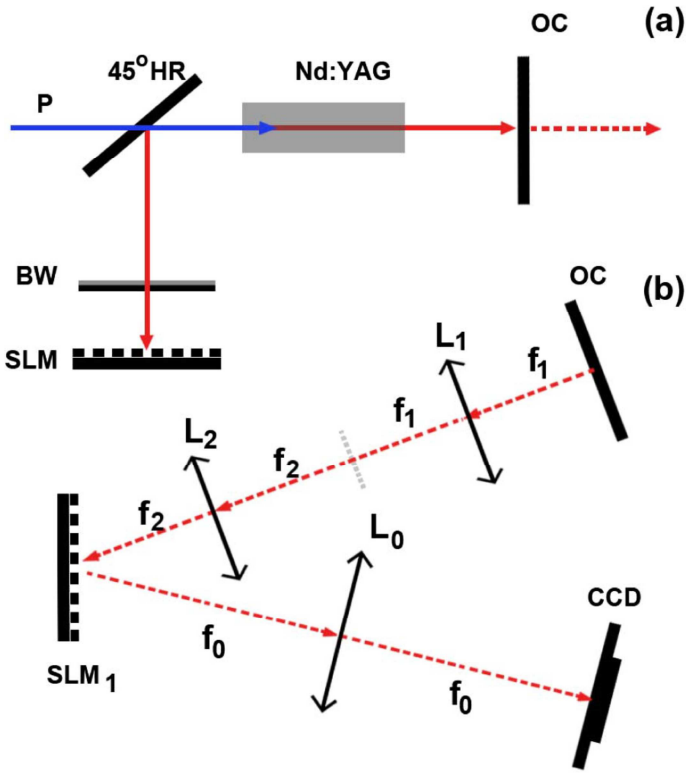

Fig. 6.2.1: (a) Schematic of the digital laser concept for the generation of a doughnut mode showing the spatial light modulator (SLM), Brewster window (BW), high reflectivity (HR) mirror at an angle of 45°, Nd:YAG gain medium pumped by an external laser diode (P) source, and the output coupler (OC). (b) Schematic of the experimental setup of the modal decomposition technique.

The gain medium of the laser was a 1% Nd:YAG crystal rod of 30 mm length and a diameter of 4 mm. The resonator configuration allowed for the crystal to be end pumped with a 75 W Jenoptik (JOLD 75 CPXF 2PW) multimode fibre-coupled laser diode operated at 808 nm. The laser mode size was selected for maximizing mode purity by avoiding aperture effects and not for maximising output power. Therefore the digital laser was operated close to a threshold and consequently the laser operation was achieved at an absorbed pump power of approximately 14 W with a slope efficiency of only 0.5% as shown in Fig. 6.2.2.

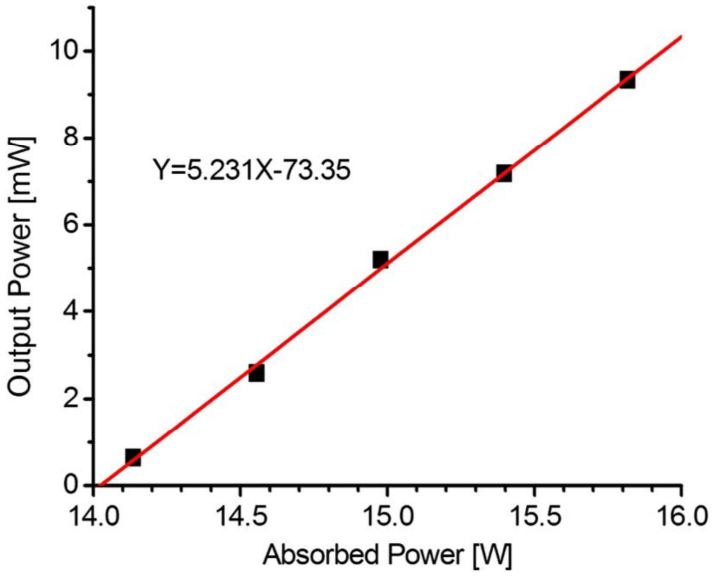

Fig. 6.2.2: Slope efficiency graph for generation of the doughnut mode by the digital laser setup.

We noted that the output power could be improved to much higher values by excluding the SLM and redesigning the cavity for maximizing output power. But this was not the aim of the present study. The experimental results were taken just above this threshold value where there were minimal thermal effects. Any disturbance to the stability of the laser system caused by induced thermal lensing was compensated by the curvature on the intra-cavity SLM holographic end-mirror and cavity length adjustment. The plane mirror was used as an output coupler with a reflectivity of 60% and the cavity length was approximately 373 mm. The radius of curvature of the concave holographic end-mirror was digitally programmed to be R = 500 mm, which gives rise to a resonator stability, g, parameter of 0.25, which is within the stability boundary of $0 < g < 1$. The mode profile of the generated doughnut mode is shown in Fig. 6.2.3. It was intra-cavity selected by spot defecting the concave mirror, with an opaque disk of radius a = 0.5 mm, where the curvature (phase) and opaque disk (amplitude) were encoded using complex amplitude modulation on the SLM [4.20].

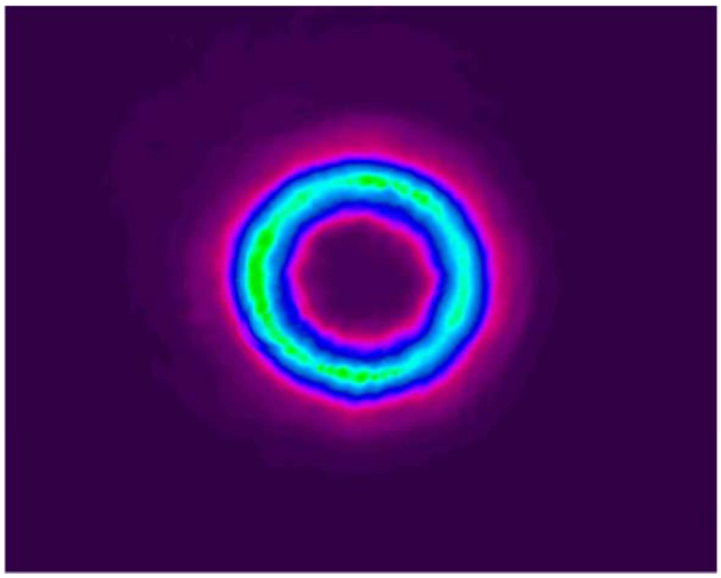

Fig. 6.2.3: Doughnut beam obtained by programming an intra-cavity circular aperture on a digital holographic end-mirror of a digital laser.

The optimum functionality of the digital laser required fulfilment of several key properties of the SLM to be met, such as high resolution, high efficiency at the desired polarization, minimal phase-amplitude cross-talk, reasonable damage threshold, and a large phase shift at the laser wavelength. The suitable SLM that fulfilled these parameters was a Hamamatsu, LCOSSLM X110468E that had an 800 × 600 pixel arrays with a 20 μm pitch, a manufacture quoted efficiency of 95%, with a damage threshold of 25 W/cm^2 and a phase shift of more than 2π. More details of the operation of the digital laser can be found in [4.22, 6.10] or in Chapter 4 of this document.

6.3. Analysis of the results

We performed a Fox-Li analysis of the cavity using the parameters previously specified to identify the modal structure of the modes with the lowest round-trip losses. The intensity of the resulting modes with the highest eigenvalue, which corresponds to the lowest losses, is illustrated in Fig. 6.3.1.

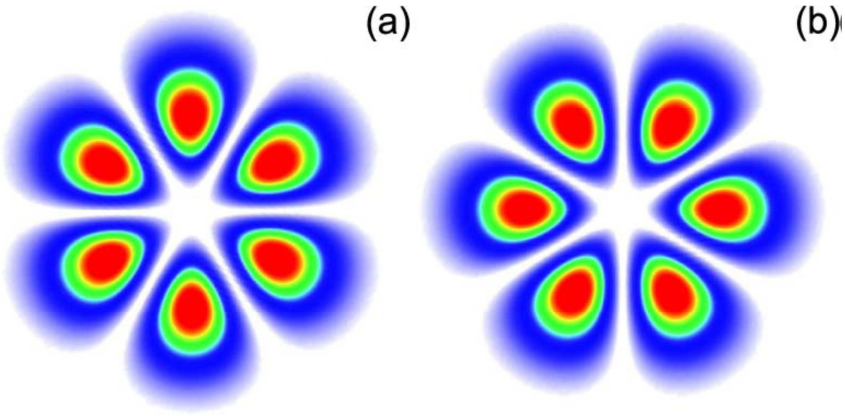

Fig. 6.3.1: Intensities of the modes with the highest eigenvalue, equivalent to 0.987, which were obtained through the Fox–Li method.

We know from [3.9] that the obtained petal modes which are shown in Fig. 6.3.1 are a superposition of two Laguerre-Gaussian modes of zero radial order (p = 0) and azimuthal order l and with different intermodal phase shift, namely,

$$u_{even}^{l}(r;\ \phi;\ z) = \mathrm{LG}_l(r;\ \phi;\ z)\left[e^{(-il\phi)} + e^{(il\phi)}\right], \tag{6.3.1}$$

$$u_{odd}^{l}(r;\ \phi;\ z) = i\ \mathrm{LG}_l(r;\ \phi;\ z)\left[e^{(-il\phi)} - e^{(il\phi)}\right], \tag{6.3.2}$$

where

$$LG_l(r,z,\phi) = \sqrt{\frac{2}{\pi\, w(z)^2 |l|!}}\left(\frac{\sqrt{2}\,r}{w_0}\right)^{|l|} exp\left(\frac{-r2}{w_0^2} + ik_0\frac{r^2}{2R(z)}\right) exp(i(1+|l|)\Phi(z)), \tag{6.3.3}$$

where $\Phi(z) = \arctan(z/z_r)$, $w(z) = w_0\sqrt{1+(z/z_R)^2}$, $R(z) = z(1+(z_R/z)^2$, $z_r = \pi w_0^2/\lambda$, w_0 is the beam width, and λ the wavelength.

Based on the Fox-Li simulation and the experimental results that were obtained, we can assume that the obtained doughnut beam profile that is shown in Fig. 6.2.3 is the superposition of two petal beams that are shown in Fig. 6.3.1. Theoretically using Eq. (6.3.4) and (6.3.5), such a doughnut superposition mode can be generated by a coherent or incoherent sum of the petal beams as shown in Fig. 6.3.2:

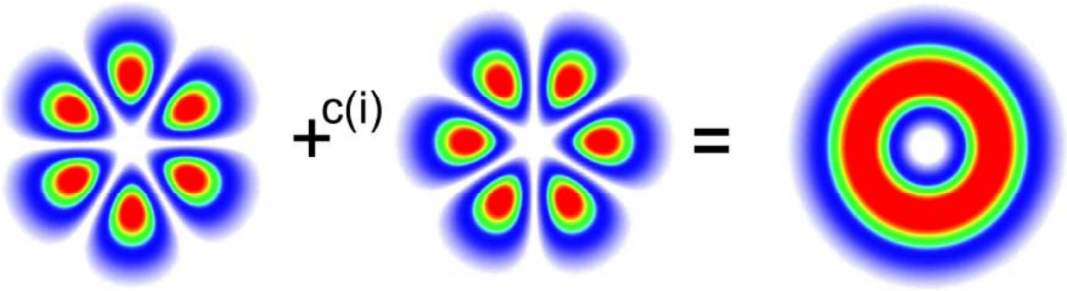

Fig. 6.3.2: Doughnut beam produced by a coherent and an incoherent superposition of the two petal beams.

$$D_i^l(r;\, z) = |u_{odd}^l(r;\, \phi;\, z)|^2 + |u_{even}^l(r;\, \phi;\, z)|^2, \tag{6.3.4}$$

$$D_c^l(r;\, z) = i\, u_{odd}^l(r;\, \phi;\, z) + u_{even}^l(r;\, \phi;\, z), \tag{6.3.5}$$

where (D_c) is the coherent superposition and (D_c) is the incoherent superposition.

Both the coherent and incoherent superposition will have the same final intensity distribution. However, we see that the final solution for the electromagnetic field of the coherent superposition as shown in Eq. (6.3.5) is $D_c^l(r;\, z) = LG_l(r;\, z;\, \phi)\, \exp(il\phi)$, is in fact the field of a Laguerre-Gaussian mode [6.16]. This result is markedly different from an incoherent superposition where the two petal modes are treated independently, as all components are a superposition of two Laguerre-Gaussian modes of opposite azimuthal order as shown Eq. (6.3.4). Based on this difference we are able to detect the correct solution for the superposition by applying an azimuthal modal decomposition technique which is shown in Fig. 6.2.1 (b). The modal decomposition was achieved by executing an optical inner product of the output beam with an azimuthal match filter [2.12]. The output beam from the laser was relay imaged using a $4f$ imaging system and directed onto SLM_1 as shown in Fig. 6.2.1 (b) to which the azimuthal match filter was addressed. The phase structure of the filter was set to $exp(il\phi)$ for various l values. To identify the full set of azimuthal modes contained in the doughnut beam that is emitted from the digital laser resonator, an optical Fourier transform was performed of the resultant beam with the aid of a thin lens (L0) and the relative modal weightings were determined from the on-axis intensity [2.12, 6.12].

The results in Fig. 6.3.3 demonstrate the experimentally obtained modal decomposition of the doughnut mode. We observed two peaks for the corresponding azimuthal mode numbers -3 and 3. This result is in contradiction to a coherent superposition as described in Eq. (6.3.5) as only a single peak is expected. We do, however, see that the modal decomposition is in perfect agreement with an

incoherent superposition as described by Eq. (6.3.4) because the petal modes are treated independently and, thus, each mode would present two peaks [3.9, 6.13].

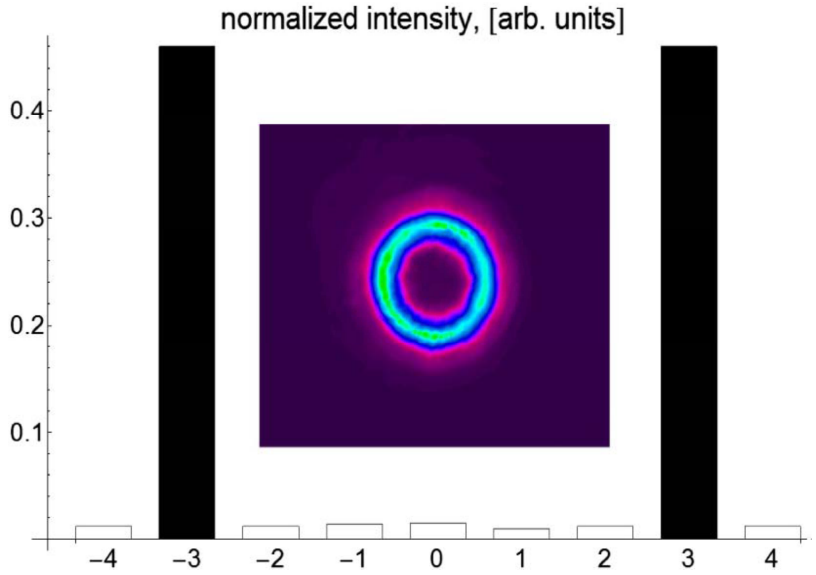

Fig. 6.3.3: Azimuthal modal decomposition of the doughnut mode.

To verify that the doughnut mode derives from an incoherent superposition we have performed the following interference experiment as shown in Fig. 6.3.4. We directed and aligned the doughnut beam to pass through a plate that consists of two pinholes. The position of the two pinholes corresponds to the position of the two petal lobes that comprise the superposition as shown in Fig. 6.3.4 (c). The specific positions that we selected and their corresponding numbers are illustrated in Fig. 6.3.4 (b). We thereafter directed the segments of the doughnut beam that passes through the pinholes to interfere at some position along the propagation axis as shown in Fig. 6.3.4 (a), (d), and (e).

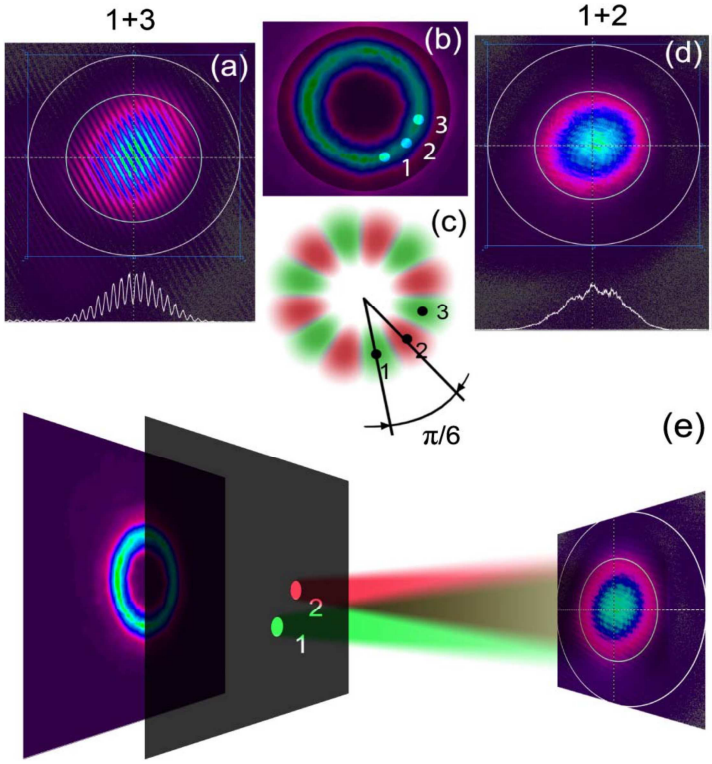

Fig. 6.3.4: Interference of the field produced by selecting two portions of the doughnut beam through two pinholes (b). The pinholes correspond to the lobes of the superimposed field (c), where we interfere either two lobes of the same petal beam [1 and 3, (a)] or two lobes with one from each petal beam [1 and 2, (d)]. (e) Schematic of the interference experiment.

The two petal fields that comprise the superposition for the doughnut beam are illustrated in Fig. 6.3.4 (c) and they are represented as green and red. We expect that if we interfere lobes 1 and 2, we should observe no interference fringes. However, if lobes 1 and 3 are interfered, then strong fringes will be present. This hypothesis was proven to be accurate as is evident from the experimental results shown in Fig. 6.3.4 (a) and (d) where notably stable interference lines are present.

6.4. Discussion

The rigorous tests provided by the azimuthal modal decomposition and interference experiment are evidence enough to conclude that the doughnut mode is an incoherent superposition of two petal modes. To understand the process occurring in the cavity during the modal build-up we have to take into account the area of the laser crystal that is pumped. Because of typical perturbations, it is not trivial to reach ideal symmetry from a custom laser cavity and there exists a degree of asymmetry.

The asymmetry can be introduced through the geometry of the custom cavity or spatial distribution of the gain and presents a minimal difference in the eigenvalues of the two lowest loss modes, which were theoretically previously identical as petal modes as shown in Fig. 6.3.1. The lowest loss mode of the two will preferentially oscillate; however, the residual gain in the pumped medium will assist in the oscillation of the mode with the higher round-trip losses. In the case of substantial asymmetry, the oscillation of the mode with higher losses becomes impossible and the output of the laser is a petal beam, which has previously been investigated in detail [1.15, 3.9]. One may also understand this from a degeneracy perspective: since there is no physical process to distinguish the handedness of the pure azimuthal modes (positive or negative l values), and since they have the same phase velocity and frequency, superposition modes are easily formed such as the well-known petal modes.

6.5. Conclusion

In conclusion, we have implemented the use of a novel digital laser capable of on-demand laser modes to output a doughnut mode. We have demonstrated that, by using well-known traditional techniques for characterizing the mode, we arrive at ambiguous conclusions. Contrary to previously reported studies, we have performed a modal decomposition on our doughnut field that reveals it is not a pure Laguerre-Gaussian mode, but rather an incoherent mix of petal modes. Our theoretical analysis also showed that doughnut-shaped modes may be produced by either coherent or incoherent mixing of odd and even petal-like modes, and that due care must be exercised to distinguish between the two cases. Our results bring into question previous reports on the generation of pure azimuthal Laguerre-Gaussian beams from such cavities, and outline a procedure for unambiguous predictions of such modes.

6.6. References

[6.1]. A. Mair, A. Vaziri, G. Weihs, and A. Zeilinger, “Entanglement of the orbital angular momentum states of photons,” Nature **412**, 313 (2001).

[6.2]. E. Yao, S. Franke-Arnold, J. Courtial, M. Padgett, and S. Barnett, “Observation of quantum entanglement using spatial light modulators,” Opt. Express **14**, 13089 (2006).

[6.3]. A. Shevchenko, S. Buchter, N. Tabiryan, and M. Kaivola, “Creation of a hollow laser beam using self-phase modulation in a nematic liquid crystal,” Opt. Commun. **77**, 232 (2004).

[6.4]. C. Paterson and R. Smith, “Higher-order Bessel waves produced by axicon-type computer-generated holograms,” Opt. Commun. **124**, 121 (1996).

[6.5]. M. W. Beijersbergen, L. Allen, H. E. L. O. van der Veen, and J. P. Woerdman, “Astigmatic laser mode converters and transfer of orbital angular momentum,” Opt. Commun. **96**, 123 (1993).

[6.6]. G. Machavariani, Y. Lumer, I. Moshe, A. Meir, S. Jackel, and N. Davidson, “Birefringence-induced bifocusing for selection of radially or azimuthally polarized laser modes,” Appl. Opt. 46, 3304 (2007).

[6.7]. M. Okida, Y. Hayashi, T. Omatsu, J. Hamazaki, and R. Morita, “High-power non-astigmatic TEM00 and vortex mode generation in a compact bounce laser design,” Appl. Phys. B **97**, 275 (2009).

[6.8]. G. Machavariani, Y. Lumer, I. Moshe, A. Meir, and S. Jackel, “Spatially-variable retardation plate for efficient generation of radially and azimuthally-polarized beam,” Opt. Commun. **281**, 732 (2008).

[6.9]. J. Kim and W. Clarkson, “Selective generation of Laguerre–Gaussian (LG0n) mode output in a diode-laser pumped Nd:YAG laser,” Opt. Commun. **296**, 109 (2013).

[6.10]. S. Ngcobo, K. Ait-Ameur, I. A. Litvin, A. Hasnaoui, and A. Forbes, “Tuneable Gaussian to flat-top resonator by amplitude beam shaping,” Opt. Express **21**, 21113 (2013).

[6.11]. M. Harris, C. A. Hill, P. R. Tapster, and J. M. Vaughan, “Laser modes with helical wave fronts,” Phys. Rev. A **49**, 3119 (1994).

[6.12]. C. Schulze, S. Ngcobo, M. Duparre, and A. Forbes, “Modal decomposition without a priori scale information.,” Opt. Express **20**, 27866 (2012).

[6.13]. I. A. Litvin, L. Burger, and A. Forbes, “Angular self-reconstruction of petal-like beams,” Opt. Lett. **38**, 3363 (2013).

[6.14]. I.A. Litvin, S. Ngcobo, D. Naidoo, K. Ait-Ameur, and A. Forbes, “Doughnut laser beam as an incoherent superposition of two petal beams,” Applied Lett. **39** (3), 704 (2014).

CHAPTER SEVEN

Conclusions and future study

7.1. Conclusions

A literature review of the different methods of generating many types of modes from the laser resonator was discussed in Chapter 1. The lowest-order Gaussian mode solution was derived from the Helmholtz paraxial wave equation and also many other families of high-order Gaussian mode solutions such as Hermite-Gaussian modes and Laguerre-Gaussian modes were discussed.

In Chapter 2 we demonstrated a novel approach of decomposing customised high-order modes that required no *a priori* knowledge of the spatial scale of the modes which lead to an optimised modal expansion. We proposed a simple two-step automated digital approach of first determining the second moment size of the beam w and the beam propagation ratio M^2; and we showed that this led to the scale w_0 ($w_0 = w/\sqrt{M^2}$) of the adapted set to be determined. We showed that this enabled the second step of determining an optimal decomposition in the adapted mode set to be possible whereby we determined the number of modes contained in the arbitrary optical field. The new proposed modal decomposition technique that we have demonstrated will be very useful in applications such as optical communication where it can be used as a decoding device and also in beam shaping techniques or application as a test for purity of the generated modes.

The novel generation of radial high-order Laguerre-Gaussian modes using an intra-cavity amplitude mask containing absorbing rings that match the zeros of the Laguerre polynomial was discussed in Chapter 3. In this Chapter we demonstrated that selective generation of higher-order modes using a fixed optical mask that was specially manufactured to match the mode that was being generated is possible. The intra-cavity generated higher-order Laguerre-Gaussian modes were shown to be of high mode purity and that the highest-order modes experience very low intra-cavity perturbation. The significance of this Chapter is that it demonstrated that high-radial-order Laguerre-Gaussian modes of $p = 5$ extracted more power from the resonator compared to the lowest-order $p = 0$ fundamental mode. These results were shown to provide a new route to high brightness lasers, where a single high-

order mode could be intra-cavity generated to extract all the power from the resonator; and then extra-cavity be shaped to the lowest-order fundamental TEM_{00} mode to increase the brightness of the laser.

The generation of high-order Gaussian modes using an intra-cavity phase-only Spatial Light Modulator (SLM) was discussed in Chapter 4. In this Chapter we demonstrated that any arbitrary mode could be generated on-demand when using a rewritable optical device such as the SLM. We showed that the SLM could be used as an intra-cavity rewriteable end-mirror that could be used to load digital holograms that would match the mode that was being generated. We showed that the generated modes corresponded to the expected modes and that the experimental results were in very good agreement with the theoretically expected one. The significance of this Chapter was to demonstrate a novel digital laser that allowed on demand arbitrary intra-cavity laser mode generation.

In Chapter 5 we demonstrated a novel laser resonator that was tuneable to produce either a Gaussian mode or a Flat-top beam from the laser resonator. In the resonator an intra-cavity opaque ring close to the end-mirror of the cavity was included in the form of a digital hologram which was programmed on a phase-only Spatial Light Modulator. The other side of the laser resonator was also shown to contain an adjustable circular aperture closer to the output coupler. We demonstrated that varying the diameter of the aperture the laser resonator could either generate a Gaussian mode or Flat-top mode. The results of the Chapter showed the practicality and the convenience of using a digital laser to program and test different design parameters instead of the old, expensive and time consuming laborious lithographic technique of manufacturing the opaque rings as an optical element of the laser resonator.

In Chapter 6 we demonstrated a method of detecting Laguerre-Gaussian beams with nonzero azimuthal order since they are routinely created external to laser cavities. We showed that at face value such similar modes that are generated inside a standing wave laser cavity may not be pure Laguerre-Gaussian modes with nonzero azimuthal order, but can be an incoherent sum of petal modes, which do not carry any orbital angular momentum. We used a doughnut mode that was generated using a digital laser to make a number of tests such as modal decomposition using digital holograms to prove that such an intra-cavity generated mode using a standing wave resonator will contain an incoherent sum of petals.

7.2. Future study

The selective excitation of a very pure single high-order radial Laguerre-Gaussian modes from a diode-end-pumped solid-state laser resonator that was discussed in Chapter 2 showed that it is possible to extract maximum power from an intra-cavity oscillating high-order mode of very high purity such that it exceed that of the lowest-order fundamental TEM_{00} mode at critical values that are determined by the relative round-trip losses of the high-order mode. This demonstration is very important for future work of increasing the brightness of the laser beams since it firstly proves that high power extraction from high-order modes is possible and secondly very pure high-order modes with very little perturbation could be generated within the laser mode. These results provide a possible route to future work of increasing the brightness of the laser beam. The future work would include extra-cavity improving the brightness of the beam by reducing the propagation constant M^2 of the high-order Laguerre-Gaussian mode to that of the lowest-order TEM_{00} Gaussian mode. The reduction of M^2 could be achieved by many techniques such as field mapping, interferometric beam combing, geometrical transformations, complex amplitude modulation, refractive or diffractive beam shaping and so on.

The novel digital laser for on-demand laser modes that was discussed in Chapter 4 has opened up a paradigm shift in the scientific community on how laser modes can be generated inside the laser resonator. The simplicity and the robustness at which customised laser modes can be generated by just creating a gray-scale image that represents your desired mode will hopefully make this a future technique of choice for intra-cavity beam-shaping ideas and tests. An added advantage to this technique is that the digital laser allows for dynamic rewritable gray-scale holographic images to be loaded on the SLM for real-time dynamic generation of customised modes to be produced by the laser. These advantages will prove to be significant for many applications that we would be investigating on the usability of the digital laser, from controlling thermal lensing and aberration in real-time, to real-time mode controlling and switching for application such as ranging, thin film deposition processes and optical communications.

The novel modal decomposition technique that was demonstrated in Chapter 2 in combination with the digital laser of Chapter 3 would be a very good complimentary tool in optical communication; where the digital laser will be used as generating device of on-demand modes which will be injected on communication fibre cables while the modal decomposition device could be used as decoding device to determine the modes exiting the fibre cable. This type of application where the two techniques will be utilised will still be an ongoing research that we will be partaking in future.